

THE STAR FORMATION AND MERGER EVOLUTION OF INTERACTING GALAXIES

by

Carrie R. Bridge

A thesis submitted in conformity with the requirements
for the degree of Doctor of Philosophy

Graduate Department of Astronomy and Astrophysics
University of Toronto

© Copyright by Carrie R. Bridge 2007

Abstract

The Star Formation and Merger Evolution of Interacting Galaxies

Carrie R. Bridge

Doctor of Philosophy

Graduate Department of Astronomy and Astrophysics

University of Toronto

2007

Hierarchical models and observations show that galaxy mergers and interactions play a key role in galaxy assembly and star formation, but to what extent is still unclear. This thesis attempts to quantify their contribution to galaxy evolution by probing the number of interactions and mergers, along with their star forming properties as a function of redshift.

The presence of long tidal tails and bridges are robust signatures of recent merger activity. This completely dynamical phenomenon was used to develop a new classification scheme to identify interacting galaxies and probe the interaction fraction and merger rate. We applied this new technique to large area, multi-band imaging obtained via the Canada France Hawaii Telescope Legacy Survey (CFHTLS-Deep), yielding the first statistically secure, lower limit of the galaxy interaction fraction between $0.1 \leq z \leq 1.0$. Optically, the fraction of galaxies undergoing an interaction evolves moderately with redshift as $(1 + z)^{2.24 \pm 0.24}$.

The *Spitzer* $24\mu\text{m}$ coverage of both the Extragalactic First Look Survey (XFLS) and CFHTLS-Deep Survey were used to carry out one of the first and largest merger studies of IR bright galaxies. Within the ACS component of the XFLS, interactions were identified over the full merger sequence using traditional techniques, finding a merger rate increase for $24\mu\text{m}$ galaxies of $(1 + z)^{\sim 2}$. This result implies that merging is an increasingly important process in the evolution of luminous IR galaxies (LIRGs), contributing 40 – 60% of the IR luminosity density and at least 30 – 40% of the star formation rate density at $z \sim 1$.

Galaxy interactions at all stages are found to have elevated star formation rates greater than a factor of two-four (on average) and a higher incidence of AGN activity compared to non-interacting field galaxies. This result supports a causal connection between galaxy merging, induced star formation, and AGN activity. Ultimately, major mergers provide a moderate

contribution to the evolution of the cosmic star formation rate density and IR luminosity density to $z \sim 1$, with an increasing trend suggesting that merging plays a larger role at higher redshifts ($z > 1$). It is also clear that merging plays a significant role in triggering the processes that power the IR emission of LIRG galaxies at $z > 0.5$.

Acknowledgements

Many thanks are due to the following people:

First I offer my sincerest gratitude to my advisor Ray Carlberg, for his encouragement, enthusiasm, guidance and support over the years.

Bob Abraham, Howard Yee, Pat McCarthy, Chris Conselice, Phil Appleton, Lee Armus, and Mark Sullivan with whom I have had many insightful and inspiring conversations.

Mike Hudson, my external examiner, for his careful reading of this dissertation and insightful comments.

Special thanks to Dave Patton, and Tracy Webb for their advice and friendship over the years, and Marc Goodman for his tireless efforts to make my life easier.

Marija, Lawrence, and Preethi, for being great office mates.

Colin Borys, for his loving companionship, shared passion for science, and his ability to focus on what's truly important in life.

Most importantly, I would like thank my family for their unwavering support, and confidence in my abilities. George and Sue Bridge for encouraging my scientific interests, instilling in me perseverance and the drive to follow my heart in life. I could not have asked for more caring and nurturing parents or a more loving brother and sister. You have helped make my dreams a reality.

My grandfather, Milton Bridge for sharing his wisdom, passion for life, and many starry nights at the cottage.

This dissertation is dedicated, with love, to my family.

This research was funded to a large extent by the Ontario Graduate Scholarship in Science and Technology, the National Research Council of Canada (NSERC), and the University of Toronto.

Contents

1	Introduction	1
1.1	Galaxy Mergers and Interactions	1
1.1.1	Dynamics of an Encounter	2
1.1.2	Formation of Tidal Tails	2
1.1.3	Identifying Mergers	3
1.1.4	Starbursts and AGN in Interacting Galaxies	3
1.1.5	The Cosmic Star Formation History	5
1.2	Dissertation Overview	7
2	Observations and Data Analysis: The Spitzer First Look Survey	10
2.1	Introduction	10
2.2	The First Look Survey Observations	11
2.2.1	Mid-Infrared: IRAC Imaging	11
2.2.2	Mid-Infrared: MIPS Imaging	11
2.2.3	Near-Infrared Imaging	12
2.2.4	Optical Imaging	12
2.2.5	Spectroscopic Observations	15
2.3	The Catalog	17
2.3.1	Band Merging	17
2.3.2	Colour Properties and Distributions	18
3	Results from the Spitzer First Look Survey	21
3.1	Introduction	21
3.2	Sample Identification	21
3.2.1	Close Galaxy Pairs	22
3.2.2	Morphological Mergers	23
3.3	Close Pair Results	24
3.3.1	Close Pair Statistics	24

3.3.2	Field Correction	25
3.3.3	Pair Fractions	26
3.4	Morphological Mergers: Results	27
3.4.1	Visually Classified Mergers	27
3.4.2	CAS Mergers	30
3.4.3	Morphological Properties of Close Pairs	30
3.5	Merger Rates	33
3.5.1	Merger Time-scales	34
3.6	The Evolution of the Galaxy Merger Rate $0.2 < z < 1.3$	35
3.6.1	Fitting the Merger Rate Evolution	35
3.6.2	XFLS Merger Rate	36
3.6.3	Mid-IR Merger Rate: Implications	37
3.7	Total Infrared Luminosities of Mergers	37
3.7.1	Estimating the IR Luminosity of Galaxies from Their Mid-IR Emission .	37
3.7.2	Caveats in Deriving LIR	40
3.7.3	The Total IR Luminosity of MIPS sources in the XFLS	40
3.7.4	IR Luminosity of Close Pairs and Mergers	41
3.7.5	AGN Contamination	41
3.7.6	AGN Identification: IRAC Colours	41
3.7.7	The Contribution of Close Pairs and Mergers to the IR Luminosity Density	44
3.8	Star Formation in Mergers & Interactions	46
3.8.1	IR Star Formation Rate Calculations	46
3.8.2	Close Pair and Merger Contribution to the SFR Density	46
3.8.3	Mergers and the SFR Density: Implications	48
3.9	Summary	49
4	Observations and Data Analysis: The CFHTLS - Deep Survey	51
4.1	Introduction	51
4.2	CFHTLS: Survey Overview	51
4.2.1	The CFHTLS - Deep Survey	52
4.2.2	Optical Imaging	52
4.2.3	Optical Catalogs	54
4.2.4	Number Counts	54
4.3	Galaxy Properties	57
4.3.1	Photometric Redshifts	57
4.3.2	Optically Derived SFRs and Stellar Masses	58

4.3.3	Mid-IR Imaging	59
4.3.4	Band Merging: Optical, Mid-IR	60
5	Results From The CFHTLS - Deep Survey	62
5.1	Introduction	62
5.2	Identifying Interacting Galaxies	63
5.2.1	A New Classification Scheme	65
5.2.2	Methodology	66
5.2.3	Classification Limits	66
5.3	A Classification Experiment	76
5.4	Recovery Rate at Higher Redshift	76
5.4.1	Method	77
5.4.2	Recovery Rate Results	79
5.5	The Galaxy Interaction Fraction: Sample Descriptions	79
5.5.1	Defining the Interacting and Non-Interacting Samples	80
5.5.2	Redshift Distribution	81
5.6	The Galaxy Interaction Fraction (GIF)	81
5.6.1	Galaxy Interaction Fraction: Interaction Class	82
5.7	Primary Galaxy Interaction Fraction	84
5.7.1	Evolution of the Interaction Fraction	84
5.7.2	Potential Biases	85
5.7.3	GIF: Comparison with Previous Works	86
5.7.4	Interaction Fraction: Luminosity Dependence	89
5.7.5	Interaction Fraction: Luminosity Evolution	90
5.7.6	Interaction Induced Brightening?	91
5.7.7	GIF: Mass Dependence	94
5.8	Galaxy Merger Rate	95
5.8.1	Merger Time-scales	97
5.8.2	Computed Merger Rates	99
5.8.3	Interaction History	99
5.9	Star Formation Rates of Interacting Galaxies	100
5.10	Mid-Infrared Properties of Interacting Galaxies	104
5.10.1	MIPS 24 μ m Sample	105
5.10.2	MIPS Galaxy Interaction Fraction	106
5.10.3	Mid-IR GIF: Luminosity Dependence	108
5.10.4	MIPS Interaction Fraction: Class Breakdown	108

5.10.5	Mid-IR Star Formation Rates	109
5.10.6	Merger-Starburst-AGN Connection?	113
5.10.7	IRAC Colour Selection: AGN Candidates	114
5.10.8	AGN Fractions	116
5.10.9	AGN Fraction: Interaction Type	116
5.11	Summary	117
6	Summary and Future Prospects	119
6.1	Summary of New Results	119
6.2	Future Work	121
6.2.1	Spectroscopic Observations of Close Galaxy Pairs	121
6.2.2	Starburst-AGN Connection: Mid-IR Spectroscopy	122
6.2.3	Comparison to Simulations: Merger Time-Scales	123
Glossary & Acronyms		124
Bibliography		126

List of Tables

2.1	Summary of XFLS Photometric Observations	14
3.1	Close Pair Statistics: XFLS	27
3.2	Morphological Merger Statistics: XFLS	31
3.3	Summary of Merger Rate Studies	36
4.1	CFHTLS-Deep Survey Field Locations	53
4.2	CFHTLS-Deep: Magnitude Limits	53
4.3	CFHTLS-Deep: Final Stacks	53
4.4	D1-SWIRE Sensitivities	60
5.1	Classification Scheme I	68
5.2	Classification Scheme II	69
5.3	Breakdown of Interacting Galaxies	70
5.4	Classification Experiment Coding	77
5.5	Inferred Galaxy Interaction Statistics as a Function of Interaction Type	82
5.6	Inferred Galaxy Interaction Statistics	86
5.7	Galaxy Interaction Statistics: Luminosity Limits	92
5.8	Galaxy Interaction Statistics: Mass Dependence	95
5.9	MIPS Galaxy Interaction Statistics	107
5.10	Fraction of MIPS Galaxies with AGN Signatures	117

List of Figures

1.1	Images of Long Tidal Tails	2
1.2	Simulations of the SFR for Merging Galaxies	4
1.3	Evolution of the Comoving IR Energy Density	6
2.1	The XFLS $24\mu\text{m}$ Mosaic	12
2.2	The XFLS ACS (F814W) Mosaic	13
2.3	Stellarity <i>vs.</i> Magnitude	15
2.4	Spectroscopic Completeness	16
2.5	Colour-Colour Plot: MIPS, Non-MIPS, & Spectroscopic Sample	18
2.6	XFLS Spectroscopic Redshift Distribution	19
2.7	XFLS $24\mu\text{m}$ Flux Distribution	20
3.1	MIPS & Non-MIPS Pairs Redshift Distribution	25
3.2	Examples of XFLS Paired Galaxies	28
3.3	The Field Corrected Pair Fraction	29
3.4	Examples of Morphologically Classified Mergers	31
3.5	XFLS Merger Fraction	32
3.6	Morphological Properties of Close Pairs	33
3.7	Merger Rate: Close Pairs and Mergers	38
3.8	IR Luminosity Correlations for Local Galaxies	39
3.9	XFLS LIRG Sensitivities	39
3.10	Total L_{IR} vs. Redshift: Pairs, Mergers and AGN	42
3.11	IRAC Colour-Colour Plot: AGN Identification	43
3.12	IRAC Colour-Colour Plot: XFLS	44
3.13	L_{IR} Density from Mergers	45
3.14	IR Luminosity and Star Formation Rates of LIRGs	47
4.1	D2 i' -band Image Outlining Masked Regions	55
4.2	Schlegel Dust Maps: D1 and D2	56

4.3	D1 and D2 <i>I</i> -band Number Counts	57
4.4	Spectroscopic vs. Photometric Redshifts	59
4.5	D1/SWIRE 24 μ m Image	61
5.1	Montage of Interacting and Merging Systems	63
5.2	Extraction of Tidal Tailed Galaxies	64
5.3	<i>i'</i> Magnitude Distributions for CFHTLS-D1 and D2	65
5.4	Fraction of Classifiable Galaxies as a Function of Magnitude	67
5.5	Examples from CFHTLS-Deep Catalog of Interacting Galaxies	71
5.6	Recovery Rate of Redshifted Tidal Features	80
5.7	Redshift Distribution: Interacting and Non-Interacting Galaxies	81
5.8	Galaxy Interaction Fraction: Class	83
5.9	CFHTLS-Deep: The Galaxy Interaction Fraction	87
5.10	GIF: Comparison	88
5.11	Absolute <i>g'</i> -Band Luminosity: Interacting and Non-Interacting Galaxies	89
5.12	Interaction Fraction: Optical Luminosity Dependence	91
5.13	M_G Distribution for Interacting Galaxies	93
5.14	Stellar Mass vs. Redshift: CFHTLS	94
5.15	Interaction Fraction: Stellar Mass Dependence	96
5.16	Asymmetry Evolution in a Merger	98
5.17	CFHTLS Merger Rate	100
5.18	Interaction History	101
5.19	Average Star Formation Rates: Interacting Galaxies	102
5.20	Star Formation Rate Distributions	103
5.21	Optical-to-Radio SED of Starbursts	104
5.22	24 μ m Distribution of Interacting and Non-Interacting Galaxies	105
5.23	The 24 μ m Galaxy Interaction Fraction	107
5.24	GIF: IR Luminosity Dependence	109
5.25	The MIPS GIF: Interaction Class	110
5.26	IR Luminosity and Star Formation Rates of LIRGs	111
5.27	Comparison of SFR_{opt} and SFR_{IR}	112
5.28	Distribution of SFR_{IR} : Field and Interacting	113
5.29	IRAC Colours of MIPS Detected Interacting and Field Galaxies	115
6.1	Examples of IRS Merger Candidates	122

Chapter 1

Introduction

For much of the 20th century galaxies were thought to evolve in isolation, their shape uniquely determined by the initial conditions under which they formed. As larger areas of the sky were explored, the number of galaxies with peculiar appearances and close companions grew. This began to call into question the idea that galaxies were "island" Universes, evolving unaffected by one another. Many of these peculiar galaxies exhibited long luminous plumes and tails. It was not until the early 1970's that a compelling alternate picture of galaxy evolution began to gain acceptance. Toomre & Toomre (1972), among others, suggested that gravitational interactions between galaxies can not only explain some of the striking tails and bridges observed, but also the idea that mergers and interactions can trigger bursts of star formation.

In the preface of Arp's *Catalog of Interacting Galaxies*, Arp noted that it had been forty years since the discovery that galaxies were independent stellar systems, and yet little was known as to the mystery of how they formed and evolved. Another forty years have since passed, and although we now know a great deal about our Universe, a complete understanding of the origin and evolution of galaxies remains elusive. The work presented in this thesis attempts to contribute by studying how galaxy-galaxy interactions and mergers not only reshape morphological appearances but also their role in triggering new phases of a galaxy's life cycle such as episodic starbursts and nuclear activity, over the last \sim 6 Gyrs.

1.1 Galaxy Mergers and Interactions

Hierarchical models and observations show that galaxy mergers and interactions play a key role in galaxy assembly and star formation, but to what extent is still a matter of debate. In order to investigate this further, an understanding about the physics involved in these encounters and their effects on observable properties is warranted.

1.1.1 Dynamics of an Encounter

Galaxies themselves are large gravitationally bound systems containing stars, interstellar gas, dust, and dark matter. When two galaxies experience a close encounter they feel strong gravitational forces from one another. The tidal fields distort the galaxies radially, drawing out galactic material into long plumes and tails. During an encounter, the total energy of the system is conserved. Dynamical friction is responsible for the galaxies orbital energy decay as it is gradually converted into internal (stellar) motions. This process depending on the masses, relative velocities, and orientation of the encounter may lead to a final coalescence, leaving behind a single merger remnant.

1.1.2 Formation of Tidal Tails

During an encounter the combination of the galaxies' rotation and radial elongation can cause gas, dust and stars to shear off the outer regions, forming two tidal tails: one trailing and one preceding each galaxy. The configuration of the tidal tails and whether a tidal bridge linking the two galaxies is produced is dependent on the geometry of the encounter. A classical nearby (~ 300 million light years) example of two galaxies caught after a first passage with long extended tidal tails and a connecting bridge are "The Mice" (NGC4676) shown in Figure 1.1 alongside a similar yet higher redshift interaction imaged in this work using the CFHTLS-Deep Survey (see Chapter 5 Figure 5.2.3 for more examples).

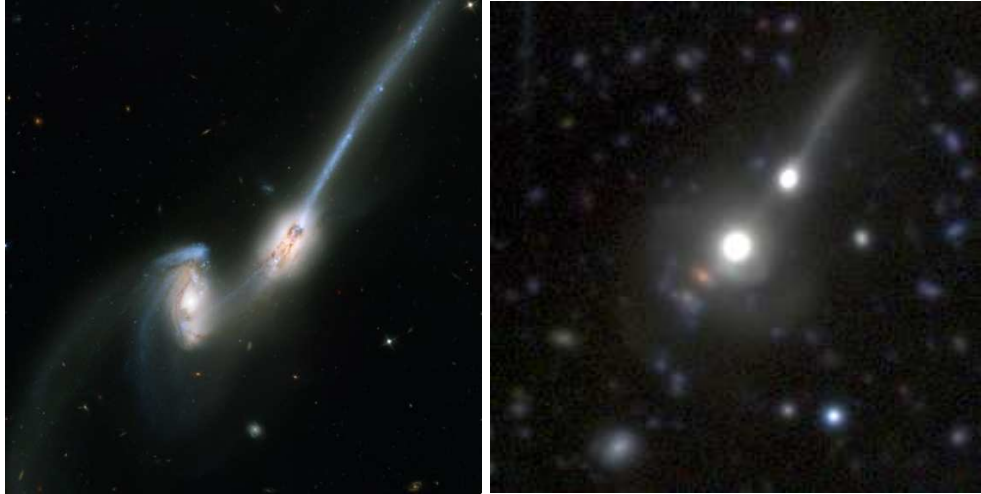


Figure 1.1: Examples of galaxies with long tidal tails and connective bridges. (Left) The famous Mice galaxies (NGC 4676) located 300 million light years away (image from Hibbard & van Gorkom (1996)). (Right) An example of a pair of galaxies identified in the CFHTLS-Deep Survey with similar morphological features but at a higher redshift ($z = 0.4$).

The development of tidal features depends on the resonances between the orbital and ro-

tational motions of the galaxies. For example tidal tails are effectively built during a prograde encounter, when the galaxies' rotation and orbital motion match. However in the case of a retrograde interaction, the making of tidal tails is either minimal or suppressed due the lack of spin-orbit resonances. Simulations, as far back as those done by Toomre & Toomre (1972) have demonstrated that the development of tidal tails during galaxy encounters are predominantly a kinematic effect.

1.1.3 Identifying Mergers

Since galaxy interactions occur over such a large timescale, hundreds of million or billions of years, observers are able to catch galaxy interactions at all stages of the merger process. The commonly applied identification techniques are, the “close pairs” and morphological methods. Morphological approaches can include quantitative measurements of a galaxy’s asymmetry (Abraham et al. 1996a,b; Conselice et al. 2003), as well as qualitative (visual) methodologies (e.g Le Fèvre et al. 2000; Bundy et al. 2004; Bridge et al. 2007a), and both are more likely to probe later stages of the merger sequence. In contrast, early stage or pre-mergers can be identified by carefully searching for close companions, regardless of morphological appearance (Patton et al. 2000; Lin et al. 2004; Bridge et al. 2007a, to name a few). It must be noted that different merger selection criteria probe different stages of the merger process (see Figure 1.2). There should be some overlap between these techniques if galaxy pairs are close enough to have induced strong tidal interactions, but galaxies in pairs could also have normal morphologies.

1.1.4 Starbursts and AGN in Interacting Galaxies

Larson & Tinsley (1978), using a sample drawn from the Arp Atlas of Peculiar Galaxies (1966), first showed that disturbed galaxies exhibit a wide range of colours, with a larger fraction having bluer colours, compared to normal looking field galaxies, suggestive of enhanced star formation. It is clear that the gas in colliding galaxies can be greatly affected. During an interaction gas can be driven into the centers of galaxies where shock waves and tidal torques can compress the gas, leading to intense bursts of star formation and the potential feeding of an active galactic nuclei (AGN). Detailed studies of gas-rich mergers in the local universe (e.g., Antennae; see Schweizer 1982) and N-body simulations (Mihos & Hernquist 1996; Barnes 2004) have also revealed evidence for bursts of star formation caused by galaxy collisions. An extreme example of merger enhanced star formation comes from a class of galaxies with very high far-infrared luminosities, discovered in the 1980’s using IRAS (Infrared Astronomical Satellite) (Soifer et al. 1987). They are known as Ultra-Luminous Infrared Galaxies (ULIRGs)

and have $L_{IR} \geq 10^{12} L_\odot$. While interaction-induced star formation is thought to be primarily responsible for ULIRGs, both locally and at high redshift (Sanders et al. 1988; Dasyra et al. 2006), Luminous Infrared Galaxies (LIRGs, $L_{IR} \sim 10^{11} - 10^{12} L_\odot$) appear to have multiple driving mechanisms, merger-induced star formation being only one.

Figure 1.2 shows a numerical simulation by Mihos & Hernquist (1996) illustrating how the star formation rate (SFR) can be affected during a merger of two disk galaxies. Probing the effect interactions have on the star formation rates of galaxies throughout various stages of the merger sequence is a primary goal of this work, and will be discussed in the subsequent chapters.

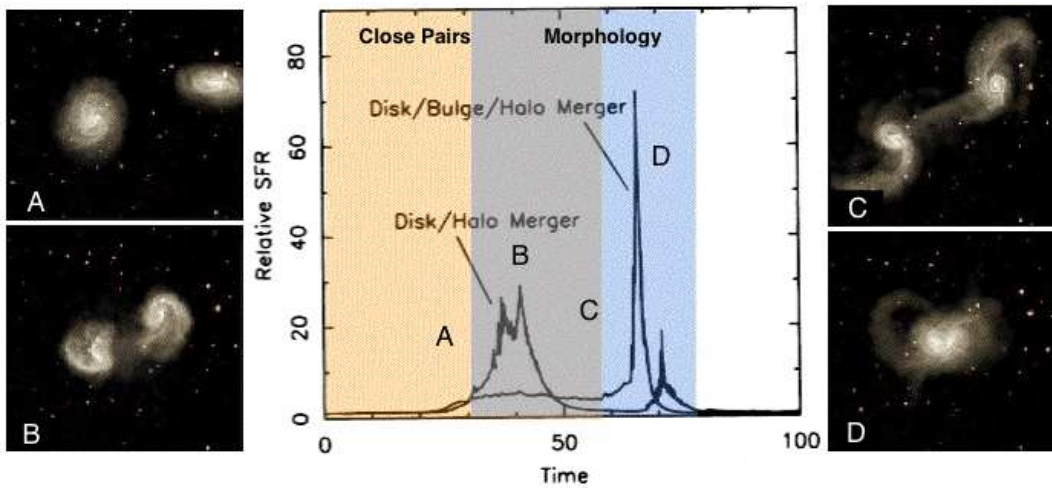


Figure 1.2: Numerical simulation from Mihos & Hernquist (1996) showing the evolution of the star formation rate, relative to isolated disk galaxies during a merger. The x axis is described in time steps (each being ~ 10 million years). The blue shaded area outlines the general scope of the merger sequence that morphological methods are sensitive to, while the orange area marks the close galaxy pairs range. The grey shaded region shows the overlap range of the two techniques. The “A,B,C,D” classifications correspond to the merger stage depicted in the images on the left and right of the figure.

The star formation rate, is a fundamental property of any galaxy at any epoch. To date, most studies probing star formation activity in interacting galaxies have been done in the optical, using broad band colours, spectral measurements of $H\alpha$, and other emission lines. However, a potential complication is that optical measurements can suffer from dust extinction resulting in underestimates of the SFR. A most intuitive alternative for tracing SF is the luminosity of a galaxy in the thermal IR. Mid-IR emission is dominated by reprocessed UV photons from massive young stars that are dust enshrouded, with a potential AGN contribution. In the LIRG population as a whole, contamination from AGN has been found to be less than 20% (Fadda et al. 2002), however their contribution in interacting pairs and mergers still remains unclear. The importance of AGN could be more substantial in interacting systems as gas may

be more efficiently funneled into the inner few kpc's, fueling AGN activity more frequently and potentially more rapidly, than in undisturbed systems.

Locally, 95% of ULIRGs and $\sim 50\%$ of LIRGs are driven by mergers (e.g. Bushouse et al. 2002), which provide the primary means of triggering star formation and AGN activity. However, at higher redshifts, more gas rich systems may produce stars at higher rates under less extreme conditions. Therefore it is logical to expect or at least postulate that a large fraction of the more distant population of LIRGs is also due to interactions as observed locally. Simulations (e.g. Mihos & Hernquist 1996): see Figure 1.2) show that the tidal tail stage may be connected with a burst of star formation and hence a potentially luminous IR phase. Once triggered, the relative contributions of star formation and AGN activity are a subject of debate. The onset of AGN activity could curtail a starburst, due to super-winds or feedback from the AGN. Conversely, there is substantial observational evidence (Priddey & McMahon 2001) that starbursts and AGN activity can be coeval in QSO's and hyper-luminous IR galaxies ($L_{IR} > 10^{13} L_\odot$). To understand these processes in mergers, it is essential to disentangle the contribution of AGN and starbursts to the IR luminosity of LIRGs/ULIRGs at different stages of the merger sequence.

1.1.5 The Cosmic Star Formation History

Over the past decade it has become clear that the average star formation rate per unit comoving volume (CSFR) has declined by an order of magnitude since $z \sim 1$ (Lilly et al. 1996; Madau et al. 1998). A fundamental question, that remains unanswered asks, “what physical processes contributed to this decline?” A wide range of factors may play a role in the drop of the CSFR, such as a potentially declining major merger rate, a decrease in the number of tidal interactions, or perhaps higher gas consumption at high redshifts, to name a few. However determining which processes dominate has proven to be observationally challenging. For example robust measurements of the merger rate have been problematic, typically suffering from small sample sizes, working with a few tens up to a hundred merger candidates. A second, although equally important component for accurate measurements of the merger rate is understanding the average timescale your particular selection technique is sensitive for, which is currently known to only $\sim 0.2\text{-}0.5$ Gyrs (Conselice 2006a). Thirdly, contamination from non-merging systems, can also greatly affect both close pair and morphological methodologies by varying degrees.

Derived close pair and merger fractions can also depend on the redshift range covered, the redshift estimation technique (spectroscopic or photometric), wavelength, and the limiting magnitudes of the surveys. Therefore it is not surprising that merger rate estimates have yielded a broad range of evolutionary strengths, from steeply rising merger rates (Toomre

1977a; Le Fèvre et al. 2000; Patton et al. 2002; Conselice et al. 2003; Kartaltepe et al. 2007) to those indicative of little or no evolution (Carlberg et al. 2000; Lin et al. 2004; Bundy et al. 2004)(see Table 3.3 for a review of the literature).

One thing that is agreed upon in the literature is that most of the star formation in the history of our Universe was enshrouded by dust, making IR bright galaxies a key population to study. Le Floc'h et al. (2005) showed that luminous infrared (IR) galaxies become the dominant population contributing to the comoving infrared energy density beyond ~ 0.6 , and represent 70% of the star formation activity at $z \sim 1$ (see Figure 1.3).

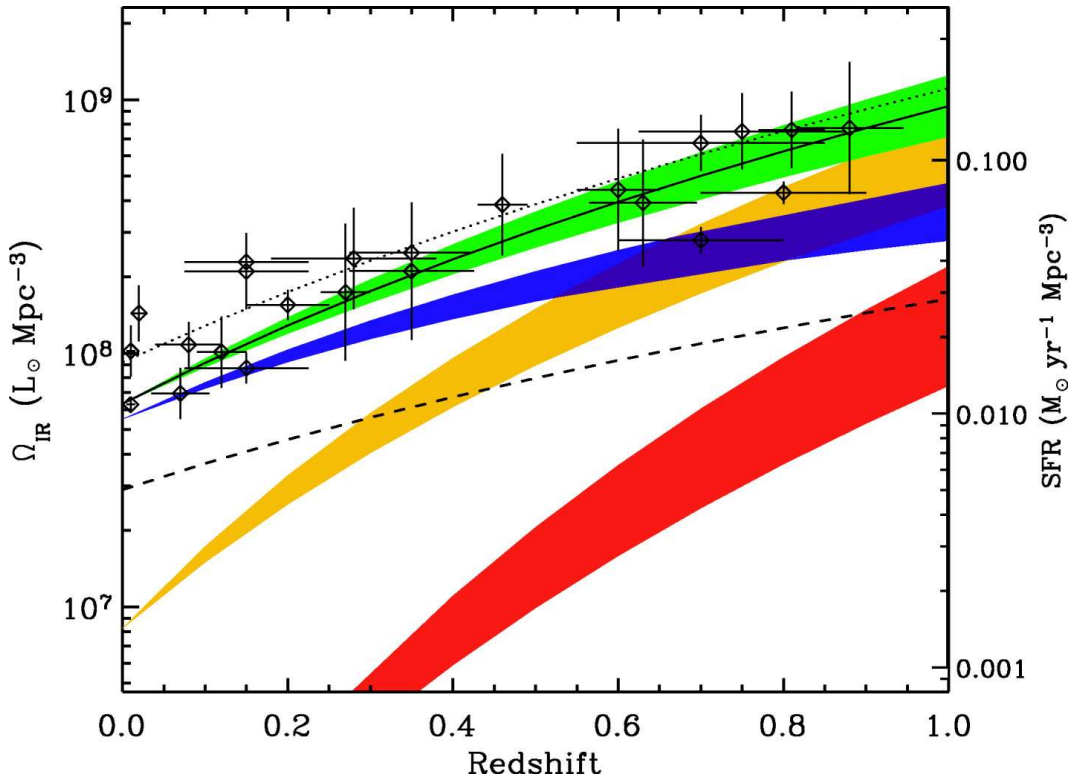


Figure 1.3: Evolution of the comoving IR energy density to $z \sim 1$ from Le Floc'h et al. (2005). The total comoving IR energy density is shown by the green filled region, with respective contributions from low-luminosity ($L_{\text{IR}} < 10^{11} L_{\odot}$) galaxies (blue), LIRGs ($L_{\text{IR}} \geq 10^{11} L_{\odot}$) in orange, and ULIRGs ($L_{\text{IR}} \geq 10^{12} L_{\odot}$) outlined by the red filled regions. The solid line represents the best fit of the total IR luminosity density between $0.1 \leq z \leq 1.0$ and evolves as $(1+z)^{3.9}$. The dotted line represents the best estimate of the total SFR density, summing the SFR measured from the uncorrected UV contribution and the IR-SFR. The dashed line corresponds to the SFR measured by the UV luminosity, uncorrected for dust. The open diamonds correspond to integrated SFR density estimates from the literature, see Hopkins (2004) for the compilation.

At $z \sim 1$ the comoving luminosity density of luminous IR galaxies was 10 times that locally, leading to the important question of the cause of their IR luminosity. Galaxy interactions and mergers have been widely discussed in the literature as being at least in part, a physical process

that could trigger these IR bright phases.

Since luminous IR galaxies appear to play a major role in the CSFR, understanding the physical drivers of their IR luminosity are likely key to discovering its rapid decline from $z \sim 1$ to the present day.

1.2 Dissertation Overview

This dissertation approaches the star formation history and merger evolution of interacting galaxies in two new ways. First, we take advantage of Mid-IR surveys which provide a uniquely unbiased window into the dust enshrouded star forming properties of merging galaxies. An important cosmological issue we can therefore address is, what kind of galaxies host star formation activity at different redshifts and the physical processes that trigger it. By studying the Mid-IR properties of close galaxy pairs and morphological mergers we can reconstruct and quantify their role in the star formation history of the Universe, unaffected by dust, out to $z \sim 1$.

Secondly, we have developed a new classification scheme to securely identify interacting galaxies based on dynamical signatures, such as long tidal tails. By applying our classification method alongside traditional techniques, using both the optical and Mid-IR wavelengths, we were able to address some central questions of galaxy formation and evolution:

- For any given mass and type, what on the average, is a galaxy's star formation and merger history?
- How is the merger history of a galaxy related to its star formation history?
- What role if any, do mergers play in triggering AGN activity?
- What physical processes are responsible for the decline in the CSFR?
- What role do mergers play in driving the IR emission of high redshift luminous IR galaxies?

This thesis aims to provide a better understanding of these pivotal questions of galaxy evolution by compiling one of the largest samples to date of merging galaxies between $0.1 \lesssim z \lesssim 1.0$. By studying their star formation properties and the merger rate as a function of time we can quantify the role interactions and mergers play in triggering star formation, AGN activity, IR luminous phases, and in turn their contribution to the CSFR density.

The dissertation begins with the first ever merger rate analysis of LIRGs and ULIRGs using close galaxy pairs and morphological mergers at moderate to high redshifts. The full

observable merger sequence was identified by searching for galaxies with high quantitatively derived asymmetries, visual indications of interactions, and galaxies in close pairs. The close pair fraction and merger rate of these IR bright systems were examined as a function of time and compared with IR faint galaxies. The role interactions and mergers play in the IR luminosity density and inferred impact on the CSFR density were estimated. The work presented in the first half of the thesis was completed in 2006, published in 2007 (Bridge et al. 2007b), and is detailed in Chapters 2 and 3¹

Small sample sizes have continually plagued close pair and mergers studies, as spectroscopic redshifts are observationally expensive, and wide field surveys are typically done in only 1-3 bands, restricting the use and accuracy of photometric redshifts. Chapter 4 presents a detailed discussion of the deep component of the Canada France Hawaii Telescope Legacy Survey (CFHTLS), which covers 4 sq. degrees in 5 optical bands, providing accurate photometric redshifts, stellar masses, star formation rates and high quality imaging. The CFHTLS survey also has extensive ancillary data from the *Spitzer* SWIRE survey, also outlined in the fourth Chapter.

Chapter 5² presents a new visual classification scheme, developed by the author of this thesis, to confidently identify tidally interacting galaxies. Long tidal tails and bridges are nearly a foolproof signature of imminent mergers. Moreover, tidal tails are a relatively simple, completely dynamical, phenomenon that can be studied in detail with N-body simulations. In spite of these positive features little work on galaxies with tidal tails has been done at high redshift. The reason is simple: tails have a relatively low surface brightness. However, the deep optical imaging and wide area of the CFHTLS-Deep survey is well suited to detecting numerous low surface brightness features allowing the largest catalog of interacting galaxies at moderate to high redshift to be compiled to date. Measuring the tidal tail fraction as function of mass, luminosity, and time is a novel technique applied in this thesis to probe the impact interactions have on galactic evolution. One outcome reported in this thesis is the first statistically confident lower limit of the optical and Mid-IR interaction fraction between

¹The co-authors of the publication presented in Chapter 3 are P. N. Appleton, C. J. Conselice, P. I. Choi, L. Armus, D. Fadda, S. Laine, F. R. Marleau, R. G. Carlberg, G. Helou, and L. Yan. The co-authors from the *Spitzer* Science Center each played a role in some aspect of data acquisition and/or reductions. P. N. Appleton, C. J. Conselice, P. I. Choi, and L. Armus, contributed to some of the ideas that were incorporated into the analysis. Finally, P. N. Appleton, C. J. Conselice, and S. Laine aided in the visual classification of the 24 μ m detected population. The analysis and writing of the paper was carried out by the author of this dissertation. The data acquisition and initial reductions (see Table 2.1 for the relevant papers pertaining to the data) were completed prior to the author of this thesis joining the collaboration.

²The analysis in Chapter 5 is currently being written in paper form, and when submitted for publication will have the following co-authors: R. G. Carlberg, M. Sullivan and D. Le Borgne. M. Sullivan undertook the data reduction of the CFHTLS Deep imaging, while the photometric redshift code was written by D. Le Borgne. Dr. Carlberg contributed to some of the ideas incorporated into this work. The analysis and writing of this chapter and the associated paper in preparation was carried out by the author of this thesis.

$0.1 \leq z \leq 1.0$. Additionally we took advantage of the overlapping area between the Mid-IR SWIRE survey and the CFHTLS-Deep survey to perform a detailed comparison of IR bright and faint interacting galaxies, highlighting their star formation rates and AGN activity.

In the final Chapter, the main results of this thesis are summarized, highlighting the most important contributions this work has made to the study of galaxy mergers and interactions. In closing, projects that are currently underway as well as future directions aimed at improving and extending the work of this thesis are presented.

Chapter 2

Observations and Data Analysis: The Spitzer First Look Survey

2.1 Introduction

This chapter details the data in which this work is partially based (specifically Chapter 3). These include the main *Spitzer* imaging of the XFLS survey, both the Infrared Array Component (IRAC) and data from the Multiband Imaging Photometer (MIPS), ACS imaging from *HST*, spectroscopic data obtained by our group, archival data, and finally ground-based optical and near-IR data obtained through collaborative arrangements.

The *Spitzer* Space Telescope (Werner et al. 2004), NASA’s Great Observatory for infrared astronomy, was launched in August of 2003. *Spitzer* has an 85cm primary mirror operating between 3.6 and 160 μ m with unprecedented sensitivity and better spatial resolution compared to other IR satellites (e.g. *IRAS*, *ISO*). In December 2003, during its first scientific campaign, *Spitzer* completed the extragalactic component of First Look Survey (hereafter XFLS). The XFLS is a 3.7 deg² region centered around R.A.=17^h18^m00^s, decl.=59°30’00”, with a deeper central region of 0.26 deg², called the verification strip. The full XFLS field was chosen to lie within the continuous viewing zone (CVZ), to have no bright radio sources, and minimum cirrus. Observations of this field were taken using all four IRAC channels and the three MIPS bands. The aim of this 67 hour survey using Director’s Discretionary Time (DDT), was to characterize the extragalactic source populations in the Mid-infrared down to sub-millijansky levels. For details of the FLS observation plan and the data release, see <http://ssc.spitzer.caltech.edu/fls>.

The components of the XFLS that have been published by members of our collaboration in peer-reviewed journals, some before C. Bridge joined the group, are listed in Table 2.1. All data used in this analysis was obtained either through published archival surveys or in collaboration with other groups. We will outline the various data sets in the proceeding sections

and the role the author of this dissertation played in their construction.

2.2 The First Look Survey Observations

2.2.1 Mid-Infrared: IRAC Imaging

The IRAC camera on *Spitzer* (Fazio et al. 2004) provides simultaneous 5.12×5.12 arc-minute images in four bands (or channels). Channel 1 is centered at a nominal wavelength of $3.6 \mu\text{m}$, channel 2 at $4.5 \mu\text{m}$, channel 3 at $5.8 \mu\text{m}$ and channel 4 at $8.0 \mu\text{m}$. The data were processed and stacked by the data processing pipeline at the *Spitzer* Science Center (SSC). Detailed descriptions of the reduction process and source extraction can be found in Lacy et al. (2005), which was published before C. Bridge joined the collaboration. The data is currently public and can be acquired through both the *Spitzer* Science Archive and the NASA/IPAC Infrared Science Archive (IRSA).

The main survey field has flux density limits of 20, 25, 100, and $100 \mu\text{Jy}$ at wavelengths of $3.6, 4.5, 5.8, 8.0 \mu\text{m}$ respectively. The deeper verification strip has limits of 10, 10, 30 and $30 \mu\text{Jy}$ respectively. The catalogs produced in Lacy et al. (2005) are $\approx 80\%$ complete and $\approx 99\%$ reliable to the above flux density limits.

The mean positional accuracy using 2MASS sources detected in all four IRAC channels above the flux limits of the catalogs, is $0.25''$, with no measurable mean offset. This uncertainty degrades at faint fluxes due to noise and source confusion. Simulations suggest a positional error of $\sim 1''$, close to the flux limits of the catalog (Lacy et al. 2005).

2.2.2 Mid-Infrared: MIPS Imaging

The Multiband Imaging Photometer for *Spitzer* (MIPS) has three detectors probing 24, 70, and $160 \mu\text{m}$ (Rieke et al. 2004). Due to the lower sensitivities of the longer wavelengths only the $24 \mu\text{m}$ imaging is utilized in this work. The field of view at $24 \mu\text{m}$ is $\sim 5 \times 5$ arc-minute. The MIPS data were also stacked and processed using the SSC pipeline, by the collaboration prior to C. Bridge joining the group. Details of the reduction procedure and catalog construction are described in Marleau et al. (2004) and Fadda et al. (2006). The source catalogs utilized in this thesis had 3σ depths in MIPS $24 \mu\text{m}$ of 0.1mJy .

Errors in the astrometry of the $24 \mu\text{m}$ sources come from both the pointing uncertainty and the positional measurement on the image. The MIPS positional accuracy is also dependent on the signal to noise ratio (S/N) of the source. The 3σ limits of our survey have a positional accuracy of $\sim 2''$, as derived through simulations outlined in Fadda et al. (2006). The $24 \mu\text{m}$ mosaicked images are presented in Figure 2.1 with the ACS coverage outlined.

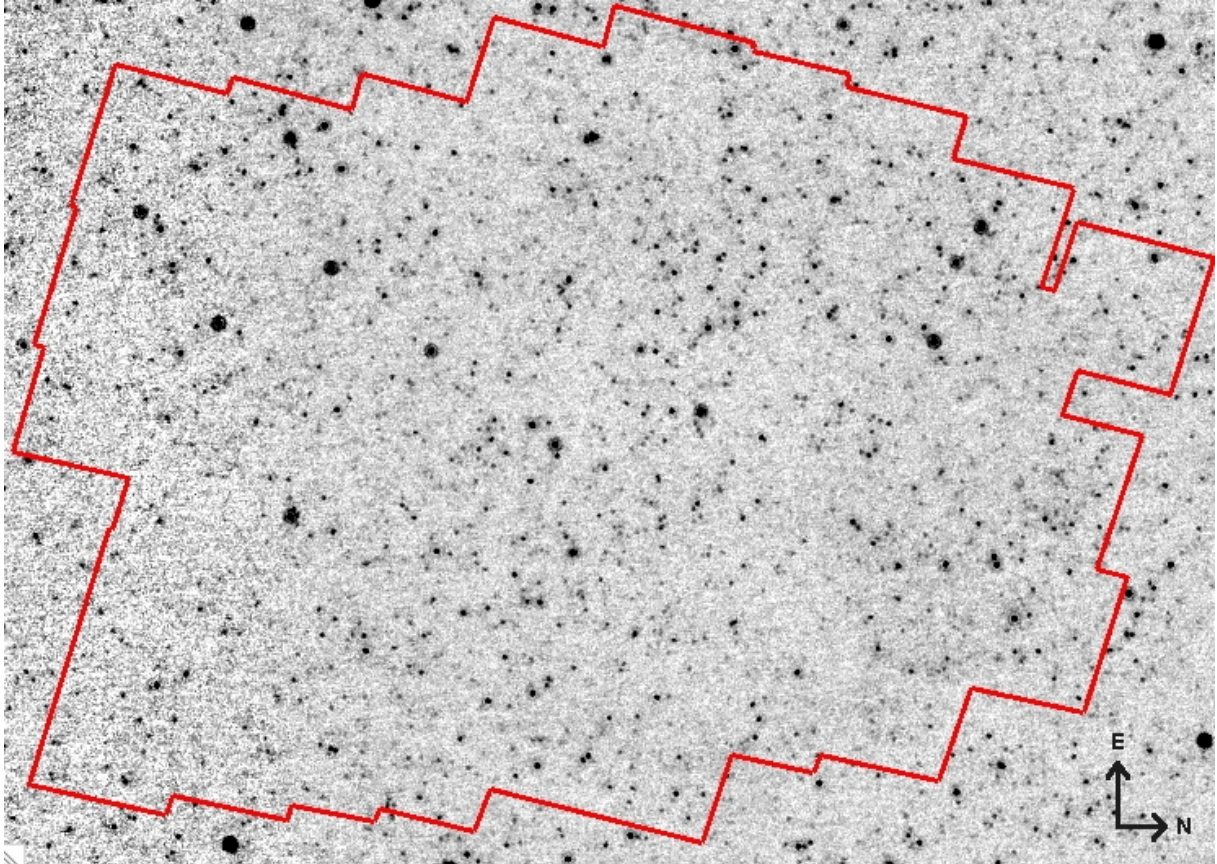


Figure 2.1: The XFLS $24\mu\text{m}$ mosaic (Fadda et al. 2006) that overlaps with the *HST* F814W imaging outlined in red (0.12 square degrees).

2.2.3 Near-Infrared Imaging

The near-IR imaging is only briefly presented as its relevance to this work is solely as a selection criterion that was applied for the spectroscopic follow-up outlined in 2.2.5. Near-infrared observations of a $45' \times 45'$ region centered on the verification region were carried out by the XFLS collaboration using the Wide Field Infrared Camera (WIRC) on the Hale 5.1m telescope at the Palomar Observatory. A median depth of $K_s < 20.2$ (Vega) was achieved. A description of the observations and data reductions are presented in Glassman (2007).

2.2.4 Optical Imaging

Ground based images in u^* , and g' from CFHT's MegaCam reach 5σ depths of 26.2 mags, and 26.5 mags (AB) where they are 50% complete. The imaging is centered on the XFLS verification strip and are detailed in (Shim et al. 2006). Additional NOAO 4-m R band observations down to $R_{AB}(5\sigma) = 25.5$ mag were also obtained by the collaboration (Fadda et al. 2004).

The optical component primarily used in this thesis comes from the 0.12 deg^2 of ACS-

HST F814W imaging of the verification strip (see Figure 2.2). This data was obtained with 50 pointings in parallel with NICMOS observations of the XFLS (Marleau 2007; Storrie-Lombardi 2007). Object detection and photometry were performed using SExtractor (Bertin & Arnouts 1996). Particular care was taken to ensure accurate de-blending of galaxies in close proximity to one another, while avoiding detections of substructure within a single galaxy, consistent with other reductions of *HST* imaging with close galaxy pairs in mind (Patton et al. 2005). There were $\sim 59,000$ sources extracted within the $F814W_{AB}$ band (hereafter extracted magnitudes are referred to as I_{AB}). We compared our number counts to those from the Hubble Deep Field (HDF) North and South and determined a limiting magnitude of $I_{AB} \sim 27.4$. Table 2.1 summarizes the photometric observations used in this work.

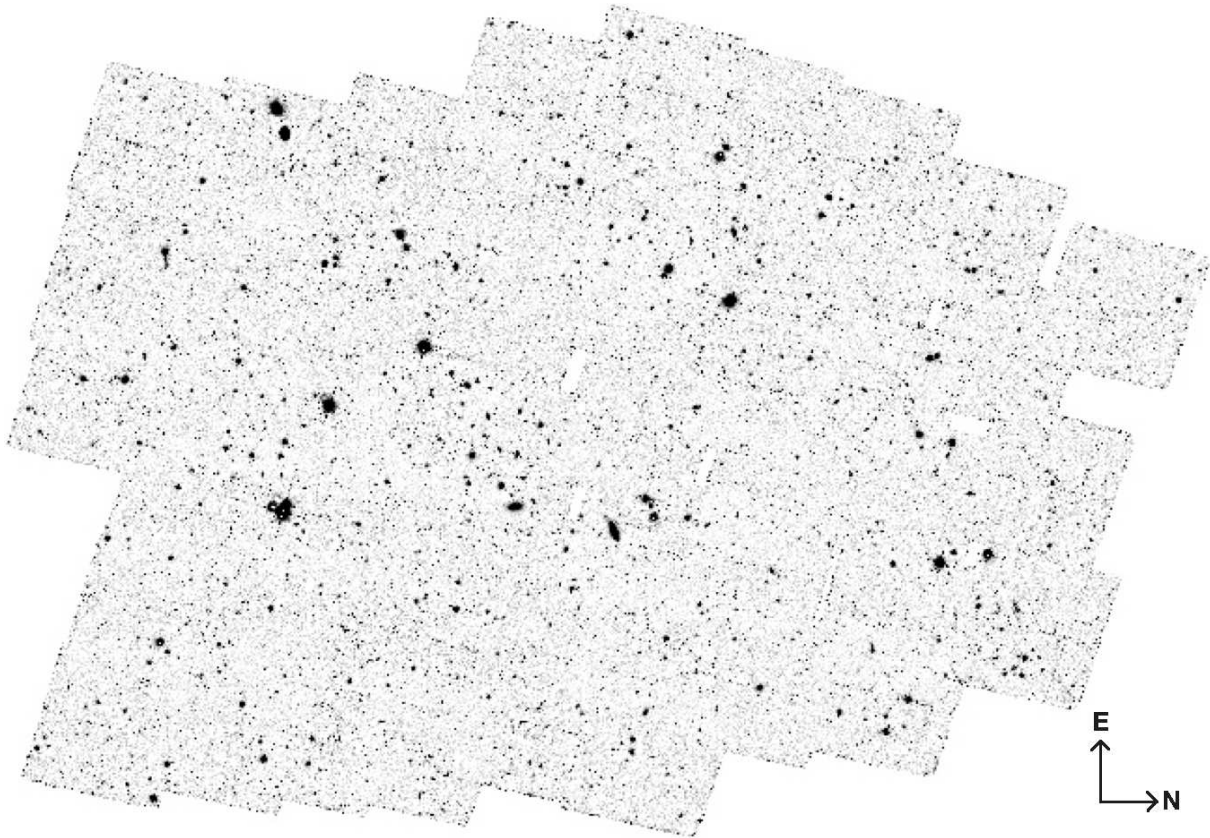


Figure 2.2: The XFLS F814W ACS mosaic. The mosaic is constructed from 50 individual ACS pointings. The image scale is $0.05''/\text{pixel}$ and the image covers 0.12 deg^2 .

The ACS source catalog from Marleau (2007) did not utilize the ACS zeropoints, or remove stellar contamination. To calibrate the magnitudes we applied the following equation:

$$mag_{app} = mag^* + zeropoint \quad (2.1)$$

where mag^* is the original apparent magnitude using the “MAG AUTO” parameter in

Table 2.1: A summary of photometric observations in the XFLS used in the subsequent chapter of this thesis.

Instr./Tele.	Band	PSF (FWHM)	λ_{eff}	Lim. Mag.	Publication
Megacam / CFHT	u^*	0.85''	3740 Å	26.2 (AB) [5 σ]	Shim et al. (2006)
Megacam / CFHT	g'	0.85''	4870 Å	26.5 (AB) [5 σ]	Shim et al. (2006)
LFC/Palomar-Hale	g'	1''	4660 Å	—	Glassman (2007)
LFC/Palomar-Hale	i'	1''	7680 Å	—	Glassman (2007)
Mosaic-1 / KPNO-Mayall	R	1.1''	6440 Å	25.5 (AB) [5 σ]	Fadda et al. (2004)
ACS / HST	$F814W$	0.1''	8330 Å	27.4 (AB)	Marleau (2007)
WIRC / Palomar-Hale	K_s	1''	2.14 μ m	20.2 (Vega)	Choi et al. (2006)
IRAC / Spitzer	Channel 1	1.8''	3.6 μ m	10 μ Jy [5 σ]	Lacy et al. (2005)
IRAC / Spitzer	Channel 2	2.0''	4.5 μ m	10 μ Jy [5 σ]	Lacy et al. (2005)
IRAC / Spitzer	Channel 3	2.0''	5.8 μ m	30 μ Jy [5 σ]	Lacy et al. (2005)
IRAC / Spitzer	Channel 4	2.0''	8.0 μ m	30 μ Jy [5 σ]	Lacy et al. (2005)
MIPS / Spitzer	Band 1	5.7''	24 μ m	100 μ Jy [3 σ]	Fadda et al. (2006)

source extractor. The final zeropoint is derived by,

$$\text{zeropoint} = zpt + 2.5 \log(\text{exposure time}) \quad (2.2)$$

since the image is in total counts. The “zpt” parameter is the zeropoint determined for the F814W filter on ACS based on constant flux per unit frequency and is found to be 25.937 $mags_{AB}$ (STSCI 1998).

The separation of stars and galaxies in deep observations is always challenging. To address the stellar contamination in the ACS photometric catalog we utilized the stellarity index determined from SExtractor as defined by the “CLASS STAR” parameter. The stellarity index is computed for a given object from the comparison of its luminosity profile with the natural “fuzziness” of the object. SExtractor gives a stellarity index ranging from 1 (star-like objects) down to 0 for extended galaxies. This quantity can be a secure stellar identifier for bright objects but breaks down at faint magnitudes. A variety of CLASS STAR values have been used in the literature, traditionally ranging from 0.9 to 0.97 (Ferguson et al. 2004; Benítez et al. 2004). Stellarity indices have also been applied as a function of magnitude (Shim et al. 2006). Our adopted value for the star/galaxy separation is a conservative one (CLASS STAR ≥ 0.90 determined to be a star), and the stellarity index distribution is shown in Figure 2.3, where the red points were flagged and removed as stellar contamination. Such a conservative value for the stellarity index was chosen to ensure that galaxies were not removed from the sample, however in turn there remains some stellar contamination, as shown in Figure 2.3. This is acceptable since we visually inspect all galaxies identified as close pairs or mergers and remove any remaining stellar like objects.

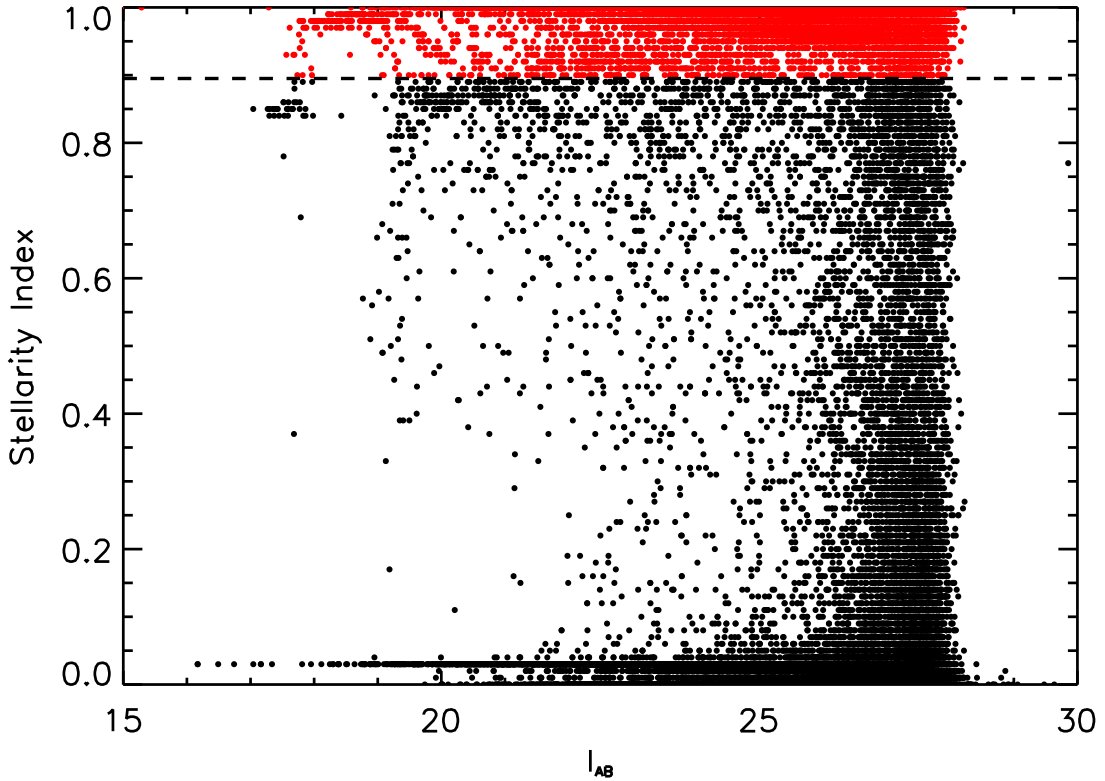


Figure 2.3: Distribution of the values from the CLASS STAR parameter as a function of magnitude (F814W). The dashed lines represents the cut used to separate stars (stellarity index ≥ 0.90 ; shown in red) and extended galaxies type objects (stellarity index < 0.90 ; black circles).

2.2.5 Spectroscopic Observations

The redshifts used in this study were determined exclusively from optical spectroscopy, prior to C. Bridge joining the group. We did however compile the spectroscopic catalog by cross-correlating the ACS sample, limited to $I_{AB} \leq 26.5$ ($N \sim 29,000$) with various FLS spectroscopic datasets. The vast majority of the included redshifts ($\geq 97\%$) were obtained with the Deep Imaging Multi-Object Spectrograph (DEIMOS) on the W.M. Keck II 10-m telescope; however, the final sample also included a few redshifts based on Sloan Digitized Sky Survey (SDSS) and WIYN Hydra/MOS (Marleau et al. 2006 in prep) spectra.

The primary spectroscopic sample in the XFLS Verification region was the result of two DEIMOS campaigns that bracketed *Spitzer's* launch. The selection criteria for these campaigns are summarized below. For the 2003 pre-launch campaign, targets were selected based on NIR (K_s) and optical (g, R, i) colors. The primary sample included sources with $K_s < 20.2$, $R > 19.0$ and a g, R, i color selection that restricted the numbers of low redshift ($z \leq 0.6$) sources. For

the 2004 post-launch campaign, a purely 24 μ m selected sample ($f_{24} > 120 \mu\text{Jy}$) was targeted for follow-up. The combined I_{AB} distribution of targeted and detected sources is shown in Figure 2.4 (*top*) along with the cumulative redshift identification efficiency (*bottom*). The overall spectroscopic completeness (defined here as the fraction of targeted sources with high quality redshifts) is $\sim 70\%$ for the full sample and $\sim 80\%$ for sources with $I_{AB} < 25.0$. For a more detailed description of the observing strategy, primary selection criteria and the overall flux distributions see Choi et al. (2006).

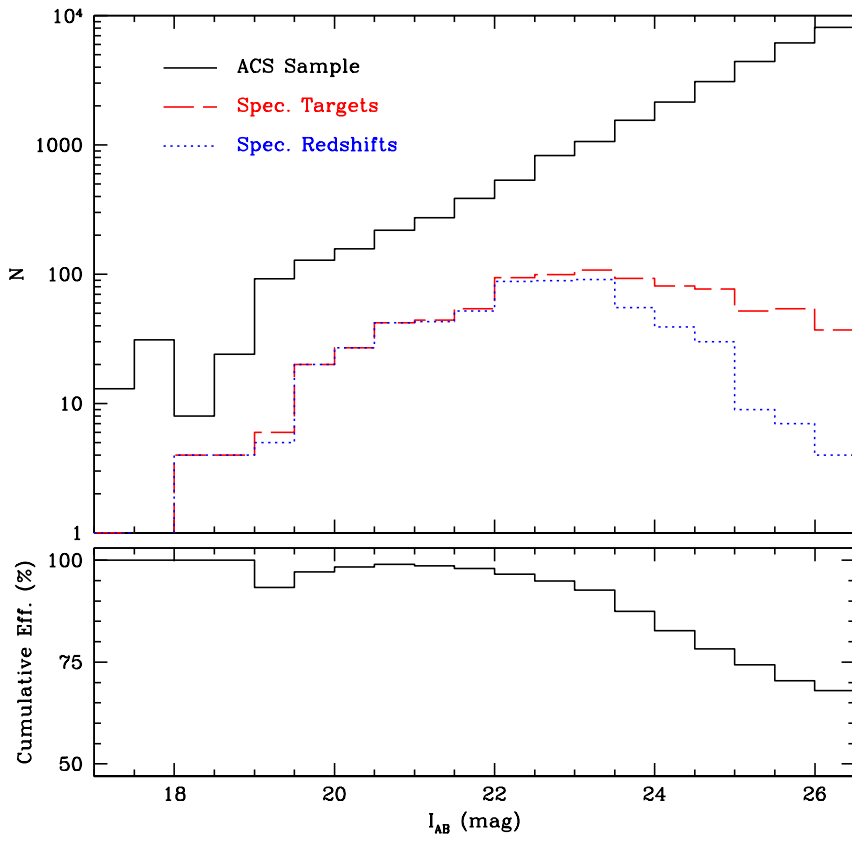


Figure 2.4: (*Upper*) The I_{AB} *mag* distribution for the XFLS sample (solid), the sample targeted for spectroscopy (long-dash), and those where spectroscopic redshifts were acquired (dotted). (*Lower*) The cumulative redshift identification efficiency. The overall spectroscopic completeness is $\sim 70\%$ for the full sample and $\sim 80\%$ for sources with $I_{AB} < 25.0$.

2.3 The Catalog

2.3.1 Band Merging

We performed a process called “band merging” which combines different data sets covering various wavelengths into a single database matching objects to their multi-wavelength counterparts. This is a relatively simple process at optical wavelengths since the resolution of the images is similar. However, as you go to longer wavelengths there can be complicated situations where multiple optical counterparts are found for one Mid-Infrared source because of the large PSF and errors in the Mid-Infrared astrometry. This error which does depend on the signal-to-noise of the sources comes from the measurement on the image and from the pointing uncertainty. As mentioned in section 2.2.2 the error in the astrometry (σ) for MIPS 24 μm detections is $\lesssim 2''$ (assuming a SNR ratio of 3), as derived by:

$$\sigma^2 = \sigma_{ext}^2 + \sigma_{point}^2, \quad (2.3)$$

where the pointing error $\sigma_{point}=0.3''$ and the extraction error (σ_{ext}) estimated from simulations (Fadda et al. 2006) follow:

$$\log(\sigma_{ext}) = 0.74 - 1.06 \log(S/N). \quad (2.4)$$

Using the full 4 square degree MIPS catalog from the XFLS we selected 24 μm sources within the area covered by the ACS imaging ($\sim 0.12 \text{ deg}^2$). In order to correlate the MIPS objects with those identified in the optical we first cross-identified sources from the MIPS 24 μm sample to the IRAC catalog using a tolerance radius of 2.0''. This choice of radius was primarily motivated by the 24 μm astrometric uncertainty and confirmed by visual inspection. We then cross-correlated the IRAC/MIPS catalog to the ACS sample which we band merged with u*, g' and R requiring a positional agreement of $\leq 1''$. When multiple optical counterparts were identified for a *Spitzer* source, we selected the closest object. Ultimately we found 1155 ACS sources also detected by IRAC and MIPS at 24 μm .

The spectroscopic catalog was then merged with the photometric catalog by cross-correlating the ACS sample, limited to $I_{AB} \leq 26.5$ ($N \sim 29,000$) with the XFLS spectroscopic dataset. Cross-correlation of the band-merged photometric catalogs with the redshift samples result in a data set of 476 sources with $I_{AB} < 26.5$ between $0.2 \leq z \leq 1.3$. Of those, 245 (51%) are MIPS 24 μm -detected with a measured $L_{IR} \geq 5.0 \times 10^{10} L_\odot$ (see 3.7 for details on how the L_{IR} is calculated). The remaining 231 (49%) were undetected at 24 μm . It must be noted that although these sources are described as 24 μm non-detections or non-MIPS sources they may just be below the 100 μJy limit of our survey. Regardless, they can at most be considered MIPS “faint”

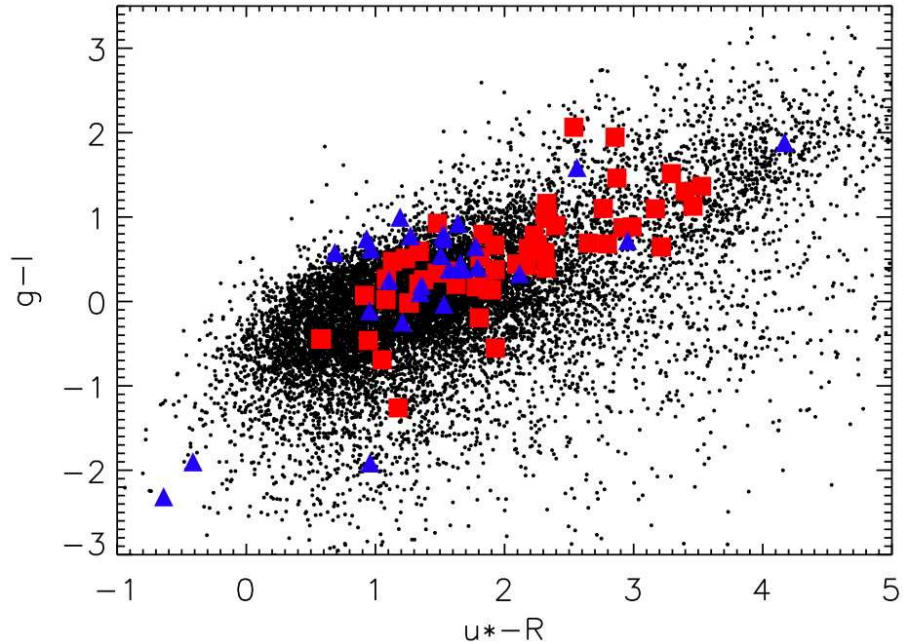


Figure 2.5: Color-color plot where red squares depict the $24\mu\text{m}$ detected objects with spectroscopic redshifts, while blue triangles show the undetected $24\mu\text{m}$ spectroscopic sample. The black dots represent the full FLS-ACS catalog for comparison. The $24\mu\text{m}$ detected and undetected spectroscopic samples occupy a similar color space. Some objects were not detected in all four bands due to the field coverage, and filter depths.

sources, and are sometimes refer to as such throughout this work.

2.3.2 Colour Properties and Distributions

Since the spectroscopic sample consists primarily of two different observational campaigns with different selection criteria (as described in section 2.2.5) it was important to explore any possible bias this may have on our analysis. Figure 2.5 shows that despite the fact that the MIPS and non-MIPS galaxies were selected differently for spectroscopic follow-up, they have similar colour properties compared to one another and the general field.

The MIPS and non-MIPS samples also have similar redshift distributions (see Figure 2.6). The deficiency of sources with spectroscopic redshifts at ~ 0.5 from the full MIPS detected sample (black dotted histogram; Figure 2.6) is a result of the colour criteria used to preferentially select objects with redshifts > 0.6 in the first spectroscopic campaign. After *Spitzer's* launch, $24\mu\text{m}$ sources were spectroscopically targeted with no colour criteria imposed, resulting in the abundance of low redshift ($z \sim 0.2$) galaxies. However, since an L_{IR} limit is imposed throughout the analysis the $z \sim 0.2$ peak is not factor, as most of theses galaxies have low IR luminosities, below $L_{IR} \geq 5.0 \times 10^{10} L_\odot$ (see blue solid line;Figure 2.6).

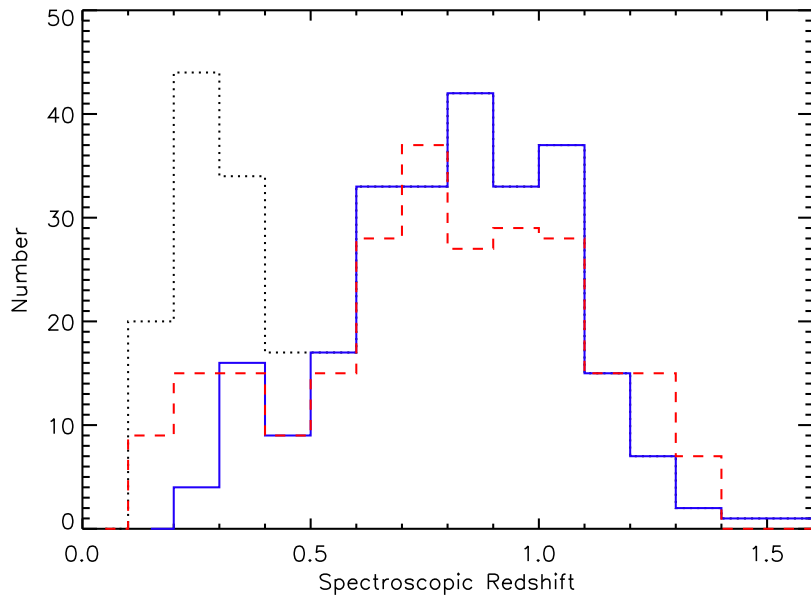


Figure 2.6: Spectroscopic redshift distribution of the full MIPS sample (dotted, black and overlaps with blue at $z > 0.5$), the undetected MIPS spectroscopic sample (red, dashed), and the L_{IR} limited MIPS sample ($L_{IR} \geq 5.0 \times 10^{10} L_\odot$) (blue, solid).

It is also evident from Figure 2.7 that the MIPS spectroscopic sample probes the same $24\mu\text{m}$ flux ranges as the MIPS field. Ultimately, the MIPS and non-MIPS spectroscopic samples show no strong differences in their optical colours or redshift distributions. Now that we are confident that the a fair comparison can be made between the MIPS detected and undetected spectroscopic samples, we can proceed with the analysis of these intriguing galaxies.

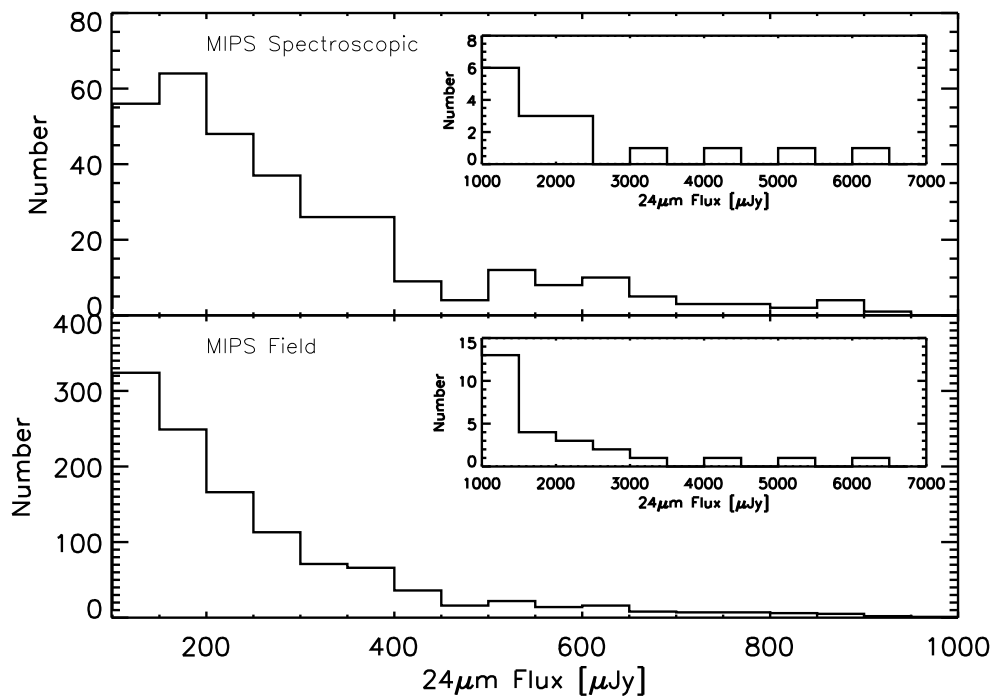


Figure 2.7: (Upper panel) The 24 μm flux distribution for the MIPS spectroscopic sample. (Lower panel) depicts the 24 μm flux distribution for the XFLS MIPS field galaxies. Insets show the higher flux distributions for each sample.

Chapter 3

Results from the Spitzer First Look Survey

3.1 Introduction

In this chapter the main results from the XFLS pertaining to galaxy pairs and mergers are presented. The catalogs of close galaxy pairs and morphologically defined mergers are discussed. From these data the merger fraction and first ever close pair fraction are measured as a function of redshift (out to $z \sim 1.2$), while considering the Mid-infrared properties of these merging systems. The majority of the work presented in this Chapter appeared in Bridge et al. (2007a)¹ of which C. Bridge is the first author.

In the discussion that follows, any calculation requiring cosmology assumes, $\Omega_M = 0.3$, $\Omega_\Lambda = 0.70$, and $H_0 = 70 \text{ km s}^{-1} \text{ Mpc}^{-1}$.

3.2 Sample Identification

To properly constrain the role interactions and mergers play in galaxy evolution, all stages of the process should be considered. Typically, merger history analyses utilize either pair or structural methods. Galaxies in close pairs are considered pre-mergers, or systems undergoing recent interactions, while morphological or structural methods find galaxies at a slightly later stage, after the first passage and possibly dynamically relaxing (recall Figure 1.2).

When discussing the pair fraction, and inferred merger rates, it must be noted that these

¹The co-authors of this paper are P. N. Appleton, C. J. Conselice, P. I. Choi, L. Armus, and R. Carlberg who contributed to some of the ideas that were incorporated into the analysis. The analysis and writing of the paper was carried out by the author of this dissertation. The data acquisition and initial reductions (see Table 2.1 for the relevant papers pertaining to the data) were completed prior to C. Bridge joining the collaboration.

measurements are highly dependent on the techniques, selection criteria, and wavelength used to identify ongoing mergers, especially for galaxies at high redshifts. Merger rate studies have primarily been undertaken in the optical, (refer to Table 3.3) however probing longer wavelengths, specifically the Mid-IR, allows us to investigate the star forming properties of these systems, uninhibited by dust. Due to the comparatively limited spatial resolution of current Mid-IR instruments like *Spitzer* (compared with optical imaging), searching for close galaxy pairs or morphological signatures of an interaction at Mid-IR wavelengths is restricted to the nearby Universe. However, we can correlate optically-selected pairs and mergers with global Mid-IR properties and investigate the IR activity in these systems out to high redshifts.

In this work we applied both pair and structural techniques in order to identify galaxies ranging from early (close pairs) to late stage mergers. The identification techniques are described in the proceeding sections.

3.2.1 Close Galaxy Pairs

The first method, typically called the “close pair method”, counts the number of galaxy companions within some projected separation, usually no more than $20\text{-}30 h^{-1}\text{kpc}$, from a host galaxy with a known redshift. The projected separation (r_{proj}) translates into an angular separation, θ , in arcseconds using the equation,

$$\theta = \left(\frac{k}{r_{\text{proj}}(1+z)} \right) \left(D_H \int_0^z \frac{dz}{\Omega_m(1+z)^3 + \Omega_\Lambda} \right), \quad (3.1)$$

where D_H is the Hubble distance, k is the conversion factor for the angular separation to be in units of arcseconds (''), and r_{proj} is the projected separation (this work uses $20 h^{-1}\text{kpc}$).

A maximum magnitude difference (Δm) between the host and companion can also be applied to select more equal mass major mergers (Le Fèvre et al. 2000). This operational close pair definition has been widely used to study the pair fraction of galaxies (Patton et al. 1997; Bundy et al. 2004; Lin et al. 2004) (see Table 3.3 for a more complete summary of works). When redshift information is known for both the primary and companion, a relative velocity difference can also be imposed to select companions with low peculiar velocities, hence increasing the likelihood of selecting paired systems undergoing imminent mergers. However, having redshift information for both close pair members is observationally expensive, and the handful of studies with this information typically suffer from small sample sizes (Patton et al. 2002; Bundy et al. 2004; Lin et al. 2004).

3.2.2 Morphological Mergers

A complementary technique is to select merging systems based on morphological indicators either by overall appearance (Le Fèvre et al. 2000) or computational measurements such as asymmetry (A), and clumpiness (S) of a system (Abraham et al. 1996b, 2003; Conselice et al. 2000, 2003), or the Gini coefficient (G), and M_{20} parameter (Abraham et al. 2003; Lotz et al. 2006).

To explore the structural components of galaxies in our sample we used the CAS (Concentration, Asymmetry, Clumpiness) quantitative classification system (Conselice 1997; Conselice et al. 2000, 2003), along with visual classifications. The basic computation of asymmetry involves rotating and subtracting a galaxy image from itself and comparing the summation of the absolute value of these residuals to the original galaxy's flux. An important aspect of rotational asymmetry is the choice of a rotation center. For large galaxies slight variations of the center of rotation can result in substantially different asymmetry values. However, as the scale of the galaxy becomes smaller the need for precise centering decreases. To address this issue, the center of rotation is defined to be the position that yields a minimum asymmetry value (for $\phi = 180^\circ$). The central brightest pixel of a galaxy is chosen to be the initial center, and the asymmetry is computed again for centers at eight surrounding points in a 3x3 grid.

A second correction that is typically applied addresses the issue of uncorrelated noise. Since rotational asymmetry is essentially a pixel-by-pixel difference algorithm it can be affected by noise. A correction is determined by performing the asymmetry measurement on a blank piece of sky in the image, and then subtracting it from the value measured for the object. Ultimately, this formula can be written as,

$$A = \min\left(\frac{\sum |I_o - I_\phi|}{\sum |I_o|}\right) - \min\left(\frac{\sum |B_o - B_\phi|}{\sum |B_o|}\right) \quad (3.2)$$

where B represents pixels in the blank region of sky, and I represents those from the object. It has been established that asymmetry can be well-measured for galaxies down to $I_{F814W} \leq 24$ (Conselice et al. 2000), as is the case for our sample. Galaxies with a high level of asymmetry ($A > 0.35$) are typically considered to be consistent with merger activity (Conselice 2003).

Visual inspection is another method of identifying merging galaxies, although it can be somewhat subjective. Nevertheless, it remains a viable technique, especially if the features of interest are tidal tails, or galaxies with disturbed appearances which can be identified with a high level of confidence. Galaxy merging routinely reveals visual evidence by way of long tidal tails or plumes, bridges between objects, and double nuclei. Quantitative methods (using asymmetry etc.) rely on each pixel being assigned to either the background or a particular object. When a feature, such as a tidal tail has a low surface brightness it can mistakenly be

determined to be a separate object or in very faint cases not a detection at all. This can lead to an underestimate of an object’s asymmetry, and a potentially unidentified merger (see section 5.2 for an example). Visual classification is a technique that can be used to identify those mergers that were not found using the close pair or quantitative morphological methods. The specifics of the visual classification scheme used in the XFLS are discussed in section 3.4.

Ultimately, when considering the merger sequence and the various techniques that identify these systems it is important to consider that each is sensitive to a slightly different merger time-scale. When normalized by their respective merger time-scales a more complete picture of the galaxy merger sequence can be achieved, and the level of agreement between identification techniques is testable. Results from the application of these selection techniques is presented in the proceeding sections.

3.3 Close Pair Results

3.3.1 Close Pair Statistics

We applied the close pairs technique to identify the average number of close companions per galaxy, hereafter N_c (similar to N_c as defined by Patton et al. (2000)). This measurement is similar in nature to the pair fraction when there are infrequent triples or higher order N-tuples. Since this is the case here, N_c will be occasionally referred to as the pair fraction. Companions were selected using a standard operational close pair definition of $5h^{-1}\text{kpc} \leq r_{\text{proj}} \leq 20h^{-1}\text{kpc}$, and an optical magnitude difference (Δm) ≤ 1.5 (in I -band) compared to the host galaxy, to select nearly equal mass major mergers. The term “host” or “primary” galaxy are both used to reference the pair member with a measured redshift. The inner radius of $5h^{-1}\text{kpc}$ is applied to avoid detection of substructure within a galaxy, while the outer $20h^{-1}\text{kpc}$ limit represents the radius within which satellites are expected to strongly interact with the halo of the host and merge within 0.5-0.9 Gyrs (Patton et al. 1997; Conselice 2006b). We find 87 close pairs out of the 476 galaxies which have a spectroscopic redshift.

To study the fraction of IR-bright galaxies in pairs, we split the pair sample into two sub-sets: those which were detected and those undetected with MIPS at $24\mu\text{m}$ down to the flux limits of our survey (0.1 mJy). The redshift distribution is similar for the two sub-samples (Figure 3.1). The mean redshift for the MIPS and non-MIPS pairs are 0.88, 0.80 respectively. Figure 3.2 shows a subset of close pairs (both detected and undetected at $24\mu\text{m}$) with MIPS contours. Due to the small separations of close pairs ($20h^{-1}\text{kpc}$ corresponds to $3.6''$ at $z \sim 1$) relative to the beam of the MIPS $24\mu\text{m}$ images (FWHM $\sim 6''$), there are a few instances (5) where only a single $24\mu\text{m}$ detection is found centered between the pair members (see middle left

image in Figure 3.2). In these cases we assume all $24\mu\text{m}$ flux is coming from the primary galaxy.

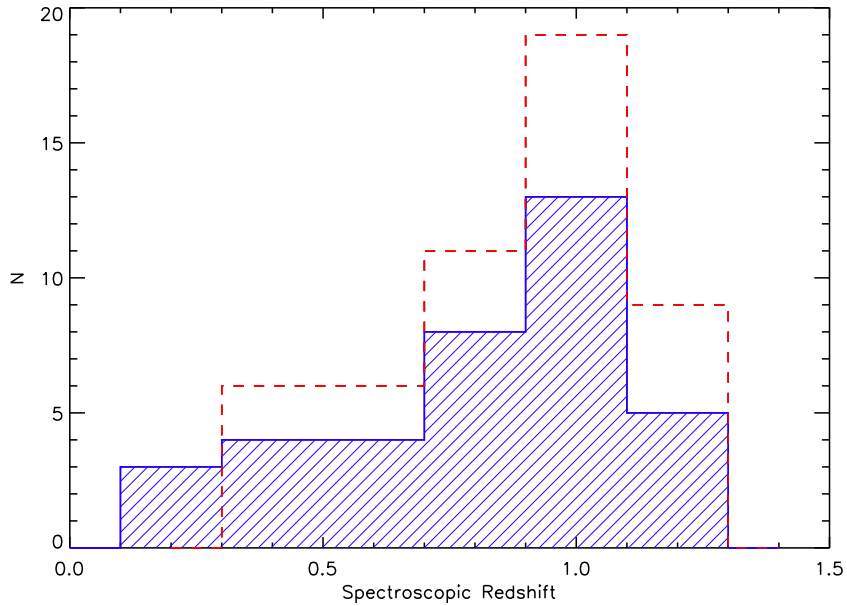


Figure 3.1: The redshift distribution for the MIPS pairs (red) and non-MIPS pairs (blue,hatched) which fulfill the selection criteria outlined in section 3.3.1. This plot shows that the redshift distributions of the two samples are comparable.

3.3.2 Field Correction

Since we have redshift information for only the primary galaxy and not the companions we need to consider what fraction of these close pairs are a result of random projection effects. A field correction was determined using two separate methods to account for these projected close pairs. The first assumed the same optical magnitude and redshift distributions independently for both the detected and undetected $24\mu\text{m}$ samples, while the positions were randomized. The close pair algorithm was applied to 50 realizations of these mock catalogs and the average N_c for each redshift bin was taken to be the pair fraction expected from random. This assumes the absence of clustering.

Before a field correction of this kind can be applied, the density of sources for the two different samples, in our case, MIPS and non-MIPS must be comparable on the scales being probed. For example if MIPS sources preferentially resided in more clustered environments, then the field correction would be underestimated, resulting in an overestimate of the pair fraction. To address this potential bias we probed the environments of $24\mu\text{m}$ detected and undetected objects, finding that on scales of $r_{\text{proj}} > 15h^{-1}\text{kpc}$ the two populations reside in comparable environments. There was a weak indication that MIPS galaxies may live in small

groups at $r_{\text{proj}} < 15h^{-1}\text{kpc}$. Since such groups may, in some cases, be physical associations, we count such cases as separate pairs. However, the number of these cases is small, and does not influence our results in a significant way, supporting the idea that the increase in the pair fraction of the $24\mu\text{m}$ sources is not because they preferentially lie in more clustered regions.

The second method utilizes the I_{AB} magnitude distribution of the full photometric catalog ($\sim 59,000$ sources), and determines the average number of companions, within 1.5 mags (I_{AB}), normalized to the area covered by $5h^{-1}\text{kpc} \leq r_{\text{proj}} \leq 20h^{-1}\text{kpc}$. The results obtained from the two field correction methods agreed within $\sim 2\%$, which is negligible compared to the uncertainty in N_c . The average of the two methods was taken to be the final field correction. Both the pair catalog and randomly generated catalogs were visually inspected for false pairs due to single galaxies being broken up into multiple components in the source extraction phase, or contaminating stars in the photometric catalog, and were removed.

3.3.3 Pair Fractions

The first ever, field-corrected optical pair fractions for the $24\mu\text{m}$ detected and undetected subsamples are presented in Figure 3.3 and Table 3.1. Errors are computed using the jackknife technique (Efron & Tibshirani 1986), e.g. given a sample of N galaxies the variance is given by,

$$\left(\frac{(N-1)}{N} \sum_i [\delta_i^2] \right)^{1/2}. \quad (3.3)$$

The partial standard deviations, δ_i , are computed for each object by taking the difference between N_c , the quantity being measured and the same quantity with the i th galaxy removed, N_{ci} , such that,

$$\delta_i = N_c - N_{ci}. \quad (3.4)$$

To allow a more direct comparison to be made between the generally lower-luminosity low- z pairs, and those at higher redshift, we derived pair fractions for MIPS detected galaxies with an $L_{IR} \geq 5.0 \times 10^{10}$ (approximately the IR luminosity of the famous Antennae Galaxies). In this way we ensure that the sub-luminous galaxies do not strongly influence the pair fractions in the lowest redshift bin. The derived N_c for $24\mu\text{m}$ detected close pairs is $\sim 11\% \pm 8\%$ at $z \sim 0.4$ and increases to $25\% \pm 10\%$ at $z \sim 1$. In contrast, the number of close pairs with no $24\mu\text{m}$ detection show no increase with redshift and have pair fractions consistent with zero at all redshifts ($z < 1.3$). The increasing pair fraction of MIPS bright sources is marginally significant due to the small number of sources in the highest redshift bin, more MIR selected samples between $z = 1-1.5$ are required to strengthen our findings. We would like to be able to rule out the possibility that N_c is biased by the brightest IR sources at $z \geq 1$, since merger fractions

Table 3.1: Close Galaxy Pair Statistics: XFLS

z	N_{gal}	N_c^D	N_c^R	N_c	κ
$24\mu\text{m Detected}$					
0.2-0.5	32	0.188 (6)	0.078 (2.5)	0.110 ± 0.083	0.83
0.5-0.80	82	0.171 (14)	0.057 (4.7)	0.114 ± 0.040	0.93
0.80-1.0	82	0.122 (10)	0.029 (2.4)	0.093 ± 0.038	0.90
1.0-1.3	49	0.429 (21)	0.182 (8.9)	0.247 ± 0.086	0.67
$24\mu\text{m Undetected}$					
0.2-0.5	44	0.136 (6)	0.102 (4.5)	0.034 ± 0.052	1.00
0.5-0.80	76	0.132 (10)	0.134 (10.2)	0 ± 0.039	1.00
0.80-1.0	56	0.214 (12)	0.193 (10.8)	0.021 ± 0.064	0.83
1.0-1.3	55	0.145 (8)	0.180 (9.9)	0 ± 0.065	0.75

Note: N_{gal} is the number of galaxies with a spectroscopic redshift, N_c^D is the number of companions per host fulfilling our pair criteria, while N_c^R is the number of projected companions per host from the field. The corrected fraction of companions per host is given as, $(N_c^D - N_c^R) / N_{gal}$, with errors being determined using a jackknife technique. Numbers appearing in parentheses refers to the number of close pairs in the respective redshift bins. Undetected at $24\mu\text{m}$ refers to sources below the limits of our survey (0.1 mJy). The constant κ is the fractional number of mergers per host galaxy. A $L_{IR} \geq 5.0 \times 10^{10}$ limit was imposed.

change as a function of luminosity and mass (Conselice et al. 2003; Xu et al. 2004). To address this we placed a higher IR luminosity limit ($L_{IR} \geq 7.0 \times 10^{11}$) on the sample, so that at $z \geq 0.7$ the same populations were being probed (optically we are probing $-22 \lesssim M_B \lesssim -19$). We still find an increase in N_c from the lower ($0.8 \leq z \leq 1.0$) to the higher ($z \geq 1$) redshift bins of similar magnitude compared to when the lower IR limit ($L_{IR} \geq 5.0 \times 10^{10}$) was used. Therefore the increase in N_c found at $z \geq 1$ is likely not a result of merely probing brighter IR systems but rather due to a physical increase in the merge rate for the $24\mu\text{m}$ population, however deeper $24\mu\text{m}$ imaging and spectroscopy are required to confirm this. When we consider the averaged pair fraction over $0.2 \leq z \leq 1.3$ for the $24\mu\text{m}$ detected sample we find that galaxies above a flux limit of 0.1 mJy are five times more likely to be in a close galaxy pair, than those below this limit.

3.4 Morphological Mergers: Results

To explore the structural components of galaxies in our sample we used the CAS (Concentration, Asymmetry, Clumpiness) quantitative classification system (Conselice 1997; Conselice et al. 2000; Conselice 2003), and visual classifications.

3.4.1 Visually Classified Mergers

To measure the merger fraction using structural classifications we visually inspected ACS (I_{AB}) images of the full $24\mu\text{m}$ detected spectroscopic catalog with the following groupings:

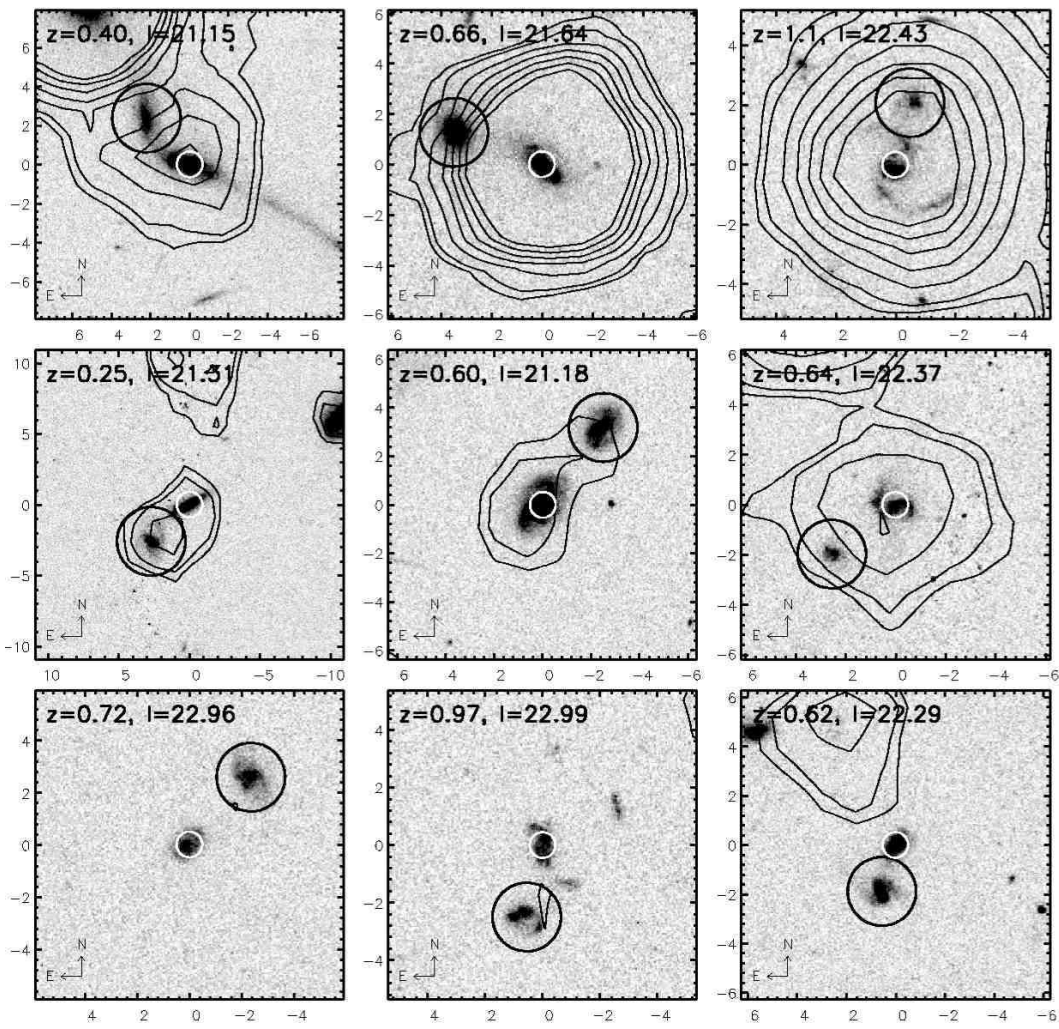


Figure 3.2: A subset of paired galaxies in our sample. Each ACS image is $60h^{-1}\text{kpc}$ on a side with axes in arcseconds, centered on the pair member with the spectroscopic redshift also referred to as the primary or host pair member (white circle), while the companion is highlighted by a black circle. The two upper rows are close pairs which were detected at 24 μm , while the lower set are from the undetected 24 μm paired sample. The 3 – 10 σ 24 μm flux contours are overlaid. The labels are spectroscopic redshift, and I_{AB} magnitude of the primary galaxy.

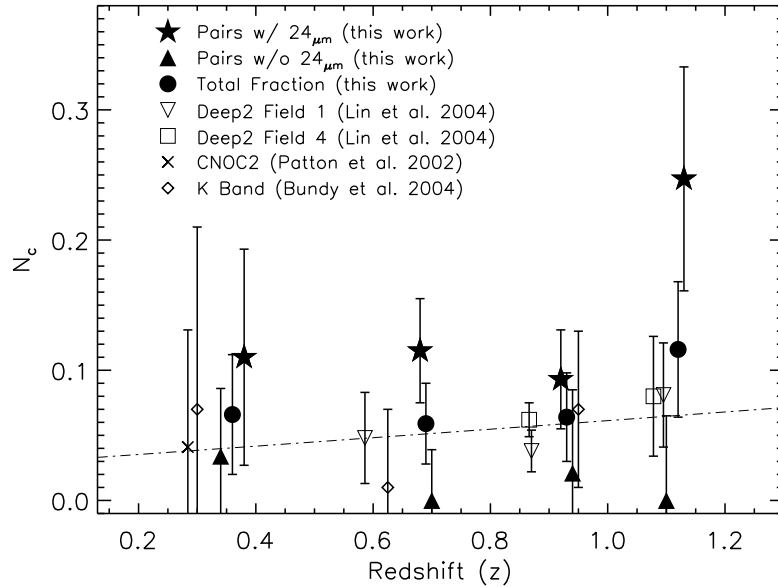


Figure 3.3: The field corrected pair fraction N_c , as a function of redshift as measured in the optical and IR. The stars represent the measurement from our $24\mu\text{m}$ detected sample, triangles depict the field corrected pair fraction of the undetected $24\mu\text{m}$ sub-set, and filled circles show the combined pair fraction of the two samples. Other optically-determined pair fractions appear as open squares (DEEP2 Field 1) and triangles (Field 2)(Lin et al. 2004), and a cross represents CNOC2 (Patton et al. 2002), while the dashed line shows their best power law fit of $(1 + z)^m$ ($m = 1.08 \pm 0.40$). The near-IR pair fraction determined by Bundy et al. (2004) is shown by diamonds. Errors for this work are derived using jackknife statistics, while the IR pair fraction errors implemented counting statistics and DEEP2, CNOC2 errors are determined via bootstrap. A $L_{\text{IR}} \geq 5.0 \times 10^{10}$ limit was imposed on the $24\mu\text{m}$ detected close pairs. Note that each work imposes a slightly different luminosity limit.

early type (E, S0), mid-types (Sa-Sb), late-types (Sc-irr), compact systems, disturbed disks, and mergers. We applied a similar methodology for carrying out this classification as described in detail in (Conselice et al. 2005). Basically, each galaxy was viewed on a computer screen and classified into one of our types by four of the authors, specifically, C. Bridge, C. Conselice, P. Appleton, and S. Laine, with an average agreement within the group of $\sim 85\%$.

Overall we find that $55\% \pm 5\%$ of $24\mu\text{m}$ detected galaxies are disks, which is consistent with Bell et al. (2005); Lotz et al. (2006), while $26\% \pm 5\%$ (86) are merging systems. An additional $\sim 6\%$ were classified as disturbed disks and are therefore possible minor mergers. Examples of visually classified mergers are illustrated in Figure 3.4.

3.4.2 CAS Mergers

Galaxies undergoing a major merger event can also generally be identified by their large asymmetries in the rest frame optical (Conselice et al. 2000, 2003). We defined a major merger as a galaxy having an asymmetry (A) ≥ 0.35 and $I_{AB} \leq 26.5$ (see Figure 3.4 for examples). This limit has been shown to be a clean way to find galaxy mergers, without significant contamination from non-merging galaxies (Conselice 2003).

The merger fraction (f_{gm}) is defined as the number of galaxies undergoing a merger (N_{gm}) divided by the total number of galaxies fulfilling a given set of selection criteria (N_T), such as redshift, stellar mass, or luminosity range,

$$f_{gm} = \frac{N_{gm}}{N_T}. \quad (3.5)$$

Figure 3.5 and Table 3.2 show how the merger fraction for CAS defined mergers evolves as a function of redshift for both $24\mu\text{m}$ detected objects ($L_{IR} \geq 5.0 \times 10^{10}\text{L}_\odot$; top panel) and LIRG/ULIRG galaxies ($L_{IR} \geq 1.0 \times 10^{11}\text{L}_\odot$; bottom panel). As with the $24\mu\text{m}$ detected close pair sample there is an elevated merger fraction compared to other works (Cassata et al. 2005; Lotz et al. 2006) in which no $24\mu\text{m}$ flux limit was imposed, and a slight indication of evolution with redshift, but it is statistically consistent with $m \sim 1.0$ (dashed line), where m is the slope of a power-law of form $(1 + z)^m$.

3.4.3 Morphological Properties of Close Pairs

A CAS analysis was also performed on the close pairs sample which revealed that $24\mu\text{m}$ detected pairs are notably more asymmetric than the undetected-MIPS close pairs (Figure 3.6), suggesting that interactions and collisions play a role in their IR activity. They also generally exhibit morphological features typical of mid-late type galaxies.

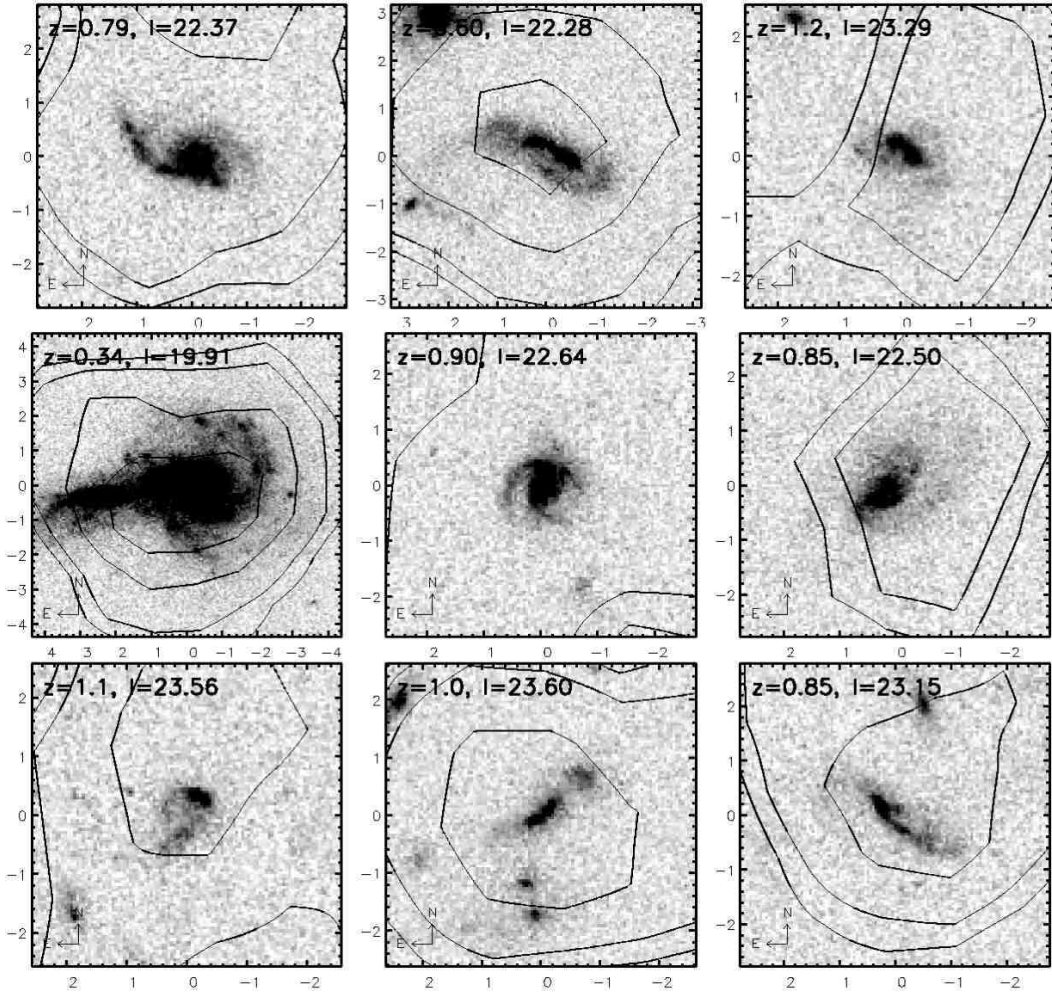


Figure 3.4: A subset of 24 μm detected galaxies in our sample classified morphologically both through visual inspection and by CAS independently as a merger. Each ACS image is $30h^{-1}\text{kpc}$ on a side with axes in arcseconds. The 3 – 10 σ 24 μm flux contours are overlaid. The labels include spectroscopic redshift, and I_{AB} magnitude.

Table 3.2: Morphological Merger Statistics: XFLS

z	24 μm Detected		$L_{IR} > 5.0 \times 10^{10} L_\odot$		N_{gm}^{Vis}	f_{gm}^{Vis}
	N_{gal}	N_{gm}^{CAS}	f_{gm}^{CAS}	N_{gm}^{Vis}		
0.2-0.5	32	1	3.3 ± 5.5	5	15.6 ± 7.0	
0.5-0.80	82	13	15.8 ± 4.4	23	28.1 ± 5.9	
0.80-1.0	82	10	12.2 ± 3.8	30	36.6 ± 6.7	
1.0-1.3	49	10	20.4 ± 6.4	21	42.9 ± 9.4	

Note: N_{gal} is the number of galaxies with a spectroscopic redshift above the IR luminosity cut, N_{gm}^{CAS} is the number of morphological mergers identified via CAS, while N_{gm}^{Vis} is the number of mergers identified through visual classification. The respective merger fractions are noted as f_{gm}^{CAS} and f_{gm}^{Vis} , with poisson errors. A $L_{IR} \geq 5.0 \times 10^{10}$ limit was imposed.

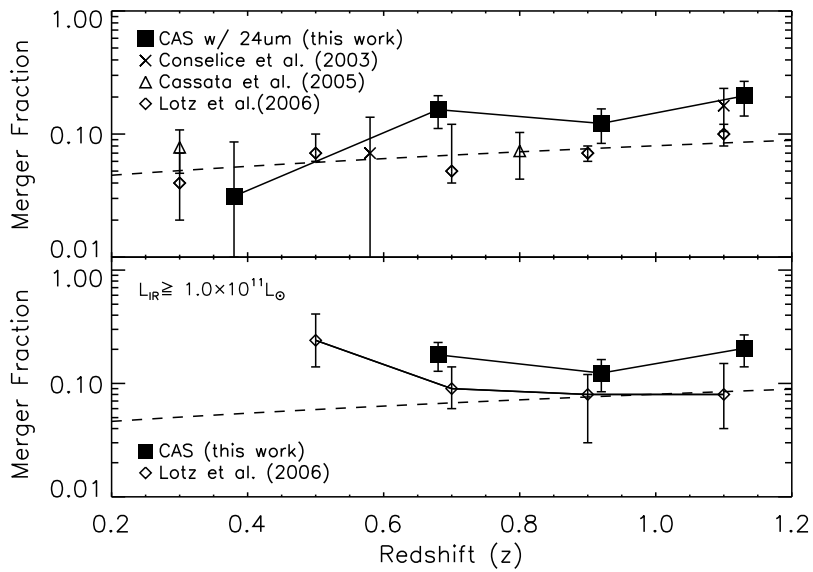


Figure 3.5: The Merger fraction as a function of redshift, using quantitative morphological criteria. The filled squares represent measurements from XFLS (this work) sources with a $24\mu\text{m}$ detection. The “x’s” mark the results of Conselice et al. (2003), triangles depict (Cassata et al. 2005), and diamonds represent Lotz et al. (2006). The top panel shows the merger fraction of other studies with no $24\mu\text{m}$ criteria imposed, while the measurements from this work are mergers with $L_{IR} \geq 5.0 \times 10^{10} L_\odot$. The dashed lines shows the best fit of $(1 + z)^m$ using all points (from the other studies) with no MIPS limit imposed ($m = 1.08$). The bottom panel shows the merger fraction for LIRG/ULIRG galaxies ($L_{IR} \geq 1.0 \times 10^{11} L_\odot$). Error bars were derived using Poisson statistics.

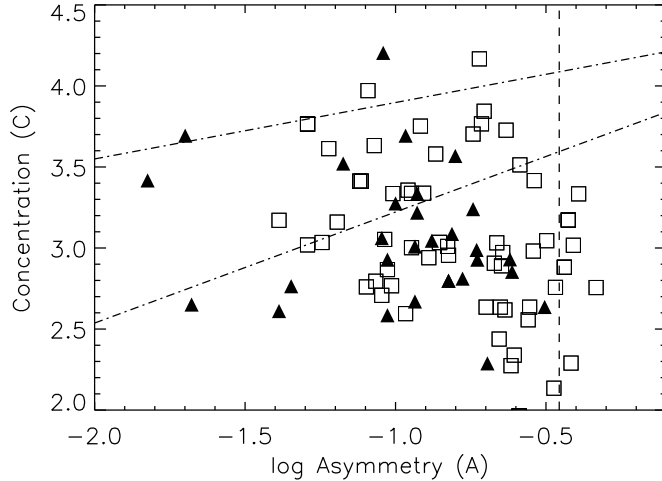


Figure 3.6: Asymmetry - Concentration diagram for the $24\mu\text{m}$ detected close pairs (squares) and undetected pairs (triangles). The long dashed (vertical) line separates merging and non-merging systems ($A \geq 0.35$ is considered a merger), while the dash-dotted lines separate early (upper) to mid to late (lower) type galaxies defined by Conselice (2003). Generally close pairs are mid/late type galaxies, and some would also be morphologically classified as a merger.

If the $24\mu\text{m}$ detected close pairs were generally of a different morphological classification than those pairs undetected at $24\mu\text{m}$ the discrepancy in the asymmetries could be explained. To address this issue each close pair was visually inspected and classified by four of the authors to be either disk or bulge-dominated. We find that 81% of the $24\mu\text{m}$ pairs have disk morphologies while 74% of the undetected $24\mu\text{m}$ hosts were also disk dominated, hence the discrepancy between the asymmetries of the two groups is not caused merely by classification differences, but rather is a physical effect.

3.5 Merger Rates

One of the goals of studying mergers and interactions is to determine how the galaxy merger rate evolves with redshift. The rate at which galaxies merge can affect the mass function of galaxies, and is likely linked at some level to the decline of the cosmic star formation rate. Since we are considering a very broad range in the merger process, from early-stage or pre-mergers selected via close galaxy pairs, to later-stage mergers chosen based on morphological criteria, we must be careful when determining their respective merger rates, as the time-scales for these selection techniques are different.

There are two variations of the merger rate definition. The first is the number of mergers that a galaxy will undergo per unit time (\mathfrak{R}_{mg}), and the second is the fraction of mergers taking

place per unit time per unit co-moving volume (\mathfrak{R}_{mgv}). Since we are primarily interested in mergers which are also Mid-IR bright systems we will have to restrict ourselves to measuring \mathfrak{R}_{mg} because the evolution of the $24\mu\text{m}$ luminosity function with redshift is currently not well constrained, and our redshifts are not complete enough to reconstruct this evolution.

In order to determine \mathfrak{R}_{mg} , we need to identify systems which are destined to merge. We have approached this measurement from three different perspectives, close pairs to select pre-mergers or interactions, visual inspection to select interactions after the first passage, and late stage mergers, as well as CAS criteria which quantitatively selects for later stage mergers. By combining information about the number of ongoing mergers (N_m) and the time-scales, (T_{mg}) on which they will undergo a merger, one can estimate an overall merger rate, $\mathfrak{R}_{mg} = N_m/T_{mg}$. Each method of identifying mergers is capturing a different snapshot of the merger process, each with different merger time scales.

The value of N_c is directly proportional to the number of mergers per galaxy (N_m), such that $N_m = \kappa N_c$ (κ is a constant relating to the number of mergers per galaxy). Hence, the merger rate determined using close galaxy pairs is given by, $\mathfrak{R}_{mg} = \kappa N_c/T_{mg}$. The value of κ depends on the nature of the merging systems under consideration. If one were to identify a pure set of galaxy pairs each consisting of one companion undergoing a merger, then $\kappa = 1.0$. In our case it exclusively accounts for close pairs which are in doubles and perhaps higher order N-tuples. Our definition of κ differs by a factor two from Patton et al. (2000) which in this instance would have $\kappa = 0.5$ since they have redshifts for both pair members and one merger is made up of two companions. We have redshift information for only one pair member, therefore one merger is made up of a primary and one companion. The merger rate equation for galaxies selected by visual classification and CAS parameters is simply $\mathfrak{R}_{mg} = f_{gm}/T_{mg}$, where f_{gm} is the galaxy merger fraction.

3.5.1 Merger Time-scales

Before the merger fraction can be used to calculate the merger rate we need to understand the time-scale in which a merger occurs. Each technique of identifying mergers has a different time-scale since each is sensitive to a different interval of the merger process. There are two main methods that have been used to estimate the time-scale of a merger: dynamical friction arguments, and N-body models.

To compute the time needed for two galaxies in a close pair to merge due to dynamical friction we must first assume that the mass distribution within a galaxy falls off as r^{-2} , that it has an isothermal profile, and that the merging galaxies have circular orbits. The dynamical friction time-scale, t_{fric} (following Binney & Tremaine (1987)) expressed in Gyrs, can be written as,

$$t_{fric} = \frac{2.64 \times 10^5 r^2 v_c}{(\ln \Lambda) M}, \quad (3.6)$$

where, M is the mass (M_\odot), v_c is the circular velocity, and r is the projected pair separation of $20h^{-1}\text{kpc}$, while $\ln \Lambda$ is the Coulomb logarithm. The velocity (v_c) and stellar mass (M) values were taken to be 250km/s , and $3.0 \times 10^{10} M_\odot$ as determined in Patton et al. (2002); Conselice (2006b). Simulations find that a $\ln \Lambda \sim 2$ value fits the orbital decay for equal mass mergers (Dubinski et al. 1999).

Ultimately, this is only an estimate for the merger time-scale of close pairs and can range from $\sim 0.5\text{-}1.0\text{Gyrs}$ (Conselice 2006a). We take the average merger time-scale for a set of close companions with $r_{proj} \sim 20h^{-1}\text{kpc}$, of roughly equal mass to merge in $\sim 0.5\text{ Gyrs} \pm 0.25$. (Patton et al. 2000; Conselice 2006b).

Conselice (2006a) showed through N-body simulations that visual classification selects on-going mergers over a longer time-scale ($1.0\text{ Gyrs} \pm 0.25$) since the human eye detects both early (after first encounter) and later stage mergers, while the asymmetry of a galaxy is sensitive to $0.41\text{ Gyrs} \pm 0.17$ (Conselice 2006a) of the merger sequence. With reasonable estimates of the merger time-scales we can now proceed to derive the galaxy merger rate.

3.6 The Evolution of the Galaxy Merger Rate $0.2 < z < 1.3$

3.6.1 Fitting the Merger Rate Evolution

A primary, yet difficult goal of close pair and merger studies is to probe how the rate galaxies merge evolves with redshift. Traditionally, the evolution of the pair fraction, merger fraction and in turn the merger rate have been fit by a power-law of the form $f = f_o(1 + z)^m$, where f_o is the present day ($z=0$) close pair or merger fraction, and m is the power-law index. Fitting the close pair and merger fractions with a power-law is motivated by the theory of structure formation. The rate galaxies merge is intimately connected to the dark halo merger history and can be understood based on the Press-Schechter (P-S) formalism (Press & Schechter 1974). P-S describe how the density of dark matter halos evolve as a function of redshift for a given halo mass. N-body models of hierarchical galaxy formation are in good agreement with P-S formalism, and its modified forms (e.g. Gottlöber et al. 2001; Khochfar & Burkert 2001). Simulations find that the fraction of merging galaxies can be well fit to the $(1 + z)^m$ formalism up to $z \sim 2$.

Toomre (1977a) were the first to suggest that the merger rate may be larger at higher redshifts, by using estimates of past merger remnants. Within the past two decades numerous studies have been performed to better estimate the evolution of the galaxy merger fraction, us-

Table 3.3: Summary of Merger Rate Studies

Reference	Type	Redshift Range	# of CP or M	$(1 + z)^m$	Criteria
Zepf & Koo (1989)	CP	$< z >= 0.25$	20	4.0 ± 2.5	$B < 22, \theta \leq 4.5''$
Carlberg et al. (1994)	CP	$< z >= 0.42$	14	3.4 ± 1.0	$V \leq 22.5, r_p \leq 20 h^{-1} \text{kpc}$
Burkey et al. (1994)	CP	0.1-0.7	50	2.5 ± 0.5	$18 < I < 22$
Woods et al. (1995)	CP	...	23	0	$I \leq 24$
Yee & Ellingson (1995)	CP	0.2-0.5	25	4.0 ± 1.5	$r \leq 21.5$
Infante et al. (1996)	AC	$< z > \sim 0.35$...	2.2 ± 0.5	$R = 19-21.5$
Neuschaefer et al. (1997)	CP	$z = 1 - 2$	90	1.2 ± 0.4	$I \leq 25$
Patton et al. (1997)	CP	$z \leq 0.45$	73	2.9 ± 0.9	$r \leq 22$
Carlberg et al. (2000)	CP	0.1-1.1	109	0.1 ± 1.4	$M_R \geq -19.8 + 5 \log(h)$
Le Fèvre et al. (2000)	CP,M	0-1.2	26,49	$2.7 \pm 0.6, 3.4 \pm 0.6$	$\Delta m \leq 1.5 \text{ mags}$
Patton et al. (2000)	CP	$z=0.015$	80	$2.26\% \pm 0.52$	$-21 \leq M_B \leq -18, f_o \text{ quoted}$
Gottlöber et al. (2001)	S	$z < 2$...	3.0	N-body Sims.
Patton et al. (2002)	CP	0.12-0.55	88	2.3 ± 0.7	$R_c \leq 21.5$
Conselice et al. (2003)	M	0-3	43	4-6	$M_B \leq -18, M > 10^{10} M_\odot$
Bundy et al. (2004)	CP	0.2-1.5	7	~ 0	$K_{AB} < 21.0$
Lavery et al. (2004)	CR	0.1-1.0	25	5.2 ± 0.7	
Lin et al. (2004)	CP	0.45-1.2	...	1.08 ± 0.4	$-21 \leq M_B \leq -19, r_p \leq 30 h^{-1} \text{kpc}$
Berrier et al. (2006)	S	$z < 2$...	~ 1	N-body Sims.
Lotz et al. (2006)	M	0.2 – 1.2	157	$\lesssim 1$	$L_{IR} \leq 10^{11} L_\odot$
Kartaltepe et al. (2007)	CP	0-1.2	1749	3.1 ± 0.1	Photometric redshifts
Bridge et al. (2007a)	CP	0.2-1.3	87	~ 1	includes MIPS and Non-MIPS
Bridge et al. (2007a)	CP	0.2-1.3	$51,24 \mu\text{m}$	2.12 ± 0.93	$L_{IR} \leq 10^{11} L_\odot$
Bridge 2007 in prep.	M	0.1-1.15	1240	2.24 ± 0.24	$M > 10^{9.5} M_\odot, i' < 21.9$

Note: The type of study reflects the technique used to probe merger statistics. CP - Close Pairs, AC - Angular Correlation function, M - Morphological, S - Simulation. The fourth column denotes the number of close pairs or morphological mergers used in the respective analyzes.

ing both the close pair technique (Zepf & Koo 1989; Burkey et al. 1994; Carlberg et al. 1994; Yee & Ellingson 1995; Woods et al. 1995; Patton et al. 1997, 2000, 2002; Le Fèvre et al. 2000; Lin et al. 2004; Bundy et al. 2004) and morphological parameters (Le Fèvre et al. 2000; Conselice et al. 2003; Lavery et al. 2004; Lotz et al. 2006). Observational fits to the power-law of form $(1 + z)^m$ have yielded a wide range of results, spanning $0 \leq m \leq 5$, (up to $z \sim 1$) with typical errors $\gtrsim 30\%$ (see Table 3.3 for a summary of the literature). The large spread in values is in part due to the different selection criteria used to identify merging systems and biases from optical contamination or redshift completeness. Patton et al. (1997) considered these biases and demonstrated that most results to that date were consistent with their estimate of $m = 2.9 \pm 0.9$. Recently, optical and near-IR close pair studies (Lin et al. 2004; Bundy et al. 2004) have derived merger fractions with little redshift evolution ($m \sim 1$), as have some morphological studies using (G), and M_{20} (Lotz et al. 2006).

3.6.2 XFLS Merger Rate

When we consider all the close pairs identified in our sample, both those detected at $24 \mu\text{m}$ and not, we find a merger fraction and rate consistent with recent studies showing little redshift

evolution ($m \sim 1$). However, when we separate the pair sample into systems with a $24\mu\text{m}$ detection above 0.1 mJy, and those below it, we do see a stronger evolution of N_c with redshift, (recall that $N_c \propto \mathfrak{R}_{mg}$) and therefore also in the merger rate (Figure 3.7).

Similarly, MIPS galaxies visually classified as mergers and those identified via asymmetry levels ($A \geq 0.35$) using the CAS parameters, also show redshift evolution in the merger fraction and rate. The merger and close pair fraction computed using the different methods are in good agreement when normalized by their respective time-scales (Figure 3.7), reinforcing the idea that we are probing different phases of the same physical process - the merger process.

Considering all three merger selection techniques for MIPS sources, we find the best fit of the merger rate parameterized by $\mathfrak{R}(0)(1+z)^m$ to be $\mathfrak{R}(0) = 0.077 \pm 0.045$, and $m = 2.12 \pm 0.93$.

3.6.3 Mid-IR Merger Rate: Implications

This result suggests that when one considers a sample of close galaxy pairs solely on their optical fluxes, brighter than $M_B \sim -19$, little evolution of the merger rate with redshift is found. However, close pairs emitting $24\mu\text{m}$ flux, a tracer of star formation, exhibit an increase in the merger rate with redshift. The infrared luminosity limit ($L_{IR} \geq 10^{11} L_\odot$) imposed on the close pairs and mergers allows us to primarily probe systems in a LIRG/ULIRG phase at $z \geq 0.4$ (see Figure 3.10 for details of the L_{IR} distribution). The increase of the merger fraction and rate of this population of galaxies coupled with the fact that LIRG/ULIRG galaxies dominate the SFR density at $z \geq 0.7$ (Le Floc'h et al. 2005) suggests that merging does in fact play an increasingly important role in star formation out to $z \sim 1$, with a trend to even higher significance at $z > 1$.

As the Mid-IR is a good proxy for star formation, unaffected by dust, we now proceed with quantifying the contribution mergers make to the global SFR. The next section presents our investigation of the IR luminosities and Mid-IR SFR's of interacting systems.

3.7 Total Infrared Luminosities of Mergers

3.7.1 Estimating the IR Luminosity of Galaxies from Their Mid-IR Emission

One way to quantify the role merging galaxies play in triggering star formation is to investigate their contribution to the IR luminosity density. The L_{IR} of a galaxy is a combined measure of the reprocessed UV photons intercepted by dust from massive young stars and AGN.

Local IR luminous galaxies show a correlation between their rest $12\text{-}15\mu\text{m}$ luminosity and their total integrated IR luminosity ($8\text{-}1000\mu\text{m}$), see Figure 3.8 (Spinoglio et al. 1995; Chary & Elbaz 2001; Elbaz et al. 2002). By using this tight correlation and considering the general IR/submillimeter colour and/or luminosity-colour correlations of local IR-luminous galaxies,

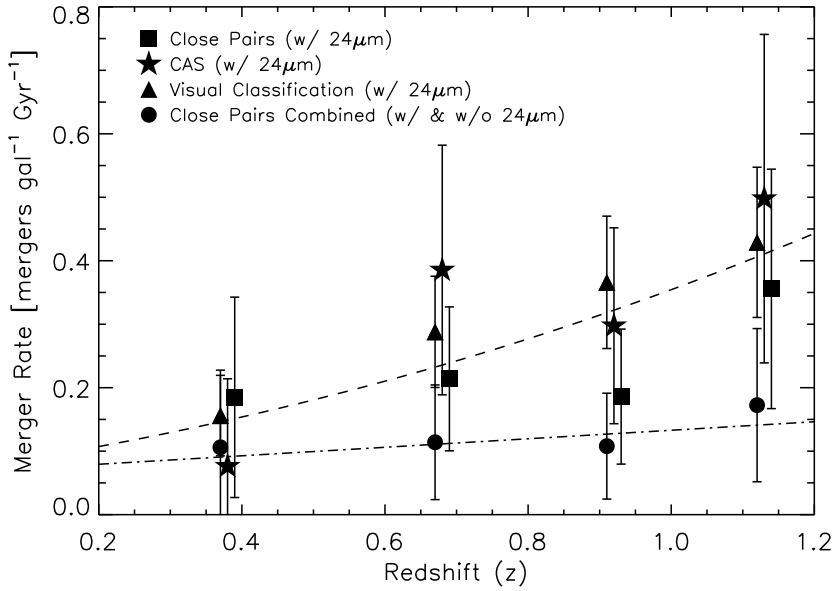


Figure 3.7: The number of mergers per galaxy per Gyr ($L_{IR} \geq 5 \times 10^{10}$) as a function of redshift. Three merger/interaction selection techniques are applied, close pairs (squares), CAS criteria (stars), and visual classification (triangles), while merger rates for the combined (w/ and w/o $24\mu\text{m}$ detections) using the close pairs method are shown with circles. The long dashed curve is the best fit of the form $(1 + z)^m$, using the FLS data for the three techniques; the dot-dashed curve represents the best fit for the combined total close pairs (MIPS and non-MIPS pairs).

several galaxy template libraries have been built, which can be utilized to estimate the total IR luminosity of galaxies based on their $24\mu\text{m}$ flux densities (Dale et al. 2001; Chary & Elbaz 2001; Lagache et al. 2003).

Infrared luminosities (8-1000 μm) were calculated utilizing the $24\mu\text{m}$ flux densities and two different SED template suites: Chary & Elbaz (2001) and Dale et al. (2001), for the full MIPS $24\mu\text{m}$ spectroscopic sample (Figure 3.10). The redshift dependent correlations between the observed $24\mu\text{m}$ flux density and the L_{IR} were computed. An estimate of the total IR luminosity was derived using both the Chary & Elbaz (2001) and Dale et al. (2001) set of templates separately. The final L_{IR} was taken to be the average L_{IR} derived from the two different SED libraries. The uncertainty in the total IR luminosity is the systematic error, derived from the absolute difference of the two L_{IR} , and summed in quadrature with the statistical error. The total IR luminosities are accurate within a factor of ~ 2 - 3 up to $z \sim 1$ (Le Floc'h et al. 2005), which is adequate for our purposes.

The verification region in which this work focuses on has the sensitivity to probe IR luminous galaxies out to redshift ~ 2.5 , more specifically, our spectroscopic range (out to $z \sim 1$) probes the full range of the LIRG population (see Figure 3.9).

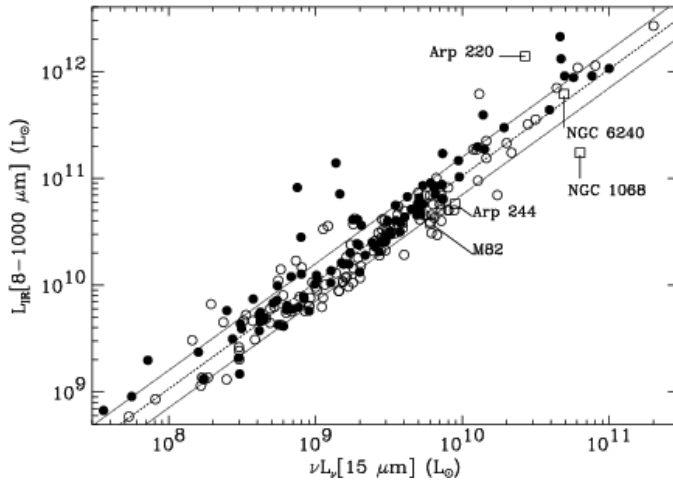


Figure 3.8: IR luminosity correlations for local galaxies from Elbaz et al. (2002). The plot shows the $L_{IR}[8-1000\mu m]$ versus IRSOCAM-LW3 ($15\mu m$) luminosity for 120 galaxies. Five specific galaxies are highlighted, 3 starburst (M82, Arp 244, Arp220), and 2 Seyfert 2's (NGC 1068, NGC 6240). The tight correlation between the rest $15\mu m$ luminosity and the total integrated IR luminosity of local galaxies is taken advantage of to derive total IR luminosities for higher redshift galaxies using the observed $24\mu m$ flux.

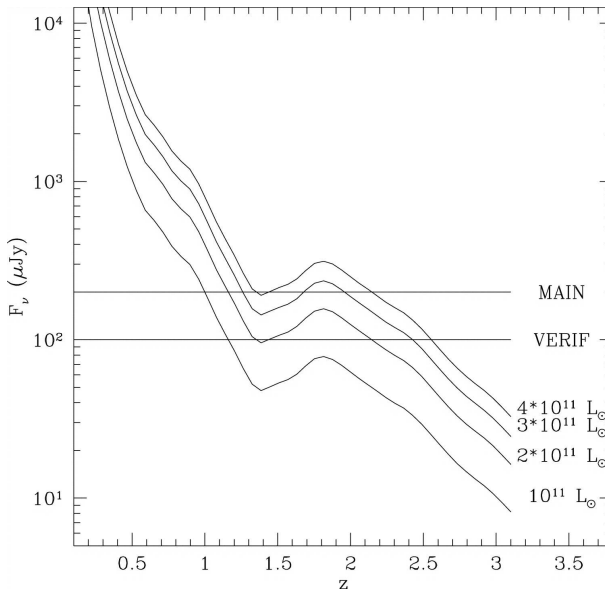


Figure 3.9: The $24\mu m$ flux of a typical luminous IR galaxy (SED of M82) with different luminosities as a function of redshift taken from Fadda et al. (2006). The solid horizontal line depicts the sensitivity levels of both the main, and verification region. LIRGs are easily detected in the XFLS-verification region out to $z \sim 1$.

3.7.2 Caveats in Deriving LIR

The derivation of the total IR luminosity ($8 - 1000\mu\text{m}$) relies on a few assumptions and caveats that are worth noting. First, the suite of SEDs used to estimate the L_{IR} are derived from properties of galaxies in the local universe. One may question the accuracy of these templates with respect to higher redshift sources. Much work has been done to address this concern. The evidence currently available suggests that IR SEDs at $z \gtrsim 0.7$ seem to be adequately represented by the IR SEDs of local galaxies. The well known local Far-IR/radio correlation results in a MIR/FIR and in turn a MIR/radio correlation (Condon 1992; Chary & Elbaz 2001). This correlation appears to still be valid at higher redshifts (Elbaz et al. 2002; Appleton et al. 2004) implying that galaxies observed at large look-back times share many of the same properties as fully formed mature galaxies seen locally.

Additionally, the $15-24\mu\text{m}$ flux ratios from *ISO* and *Spitzer* for $z \sim 1$ galaxies is similar to that for local starburst dominated galaxies. This evidence provides reasonable confidence in using local galaxy templates to estimate the IR luminosity of higher redshift sources. However, this issue will be clarified by work currently underway with *Spitzer* and in the future with *Herschel*.

A second caveat related to the IR luminosity estimates comes from the fact that the template libraries are only representative of normal and starburst-like galaxies, and do not include SEDs typical of AGN. The consequences of this can result in an over-estimate of the L_{IR} in AGN dominated systems, as the power law continuum can mimic the SED of a high luminosity IR galaxy.

Lastly, for higher redshift galaxies MIPS $24\mu\text{m}$ begins to probe a spectral region of prominent broadband features called polycyclic aromatic hydrocarbons or PAH's. These features are observed between rest 3 and $14\mu\text{m}$ and result in striking global SED signatures when integrated over normal spiral galaxies. However, the strength and presence of PAH features can change. Low metallicity galaxies and those harboring an AGN tend to have little or no PAH signatures , while star forming systems can exhibit a range of feature strengths. Overall, the $24\mu\text{m}$ flux density of an object with a known redshift can provide a reasonable estimate of the IR luminosity for most galaxies. More accurate measurements of L_{IR} will be made possible with *Herschel* which better probes the thermal dust peak.

3.7.3 The Total IR Luminosity of MIPS sources in the XFLS

The infrared luminosities ($8-1000\mu\text{m}$) for all MIPS detected galaxies in our sample were estimated using the procedure outlined in section 3.7.1. The IR luminosities are displayed as a function of redshift in Figure 3.14 and show the strong luminosity evolution of Mid-IR galax-

ies. The derived IR luminosities are accurate to within a factor of $\sim 2\text{-}3$ up to $z \sim 1$. We see that below $z \sim 0.5$ most sources are only moderate IR emitters ($L_{IR} < 10^{11} L_\odot$), with only a small number of LIRGs and no ULIRGs ($L_{IR} > 10^{12} L_\odot$). The lack of ULIRGs below $z=0.5$ is simply a matter of volume and their rarity in the local universe. Our survey is probing $\sim 8.2 \times 10^4 \text{Mpc}^3$, at $z=0.5$, and number density predictions expect <1 ULIRG in that volume (Wang 2006). At $z=1$ however we are probing larger volumes detecting 7 ULIRGs, again consistent with number density models which predict ~ 6 ULIRGs (Wang 2006).

3.7.4 IR Luminosity of Close Pairs and Mergers

As mentioned earlier, the role merging galaxies play in triggering star formation can be studied through their contribution to the IR luminosity density, since the L_{IR} of a galaxy is a good tracer of star formation that is unaffected by dust extinction.

The IR luminosities of galaxies identified in close pairs and those found to be undergoing a merger have been plotted in Figure 3.10. We find that galaxies involved in the merger process (close pairs or later stage mergers) share a similar luminosity distribution to $24\mu\text{m}$ bright isolated undisturbed field galaxies. This suggests that although some of these systems are likely to have recently undergone a starburst due to tidal interactions, their IR luminosities have not been substantially elevated compared to that of isolated, undisturbed IR-luminous galaxies. That being said, the fact these galaxies are in close pairs or mergers may have resulted in them being classified as IR-bright in the first place. Overall, it is clear that LIRG phase galaxies can be in close pairs, mergers, or isolated undisturbed galaxies, all with similar IR luminosities. LIRG mergers and pairs are not the brightest objects in this IR phase of galaxy evolution, but rather have average IR luminosities. Although, as mentioned earlier, red-AGN seem generally more luminous which is in part due to template mismatches (Chary & Elbaz 2001).

3.7.5 AGN Contamination

The utilization of the L_{IR} luminosity as a star formation tracer hinges on the assumption that the dominant heat and ionizing source is radiation from young massive stars and not AGN. Therefore to investigate the contribution an interacting or merging galaxy makes towards the total L_{IR} density from star formation alone, we must first attempt to remove AGN from our sample.

3.7.6 AGN Identification: IRAC Colours

It has been shown with *Spitzer* and *ISO* that AGN can be identified in the MIR by their strong continuum. The main contributors to the MIR continuum ($3\text{-}12\mu\text{m}$) of galaxies are polycyclic

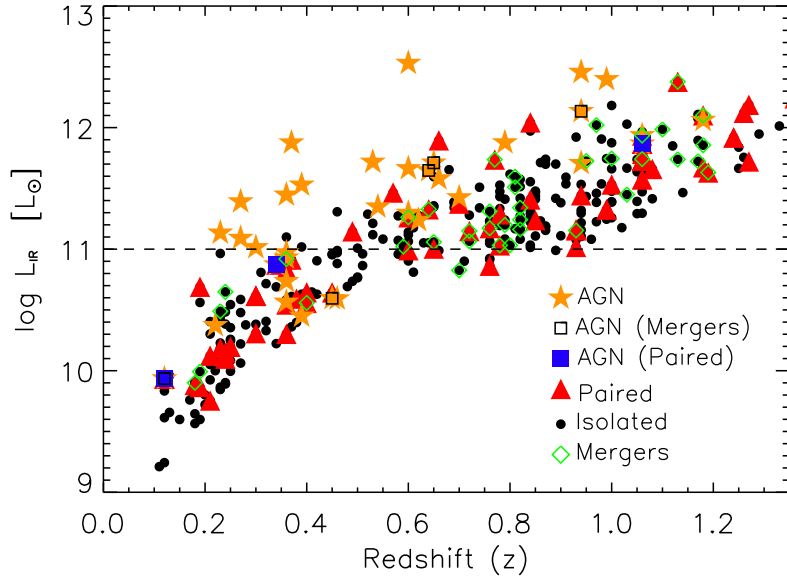


Figure 3.10: Infrared luminosity $L_{IR[8-1000\mu m]}$ vs. redshift for the MIPS 24 μm sample with spectroscopic redshifts, broken down into galaxies in a close pair (red triangle), CAS mergers (open green diamonds), AGN candidates (yellow star), AGN candidates in a close pair (blue square), AGN mergers (open black square), and field galaxies (black circles). LIRGs lie above the horizontal dashed line at $L_{IR} \geq 10^{11} L_{\odot}$.

aromatic hydrocarbons (PAH) emission features (Puget et al. 1985), light from old stellar populations (Boselli et al. 2003), emission from very small gains in HII regions (Desert et al. 1990), and power-law continuum from AGN (Clavel et al. 2000).

Numerous studies have taken advantage of the SED signatures that arise from the above processes to discriminate between star forming galaxies and those dominated by the strong MIR continuum flux of an AGN (Laurent et al. 2000; Lacy et al. 2004; Stern et al. 2005). The four channel *Spitzer* IRAC photometry (3.6, 4.5, 5.8 and 8.0 μm) was used by Lacy et al. (2004) to identify a region in colour-colour space where AGN dominated sources tend to reside. However, it must be noted that not all galaxies that fall into this region of IRAC colour space will be AGN. This region selects AGN candidates, whose SEDs are consistent with AGN activity, and hence can not be photometrically ruled out. Choi et al. (2006) found that 63% of their AGN candidates selected by their IRAC colours exhibited some AGN signature in their optical spectra, however obscured AGN are difficult to positively identify in optical spectra and the remaining 37% could not be ruled out. More recently, Lacy et al. (2007) followed up a sample of bright MIPS galaxies identified as AGN candidates, by their IRAC colours with optical spectroscopy. They found that 92% of the AGN candidates did show spectral AGN signatures. In figure 3.11 we reproduce the IRAC colour-colour plot from (Lacy et al. 2004) for the entire XFLS main

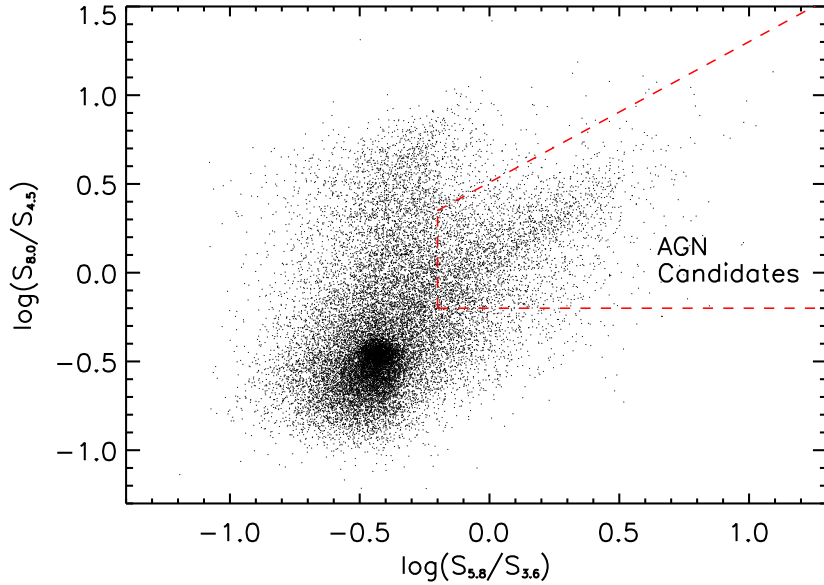


Figure 3.11: IRAC four-channel colour-colour plot used to identify candidate AGN. The region outlined in red (dashed lines) illustrates the area in the colour-colour plot where AGN are expected to reside (Lacy et al. 2004; Sajina et al. 2005; Lacy et al. 2007). Sources detected in all four IRAC channels from the full 4 deg^2 XFLS main field are plotted ($\sim 20,000$ sources).

survey area. The dashed line defines the region expected to be occupied by AGN.

Due to the nonuniform rest-frame spectral coverage of our sample we rely on the four-band IRAC colour selection technique used by Lacy et al. (2004) to identify and remove AGN candidates (Figure 3.12). Over the modest redshift range of our sample, this method is still effective at separating IR-warm AGN from starburst systems. We find an AGN contamination rate of $\sim 12\%$ for the full $24\mu\text{m}$ sample, which is consistent with that found by (Choi et al. 2006; Lacy et al. 2007). Similarly, we find that $\sim 14\%$ of the hosts in a pair or merger were characterized as AGN, consistent with that found in the field.

Locally, AGN dominate the MIR output of only the most extreme ULIRGs, while the general IR population is dominated by star formation at the $\sim 85\text{-}90\%$ level. At higher redshifts, models predict that emission arising from pure AGN in $24\mu\text{m}$ sources should be negligible (Lacy et al. 2007). It should therefore be reasonable to assume that AGN will not be the dominate heat source producing the MIR flux, however to be conservative we will remove galaxies that have been identified as AGN candidates from our sample. This allows us to exclusively probe the star forming properties of these systems (a lower limit) by way of their MIR luminosities.

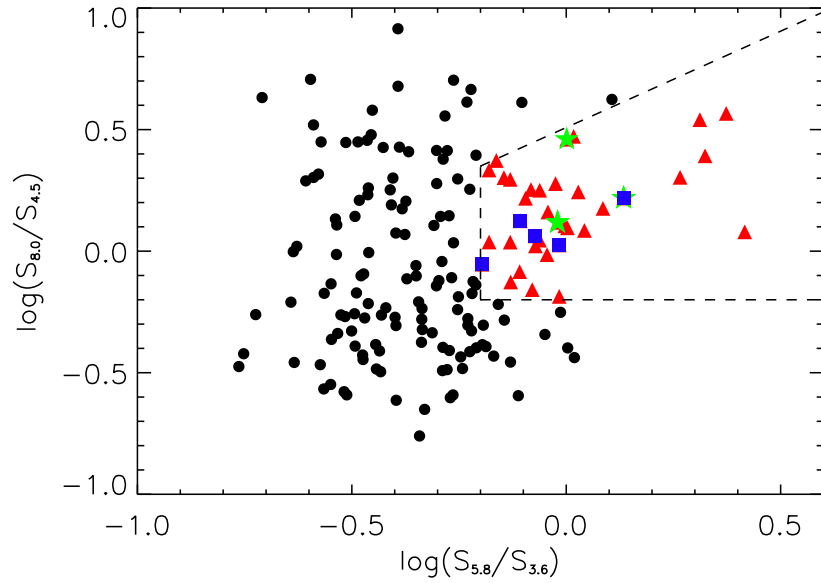


Figure 3.12: IRAC colour-colour plot using the region in the XFLS covered by the ACS imaging. Circles represent objects with spectroscopic redshifts and detections in all four IRAC channels. The red triangles indicate objects which have met the colour criteria (shown by the dashed line) of an AGN candidate (Lacy et al. 2004). The green stars and blue squares depict objects in a close galaxy pair or merger whose host was also flagged as an AGN candidate.

3.7.7 The Contribution of Close Pairs and Mergers to the IR Luminosity Density

With AGN candidate objects removed we can infer the contribution to the L_{IR} density from star formation coming from $24\mu\text{m}$ galaxies in an interaction or merger as a function of redshift. We derive the number of statistically "real" galaxy pairs from our pair fraction result at each redshift interval and determine the total L_{IR} density from close pairs which is in turn divided by the L_{IR} density from the whole sample. We find that paired galaxies ($L_{IR} \geq 10^{11} L_\odot$) are responsible for $27\%^{+9\%}_{-8\%}$ of the IR background stemming from star formation at $z \sim 1$. Since we only know the redshift of the host galaxy we select "real" close pairs in a statistical sense, and derive error bars for the close pairs contribution by the spread of 50 realizations of the L_{IR} density from different combinations of $24\mu\text{m}$ galaxy pairs. We also applied this analysis to CAS and visually classified mergers, which make up an additional $\sim 12\%$, and $\sim 22\%$ of the IR luminosity density respectively. Naturally, there is some overlap in mergers identified through close pair criteria and morphological parameters, since interacting pairs can exhibit tidal tails and asymmetric structures, causing them to also be identified morphologically as mergers. We found that 37% of CAS defined mergers were also in a close pair, and 31% of visually identified mergers were also classified by CAS as merging. In cases where a merging

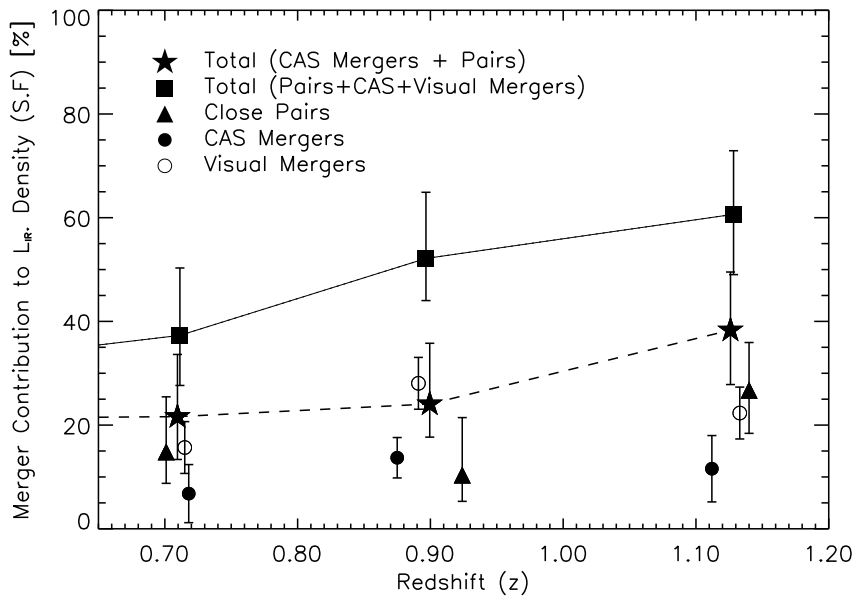


Figure 3.13: The fraction of the total L_{IR} density (as a result of star formation) as a function of redshift coming from LIRG/ULIRG galaxies in a close pair (pre-merger phase) shown by triangles, or more advanced stage mergers defined morphologically (circles). The star symbol indicates the total combined contribution from close pairs and CAS mergers, while squares depict the total from close pairs, CAS, and visually classified mergers. Note an infrared limit of $L_{IR} \geq 10^{11} L_\odot$ was imposed.

system was identified using multiple techniques it's contribution was only counted once. For example, if a merger identified morphologically (either through CAS or visual inspection) is also in a close pair it is removed from the morphological merger catalog, or if a CAS merger is also identified visually the merger is removed from the visual merger catalog. This insures that no close pair or merger is counted more than once when deriving the contribution from interactions and mergers to the IR luminosity density.

The combination of these three merger selection techniques identifies a large range in the merger process, from pre-merger to late stage mergers, implying that $\sim 40\text{-}60\%$ of the infrared luminosity density at $z\sim 1$ can be attributed to galaxies involved in some stage of a major merger (Figure 3.13). The remaining $\sim 40\%$ of the IR background from LIRGs is likely to predominately come from active, isolated gas-rich star-forming spirals, with some contribution from minor mergers.

If we exclude visually classified mergers, as they are somewhat subjective in nature, the close pair/merger contribution to the IR density is $\sim 38\%$, in good agreement with Lin et al. (2006) who estimate a moderate contribution from interacting and merging systems of $\lesssim 36\%$. It must be noted however that neither Lin et al. (2006) or this work have considered the contri-

bution from minor mergers and therefore represent lower limits of the merger contribution to the IR background. In addition, mergers flagged as potential AGN were also not included, and these systems will also house some star formation.

3.8 Star Formation in Mergers & Interactions

An important and highly debated question is: how important are galaxy mergers in understanding the dramatic decline of the cosmic SFR density from $z \sim 1$ to the present day? It has been well established that mergers and interactions can induce violent bursts of star formation (Schweizer 1982; Mihos & Hernquist 1996; Barton et al. 2000; Cox et al. 2006).

In this section, we explore the amount of star formation being contributed by galaxies involved in an interaction or merger at $z \sim 1$, when the Universe was only half its present age.

To investigate this contribution we derived the SFR for our $24\mu\text{m}$ detected close pairs and mergers, using their total IR luminosities (L_{IR}).

3.8.1 IR Star Formation Rate Calculations

The infrared luminosity of a galaxy is a star formation rate tracer which is unaffected by the extinction of dust. In general, the dust is heated primarily by stellar radiation from young stars, AGN, and an older evolved stellar population. The dominant heat sources of most dusty, high-opacity systems such as LIRGs and starbursts is stellar radiation from young stars. In these types of systems the L_{IR} can be converted into a SFR using the calibration of Kennicutt (1998),

$$SFR_{IR} = 4.5 \times 10^{-44} L_{IR} (\text{ergs s}^{-1}), \quad (3.7)$$

where L_{IR} is the integrated luminosity from 8-1000 μm as determined in section 3.7.1. Equation 3.7 assumes a Salpeter IMF (0.1-100 M_\odot), solar abundance, and continuous bursts lasting 10-100 Myrs.

3.8.2 Close Pair and Merger Contribution to the SFR Density

We estimated the contribution mergers and interactions with $L_{IR} \geq 10^{11} L_\odot$ make to the SFR density at $z \sim 1$ in two ways. The first is simply to consider their contribution to the L_{IR} density which is a star formation tracer. In section 3.7.7 we determined that mergers and interactions at $z \sim 1$ (above $L_{IR} \geq 10^{11} L_\odot$) are responsible for 40-60% of the IR luminosity density. Using the results of Le Floc'h et al. (2005) which showed that $z \geq 0.7$ LIRGs produce $\sim 70\%$ of the star formation rate density, we can infer that mergers and interactions in LIRG/ULIRG

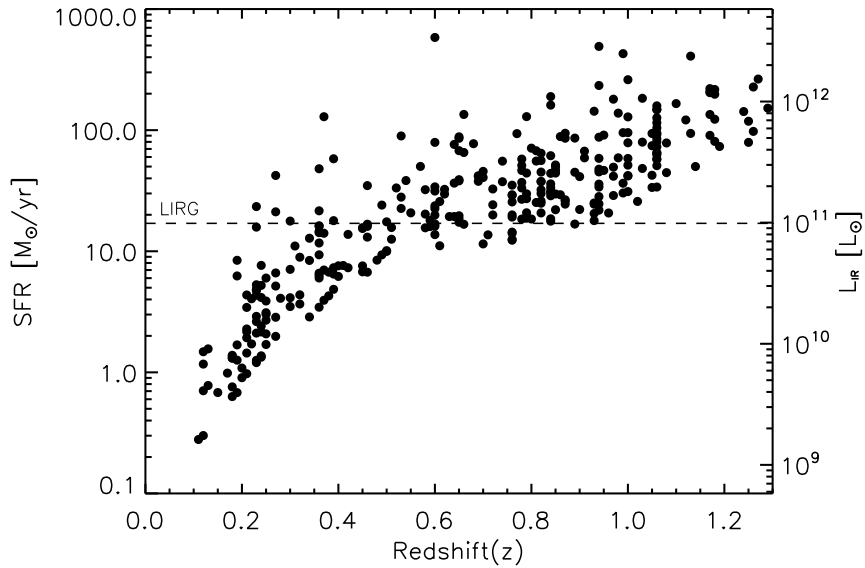


Figure 3.14: Total Infrared luminosity $L_{\text{IR}}[8-1000\mu\text{m}]$ (right axis) vs. redshift for the MIPS 24 μm sample with spectroscopic redshifts. This figure illustrates the strong luminosity evolution of the Mid-IR population. The L_{IR} was derived using luminosity dependent SED template suites from the literature (see text for details). The dashed lines define the L_{IR} regions that classify LIRGs ($L_{\text{IR}} \geq 10^{11}L_{\odot}$) and ULIRGs ($L_{\text{IR}} \geq 10^{12}L_{\odot}$). The star formation rates (plotted on left axis) in M_{\odot}/yr for all the 24 μm sources with spectroscopic redshifts between $0.1 \leq z \leq 1.3$, assuming the calibration from Kennicutt (1998).

phases would be responsible for $\sim 30 - 40\%$ ($0.6 \times 70\%$) of the SFR density at $z \sim 1$, since IR activity traces dusty star formation.

The second more detailed approach utilizes the SFR's directly arising from our sample of mergers and interactions. At $1.0 \leq z \leq 1.3$ we find that 59% (12 close pairs, and 17 later stage mergers) of galaxies detected at $24\mu\text{m}$ in our spectroscopic sample are involved in some stage of an interaction or merger. When dealing with density measurements we must account for the fact that our sample is only considering a small fraction of the total population of galaxies within a given volume. To correct for this we derived a scaling factor (~ 7) simply by comparing the number of observed objects of a given L_{IR} ($1.0 \times 10^{11.5}$) in a specific redshift range to the number expected from models (Lagache et al. 2004; Le Floc'h et al. 2005). However, to go any further we must assume that our spectroscopic sample is representative of this population at ~ 1 , and by all accounts this appears to be true (see 2.3.2).

Using the derived pair fraction we can then infer the total number of major mergers and interactions occurring (fulfilling our criteria) in a given volume and L_{IR} limit. The lower limit of the SFR density at $z \sim 1$ from merging and interacting galaxies is found to be $0.066 \text{ M}_\odot \text{yr}^{-1} \text{Mpc}^{-3}$. Using the extinction corrected "Lilly-Madau" plot to estimate the SFR density at $z \sim 1$ ($0.16 \text{ M}_\odot \text{yr}^{-1} \text{Mpc}^{-3}$ at $z = 1$) (Thompson et al. 2001), we find that mergers and interactions are responsible for at least 42% of the SFR density at $z \sim 1$ (assuming mergers contribute 60% of the IR density). Both approaches are in good agreement, and are only a lower limit, since objects flagged as AGN were not considered even though some of their L_{IR} is likely a result of star formation, and minor mergers which have been shown to also induce bursts of star formation were not included.

3.8.3 Mergers and the SFR Density: Implications

These results have interesting implications for the physical mechanisms that drive the decline in the cosmic SFR (CSFR) density from $z \sim 1$ to present day. They suggest that when all stages of the merger process are considered (pre-merger to later stage merger) major interactions and mergers contribute close to half of the $z \sim 1$ SFR density, and the decline in the number of $24\mu\text{m}$ detected mergers/interactions is a significant, but perhaps not the primary driver for the decline in the cosmic SFR.

This conclusion differs in interpretation from Bell et al. (2005); Melbourne et al. (2005); Wolf et al. (2005); Lin et al. (2006); Lotz et al. (2006) which generally suggest that the evolution of the merger rate is not a significant underlying cause of the decline in the cosmic SFR, but rather a strong decrease in the SFR of morphologically undisturbed spiral galaxies is the dominant mechanism. Their results do not preclude the possibility that their "star forming (undisturbed) disks" could be in close pairs, and when we only consider quantitatively defined morpholog-

ical mergers our results are consistent with theirs, stressing the importance of considering the merger process in its entirety. It must also be mentioned that we are probing to higher redshifts than (Bell et al. 2005), which found that major galaxy mergers account for $\leq 30\%$ of the IR luminosity density at $z \sim 0.7$, consistent with our findings of 35% at that redshift. Our results also agree that at $z \sim 0.7$ isolated undisturbed spiral galaxies are a primary contributor, however, the influence shifts to interactions and mergers at $z > 0.7$.

Our findings point to an increased importance of MIPS bright interactions and mergers to the IR luminosity density and SFR density at $z \geq 0.7$. This conclusion is not hampered by the small statistics of the $z > 1$ bin. Figure 3.13 shows the IR luminosity density contribution from interactions/mergers at $z \sim 0.7$ to be $\sim 37\%$ and 52% at $z \sim 0.9$, reinforcing this increasing trend.

3.9 Summary

Using a spectroscopic sample of field galaxies from the ACS component of the XFLS and dividing it into two subsets, those with a $24\mu\text{m}$ detection (above 0.1 mJy) and those without (or below) we identified optically merging/interacting systems via close pair statistics and morphological methods. We find that roughly 25% of galaxies emitting at $24\mu\text{m}$ have a close companion at $z \sim 1$ while at $z \sim 0.5$ only $\sim 11\%$ are in pairs. In contrast, those undetected at MIPS $24\mu\text{m}$ showed a pair fraction consistent with zero at all redshifts ($0.2 \leq z \leq 1.3$). On average MIPS $24\mu\text{m}$ galaxies are five times more likely than non-MIPS sources to have a close companion over $0.2 \leq z \leq 1.3$. When the samples are combined (regardless of $24\mu\text{m}$ flux) we find pair fractions consistent with previous studies (Lin et al. 2004; Bundy et al. 2004) showing little evolution with redshift.

An important and open question is the cause of star formation in LIRG galaxies at high- z . Some morphological studies have suggested that since at least half of the LIRG galaxies exhibit disk dominated morphologies (Bell et al. 2005; Lotz et al. 2006) at $z \sim 0.7$ and low non-evolving merger fractions (Lotz et al. 2006), that the driver of IR activity in high- z LIRGs is from ongoing star-formation from isolated gas-rich spirals and not merger or interaction induced. One bias of morphological studies involving the identification of merging/interacting systems is the limitation of detecting low surface brightness features such as tidal tails caused by close interactions, which can lead to an underestimate of the importance of mergers in the evolution of galaxies at $z < 1$. Ultimately, both close pair and morphological techniques must be applied and considered, to obtain a complete major merger timeline. Our analysis is the first to probe merger rate evolution combining close pairs and later stage mergers while considering the IR activity of these systems.

We find that close pair statistics, visually classified mergers, and those identified via quan-

titative CAS parameters all showed similar evolution in their merger rates. Fitting the merger rate evolution function $\mathfrak{R}(z) \propto (1+z)^m$ for $24\mu\text{m}$ detected mergers above 0.1 mJy , we find $m = 2.12 \pm 0.93$. This result agrees with previous claims of an increase ($m \geq 2$) of the merger rate out to $z \sim 1$ (Patton et al. 1997, 2000; Le Fèvre et al. 2000; Conselice et al. 2003; Cassata et al. 2005), however these studies did not consider the Mid-IR properties of the data. This evolution however, is not seen when IR faint ($< 0.1\text{ mJy}$) mergers are included, suggesting that it is the LIRG-merger population that is evolving with redshift.

The Mid-IR emission of LIRGs is indicative of dust enshrouded star formation (and some AGN activity), and at $z \geq 0.7$ they dominate the IR luminosity density and in turn the volume-averaged star formation rate density at $z \sim 1$. We estimate that close galaxy pairs are responsible for $\sim 27\%$ of the IR luminosity density resulting from star formation at $z \sim 1$, while later stage mergers contribute $\sim 35\%$. This implies that 40-60% of the infrared luminosity density at $z \sim 1$ can be attributed to galaxies involved in some stage of a major merger, indicating that merger-driven star formation is responsible for 30-40% of the star formation density at $z \sim 1$. This value is a lower limit since minor mergers and interactions/mergers with an AGN were not considered.

Ultimately, our findings suggest that interactions and mergers of LIRG phase galaxies play an increasingly important role in both driving the IR luminosity of these systems and the SFR density from $z \geq 0.7$ out to $z \sim 1.3$. They appear to be vital to our understanding of the evolution and mass assembly of luminous IR galaxies.

Chapter 4

Observations and Data Analysis: The CFHTLS - Deep Survey

4.1 Introduction

The CFHTLS-Deep survey covers an area 30x (4 sq. degrees) that of XFLS and to comparable depths (in the i' -band), allowing us to probe merger statistics with a higher level of confidence. This large well defined sample of galaxies is used to establish a lower limit on how interaction and merger fractions evolve with redshift and their role in star formation and AGN activity out to $z \sim 1$.

This chapter details the data on which this work is partially based (specifically Chapter 5). These data include the 5-band optical imaging of the CFHTLS Deep component from CFHT's MegaCam, the IRAC and MIPS imaging from the *Spitzer* SWIRE survey, as well as the photometric redshift catalog derived by our group.

4.2 CFHTLS: Survey Overview

The CFHT Legacy Survey is a joint community project between Canada and France with more than 450 nights over a 5 year period that commenced in 2003. The survey utilizes the wide field imager MegaPrime equipped with MegaCam having 36, 2048x4612 pixel CCDs covering a 1 deg. \times 1 deg. field of view with a pixel scale of 0.187''. The CFHTLS is comprised of three survey components: 1) a 410 square degree very wide and shallow survey ("Very Wide"), 2) a 170 square degree wide survey ("Wide"), 3) and a 4 square degree "Deep" survey. This work focuses solely on the Deep survey component.

The optical data presented in this chapter have been acquired as part of the survey, and have been reduced, processed and stacked within the CFHTLS Supernova Survey (SNLS) col-

laboration. Therefore the imaging, and photometric catalogs including redshifts used in this work are not public. However, Terapix has separate stacked mosaics and photometric catalogs of the survey fields that have been publicly released (see the "Canadian Data Astronomy Data Centre" for details on data releases¹).

4.2.1 The CFHTLS - Deep Survey

The CFHTLS Deep survey is uniquely built to address many open and unconstrained scientific questions by obtaining deep 5-band (u^*, g', r', i', z'), optical imaging over 4 square degrees. The primary scientific driver is the determination of the cosmic equation of state, derived from the use of supernova measurements. Hence the observing strategy for the Deep survey was tailored to the requirements of the SNLS (see Sullivan et al. 2006b,a, for details). However, the high image quality and depth of the survey lends itself to numerous other scientific applications, such as the study of large scale structure, clustering, merger rates, morphology and testing of galaxy formation and evolution models within the CDM paradigm, to name a few.

One of the primary objectives of this thesis is to investigate the role merging plays in star formation and AGN activity as a function of redshift, by visually identifying interacting systems using the larger CFHTLS-Deep sample (15x larger than XFLS).

The four survey fields were chosen to have low galactic extinction and were distributed in right ascension for efficient observing throughout the year. These fields were also targeted by numerous other surveys, providing a plethora of ancillary data (Table 4.1). As the survey is still ongoing (80% complete)² Table 4.2 outlines the current and expected magnitude limits upon survey completion.

Although all four Deep fields were reduced, stacked and photometrically analyzed, the detailed analysis that follows only includes the D1 and D2 fields. The area and survey depth of just 2 square degrees provides a large enough sample size to confidently investigate our science goals. However the other two fields (D3 & D4) will be folded into our sample at a later date. The D1 and D2 fields were analyzed first, due to their ancillary data, specifically and ACS.

4.2.2 Optical Imaging

The CFHTLS-Deep optical images used in this thesis were a data product of the SNLS program and were generated using the SNLS's data reduction, stacking and mosaicing pipeline. Their methods are outlined in Sullivan et al. (2006b).

¹<http://cadcwww.dao.nrc.ca>

²During the course of writing this dissertation the MegaCam i' filter was destroyed. It is unclear at the time this work was submitted as to the projected survey completion date.

Table 4.1: CFHTLS-Deep Survey Field Locations

Field	R.A. (J2000.0)	Decl. (J2000.0)	Ancillary Data
D1	02 26 00.00	-04 30 00.0	SWIRE, <i>XMM</i> , <i>GALEX</i> , VIMOS, VLA
D2	10 00 28.60	+02 12 21.0	COSMOS/ACS <i>Spitzer</i> , VIMOS, VLA, <i>GALEX</i>
D3	14 19 28.01	+52 40 41.0	<i>Spitzer</i> , Deep-2, <i>GALEX</i>
D4	22 15 31.67	-17 44 05.7	<i>XMM</i> , <i>GALEX</i>

Table 4.2: CFHTLS-Deep: Magnitude Limits

Field	Limiting Mag. (AB) (u^*, g', r', i', z')	Expected Limiting Mag. (u^*, g', r', i', z')
D1	27.4, 27.8, 27.4, 27.3, 26.0	28.0, 28.2, 27.8, 27.7, 26.3
D2	26.3, 27.6, 27.2, 27.1, 25.9	28.0, 28.2, 27.8, 27.7, 26.3
D3	27.3, 27.8, 27.4, 27.2, 25.9	28.0, 28.2, 27.8, 27.7, 26.3
D4	27.4, 27.7, 27.3, 27.1, 25.9	28.0, 28.2, 27.8, 27.7, 26.3

The limiting magnitudes are taken from the Deep Survey's website (<http://www.ast.obs-mip.fr/article204.html>). They include all data up to D1: 02/2007, D2 & D3: 04/2007, D4: 12/2006.

Deep optical stacks with a precise astrometric solution were produced for each of the filters (u^*, g', r', i', z') for all four fields using "Elixir" processed images (Magnier & Cuillandre 2004). Given that we are studying the structural appearances of galaxies a key requirement of the imaging is good resolution, which requires good seeing. Our aim was to maximize exposure depth while retaining excellent seeing in the final stacks. To achieve this we required that only images below a seeing limit ($S_{limit} \sim 4$ pixels) were used in making the final stacks. Since seeing is $\propto \lambda^{1/5}$, different filters required slightly different seeing cuts. The typical seeing of the final stacks is 0.7-0.8"(in i' -band). Table 4.3 outlines the final total exposure times for each filter for a given field with the seeing cut imposed.

Table 4.3: CFHTLS-Deep: Final Stacks

Field	Filter	Total Int. Time [hours]
(0.959 sq. deg.)	u^*	10.6h
	g'	9.5h
	r'	18.8h
	i'	45.1h
	z'	20.0h
(0.900 sq. deg.)	u^*	3.4h
	g'	5.7h
	r'	10.7h
	i'	22.2h
	z'	12.0h

Note: The seeing cut imposed on D1=4.0 pixels, D2=4.2 pixels.

4.2.3 Optical Catalogs

Source extraction and photometry were performed on each Deep fields using SExtractor (Bertin & Arnouts 1996) in dual image mode. Detections were performed in the i' filter (the filter with the deepest data) and photometry measurements calculated in each of the 5 filters, u^*, g', r', z' . There are numerous bright stars that occupy the fields resulting in diffraction spikes and stellar halos which can affect the accuracy of the photometry. Figure 4.1 illustrates the regions masked out in D2, which was more heavily masked than D1 since it contained a larger number of bright objects. We applied a bad pixel mask to the image prior to running the source detection to eliminate noisy or contaminated regions. The total area masked is $\leq 10\%$ for each field.

Numerous photometric and structural parameters are measured for each galaxy. Specifically, we use SExtractor's MAG AUTO flux values and associated errors throughout this work ($\text{apparent magnitude} = -2.5 \log(\text{flux auto}) + \text{zeropoint}$). The MAG AUTO function uses a flexible elliptical aperture with a characteristic "Kron" radius (Kron 1980). By configuring SExtractor to measure fluxes inside 2.5 Kron radii, $\sim 90\%$ of an object's light is being measured in each aperture (Infante 1987; Graham & Driver 2005). Running SExtractor in dual image mode ensures that the same MAG AUTO aperture is used in the different filters, reducing aperture mismatches. The weight image (rms) of the final stacks are used to determine the statistical errors in the flux measurements. Stars were removed from the catalogs in the same manner described in section 2.2.4. Our adopted value for the star/galaxy separation is again CLASS STAR ≥ 0.9 (meaning stellar object).

As mentioned earlier, the Deep Survey fields were chosen to have low levels of galactic dust extinction. Figure 4.2 shows the Schlegel dust maps (Schlegel et al. 1998) for both the D1 and D2 fields. The average dust correction in the i' filter was found to be 0.063 mags for D1 and 0.042 mags for the D2 field. Each object in the Deep survey was corrected for this extinction.

4.2.4 Number Counts

We derived the I -band number counts for our fields and compared them with other surveys as a check of the approximate photometric calibration and depth of the data. The raw I -band number counts (*i.e.* we have not correct for incompleteness at the faint end) for both the D1 and D2 fields, are plotted in Figure 4.3, alongside counts from the HDF North, South (Williams et al. 1996; Metcalfe et al. 2001) and the COSMOS field (Leauthaud et al. 2007) that overlaps with the D2 field. The number count differences between fields was investigated. At bright apparent magnitudes ($I \lesssim 22$) the variation between the D1 and D2 fields with COSMOS is a result of a more aggressive stellar removal criteria applied by the COSMOS group (Leauthaud

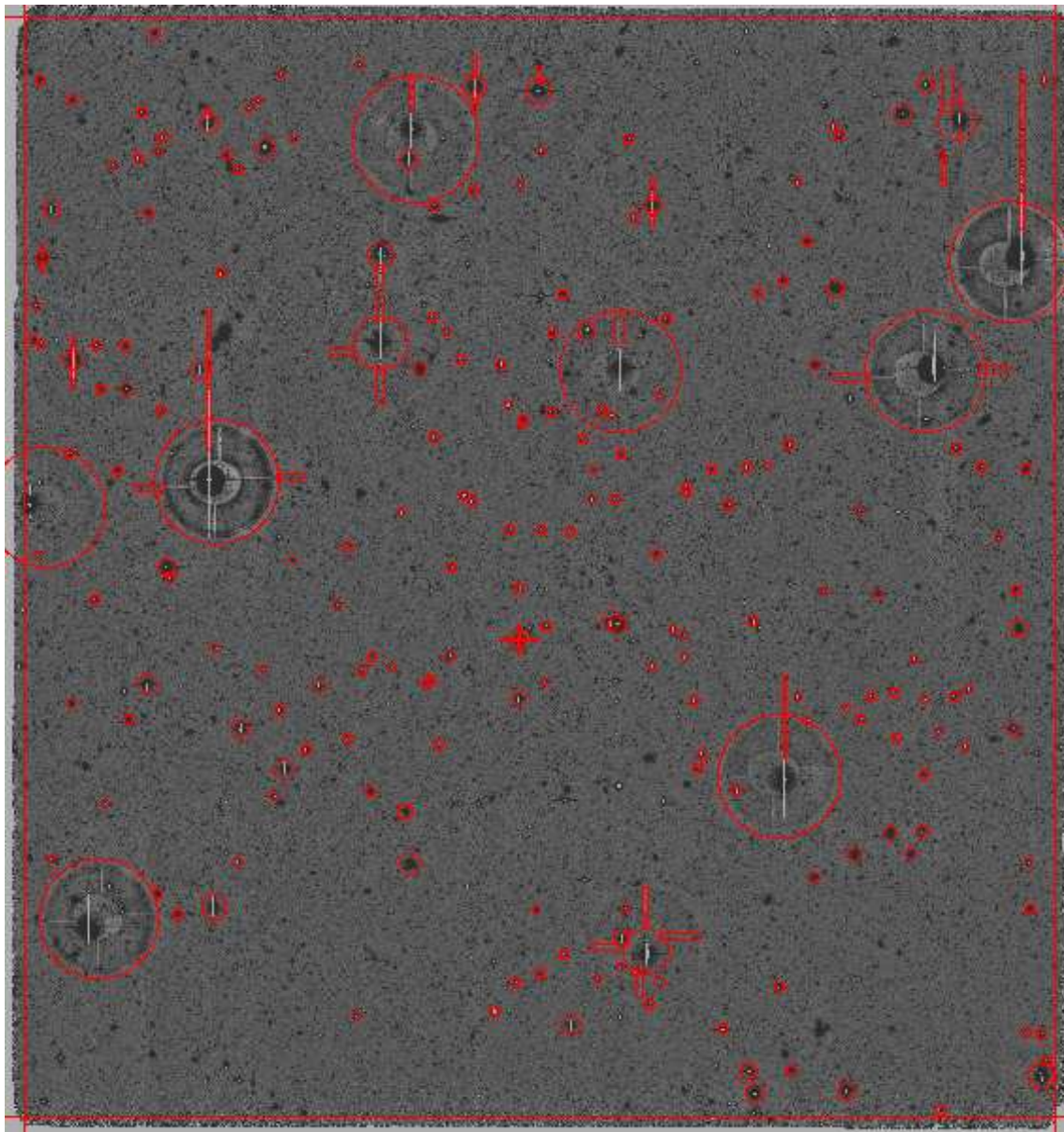


Figure 4.1: The D2 i' -band stacked image is shown (1 sq. deg.). The outlined areas (red) illustrate the regions of the sky masked out due to contamination by diffraction spikes, and stellar halos. Bad pixel masks were applied separately prior to the source extraction. The mask removes < 10% of the area.

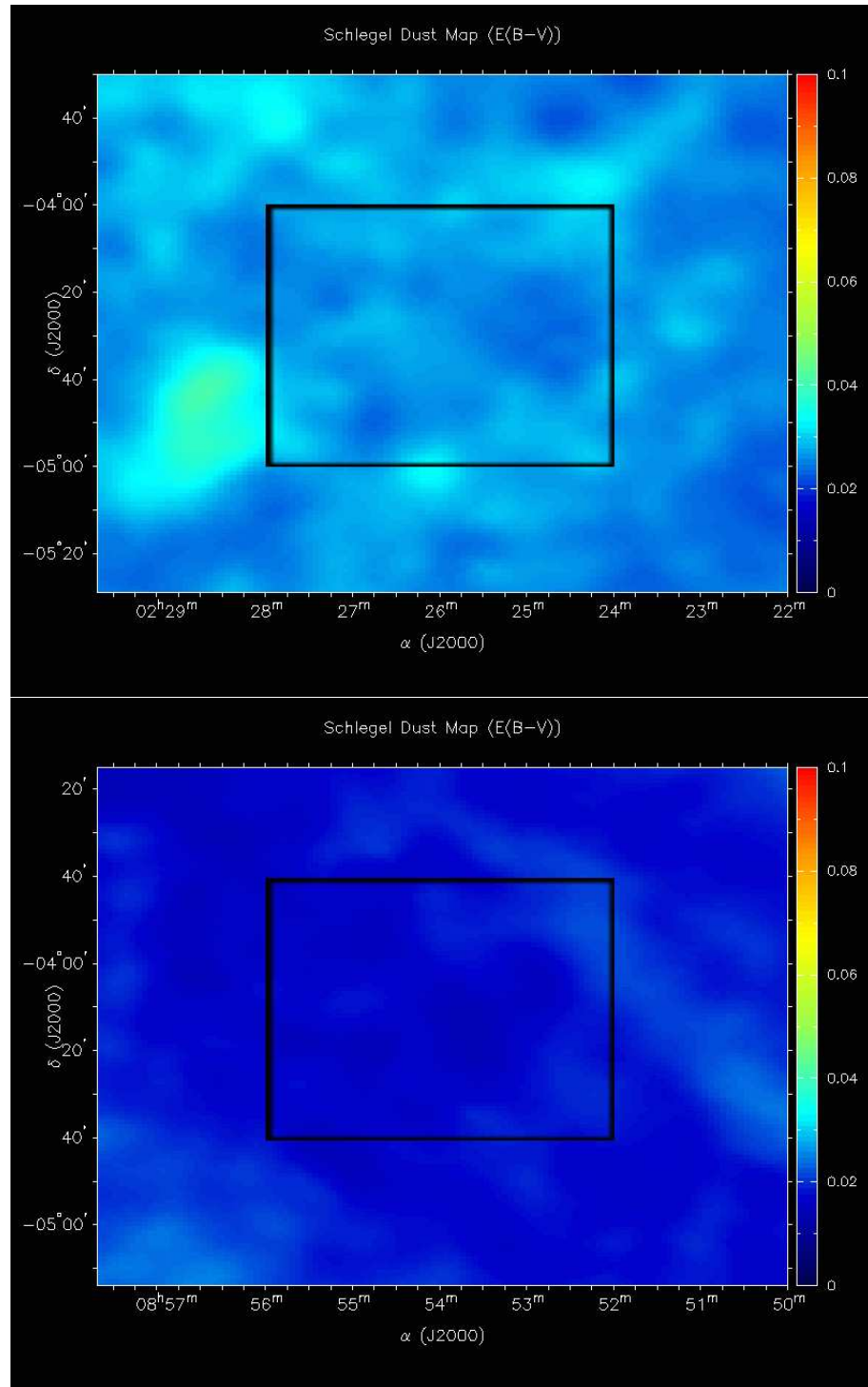


Figure 4.2: The Schlegel dust maps (Schlegel et al. 1998) for the D1 (Top) and D2 (Bottom) fields. The inner square outlines the region covered by the respective fields. There is an $E(B-V)$ difference of 0.02 between the two fields, with an average i extinction of 0.063 mags (D1) and 0.042 mags (D2).

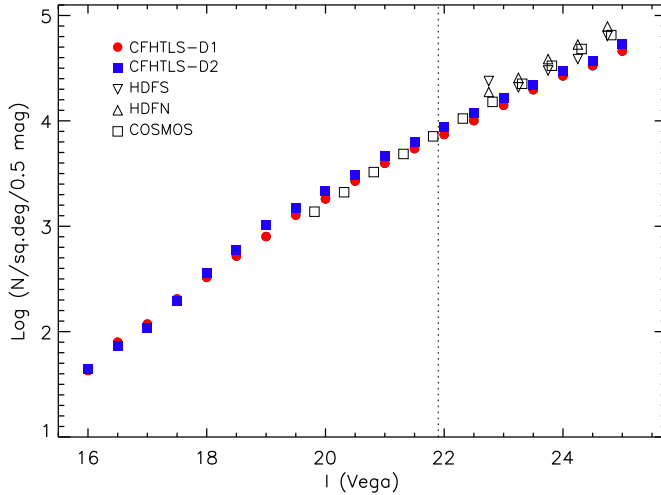


Figure 4.3: The I -band number counts for the D1 (red,circle) and D2 (blue,square) CFHTLS-Deep fields. Works from other deep surveys are plotted for comparison, COSMOS (open square) (Leauthaud et al. 2007); HDF-S (downward triangle), HDF-N (upward triangle) (Metcalfe et al. 2001). The vertical dotted line outlines the apparent I magnitude limit imposed on the work contained in this thesis ($I \leq 21.9$).

et al. 2007). The overall number count differences are on the order of $\sim 6\%$, which is consistent with variations that could arise from cosmic variance. At fainter magnitudes the number counts do begin to diverge more significantly, however this thesis work focuses only on galaxies brighter than $i'_{AB} \sim 22$, a magnitude range where the number counts are consistent with other works.

4.3 Galaxy Properties

This section details the techniques used for deriving the galaxy properties utilized in the subsequent analysis, presented in Chapter 5. We outline the method used to convert the optical fluxes of our sources from §4.2.3 into a photometric redshift estimate and other galaxy properties, such as the stellar mass and star formation rate (SFR).

4.3.1 Photometric Redshifts

In order to study the potential evolution of the interaction and star formation rates of galaxies we need to derive a redshift estimate for each galaxy. Although spectroscopic redshifts are the most precise distance measures, they are observationally expensive to obtain for large samples. A strength of the CFHTLS-Deep survey is its high quality 5-band optical imaging, which can be used to derive a photometric redshift estimate. The 5 optical bands can be combined to

produce a broad band spectral energy distribution (SED), that can be compared to a set of template SEDs to estimate properties of the galaxy such as, its redshift, age, stellar mass, and SFR (Baum 1962; Loh & Spillar 1986). This technique uses broad spectral features like the 4000Å discontinuity or the Lyman break for comparison to templates.

We fit a series of galaxy template SEDs to the broad band fluxes of each galaxy. The best-fit SED is determined through a standard χ^2 minimization procedure between the synthetic photometry generated by integrating the template SEDs through the CFHTLS filters, and the observed fluxes (including the flux errors). We specifically use the Z-Peg template fitting code provided by D. Le Borgne. Its methodology is similar to that applied by other photometric redshift codes (e.g. Gwyn & Hartwick 1996; Bolzonella et al. 2000; Le Borgne & Rocca-Volmerange 2002).

We employ a set of synthetic templates computed with the PEGASE-II galaxy evolution code (Fioc & Rocca-Volmerange 1997; Le Borgne & Rocca-Volmerange 2002; Le Borgne et al. 2004). Both the SEDs and the photometric redshift code have been extensively tested and used in the literature (e.g. McCarthy et al. 2004; Grazian et al. 2006; Sullivan et al. 2006b). We use eight evolutionary scenarios that evolve self-consistently with age and assume a Rana Basa initial mass function (IMF). These scenarios were designed to match the average colours of local galaxies and to reproduce deep galaxy number counts. Considering several tens of time-steps for each scenario, the total number of synthetic SEDs is ≈ 500 . When fitting a given galaxy only templates younger than the age of the universe at the redshift of the galaxy are considered.

For each galaxy, the entire probability distribution $P(z)$, the most likely redshift and the “ 1σ ” errors (described in terms of a minimum and maximum redshift) are calculated. We only consider galaxies with a $z_{max} - z_{min} < 0.5$ to ensure a high level of confidence in the redshift estimate (D. Le Borgne 2006, private communication).

The accuracy of the photometric redshifts is determined by comparing them to the SNLS spectroscopic sample in our fields (Sullivan et al. 2006b). Figure 4.4 shows the comparison between the photometric and spectroscopic redshift estimates for SN host galaxies in the Deep fields. The photometric accuracy down to $i' \sim 22.5$ is :

$$\sigma_{\Delta z}/(1 + z_s) = 0.04 \quad (4.1)$$

4.3.2 Optically Derived SFRs and Stellar Masses

Two physical parameters of particular interest are the SFRs of interacting galaxies and their stellar masses. These quantities are both derived using the Z-Peg code (Le Borgne & Rocca-

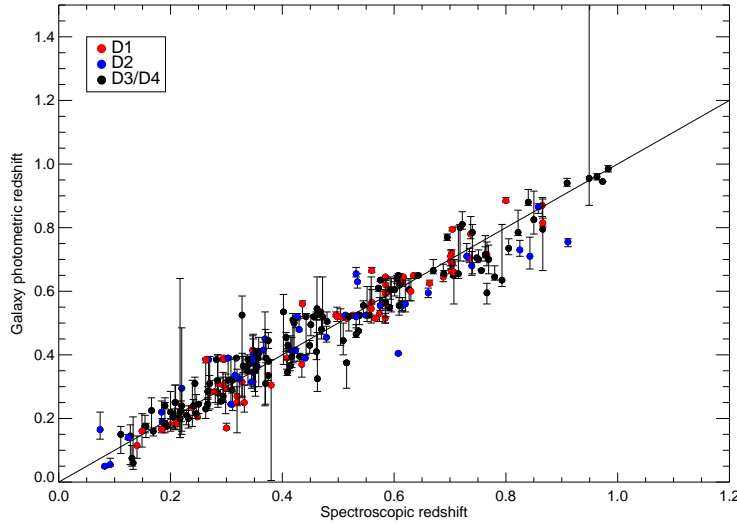


Figure 4.4: A Comparison of spectroscopic and photometric redshift estimates for the SNLS supernova host galaxies in the CFHTLS-Deep fields (Sullivan et al. 2006b). This figure was constructed to have a similar i' -band cut ($i < 22.5$) to that used in our analysis in order to illustrate the photometric redshift accuracy of our sample. The solid line shows a 1:1 agreement between the photometric and spectroscopic redshift.

Volmerange 2002). The *mean* recent SFR for a galaxy is determined from the best-fit SED, averaging the SFR over a period of 0.5 Gyrs. The total stellar mass of a galaxy was derived by integrating the total star formation history (SFH) of the best-fit scenario, up to the best-fit age and subtracting off the mass from stars that have died.

4.3.3 Mid-IR Imaging

As mentioned earlier, a large fraction of emitted starlight in galaxies is absorbed and re-emitted by dust in the thermal infrared. Since luminous IR galaxies become increasingly important systems to the IR luminosity and cosmic star formation rate densities of the Universe, probing galaxies in the Mid-IR is essential for a complete picture of galaxy evolution.

The CFHTLS-D1 field overlaps with 0.85 sq. degrees of the *Spitzer* SWIRE (*Spitzer* Wide-area InfraRed Extragalactic) legacy survey (see Figure 4.5). The SWIRE survey covers 49 square degrees over 6 different fields in all 7 infrared colours available to *Spitzer*. Its primary science objectives were to trace the evolution of dusty, star-forming galaxies, AGN, and evolved stellar populations out to $z \sim 3$.

In this work we utilize the public data 2 release (DR2) of the SWIRE photometry for the general field population.³ Through collaboration with the SWIRE team we have obtained less

³Data can be obtained through the SWIRE legacy survey website

restrictive catalogs (CD1) for the sample of interacting galaxies defined in the next section. The data reduction techniques are described in Surace (2005), and the flux limits of the data used in this work are outlined in Table 4.4.

For any source to be included in the DR2 it had to be detected at both $3.6\mu\text{m}$ and $4.5\mu\text{m}$. The detection thresholds were set to a SNR of 10 at $3.6\mu\text{m}$ and 5 at $4.5\mu\text{m}$ ($10\mu\text{Jy}$). The less restrictive CD1 catalog placed a SNR cutoff of 5 on each band.

Table 4.4: *Spitzer* :D1 IRAC and MIPS Sensitivities

Sample	IRAC [μJy]				MIPS [μJy]
	$3.6\mu\text{m}$	$4.5\mu\text{m}$	$5.8\mu\text{m}$	$8.0\mu\text{m}$	
DR2....	10	10	43	40	450
CD1....	4	6	31	36	340

4.3.4 Band Merging: Optical, Mid-IR

The D1 optical catalog was merged with SWIRE data sets in a similar manner as that described in section 2.3.1. A $1.5''$ search radius was used for object matching from the $3.6\mu\text{m}$ channel to the i' band. The SWIRE catalogs contained duplicate objects due to overlapping regions of sky from dithering. In such cases the object with the highest $3.6\mu\text{m}$ SNR was selected to be band merged with the optical. We find that $\sim 70\%$ of the D1 objects in the SWIRE region were detected by IRAC, while 12% were found to be MIPS $24\mu\text{m}$ sources (see Figure 4.5).

This chapter has introduced the optical CFHTLS-Deep survey, the photometric redshift estimates and associated Mid-IR ancillary data, used throughout the analysis in proceeding chapter. We have corrected the optical photometry for galactic dust extinction, removed stellar contamination, and optimized the image quality through seeing restrictions. Using the optical CFHTLS-D2 catalog and the band-merged (optical to Mid-IR) catalog from the D1/SWIRE field we commence our investigation into the interaction and star forming properties of the sample.

(<http://swire.ipac.caltech.edu/swire/astronomers/dataaccess.html>) or through the IPAC Gator site (<http://irsa.ipac.caltech.edu/applications/Gator/>).

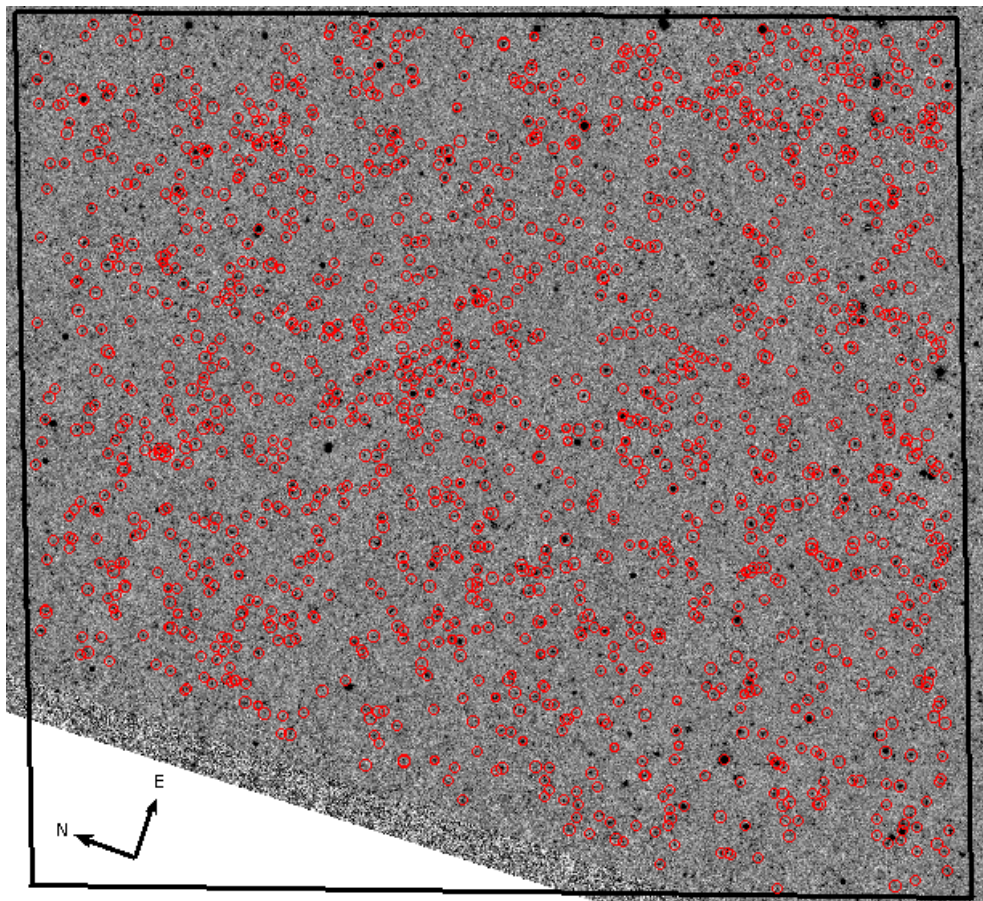


Figure 4.5: The Spitzer 24 μm image that overlaps with the 1 square degree CFHTLS-Deep D1 field (outlined). The red circles mark the 24 μm sources. The SWIRE image is available from <http://irsa.ipac.caltech.edu/applications/Gator>.

Chapter 5

Results From The CFHTLS - Deep Survey

5.1 Introduction

The presence of long tidal tails or bridges are nearly a foolproof signature of imminent mergers. Moreover, tidal tails are a relatively simple, completely dynamical phenomenon that can be studied in detail with N-body simulations. In spite of these positive features little work on galaxies with tidal tails has been done at high redshift. The reason is simple: tails have a relatively low surface brightness and are fairly rare. Deep optical imaging over a large area, like that found in the CFHTLS-Deep survey, is required to identify enough of these tell tale signs of merging to confidently probe the evolutionary impact of interactions on galaxy properties.

The first step in probing the evolutionary properties of interactions is to define a sample of such galaxies. We have developed a new classification scheme to identify interacting galaxies based on the presence of tidal features. By visually classifying all galaxies in the CFHTLS-D1 and D2 fields down to $i_{vega} = 22.2$ ($\sim 27,000$ galaxies) we have compiled the largest catalog of interacting galaxies from low to high redshifts.

In this chapter the main results of the survey which were obtained directly from the optical and Mid-IR data are discussed. A new method of identifying interacting and merging galaxies is presented. The resultant catalog of interacting galaxies has allowed us to measure the interaction fraction as a function of mass and redshift, while probing the star formation rate, potential AGN activity and Mid-IR properties of these systems.



Figure 5.1: A montage of interacting and merging galaxies. Starting from the left going clockwise: Arp295; The cartwheel galaxy; NGC 520; NGC 4676 (The Mice); NCG 4038/39 (The Antennae); NGC 2207, IC 2163. Images from Hibbard & van Gorkom (1996), and the Hubble Heritage Team, NASA.

5.2 Identifying Interacting Galaxies

The first step in studying the frequency of galaxies involved in an interaction is to define a clean, robust and useful definition of an interacting galaxy. Morphologically, interacting galaxies can exhibit long tidal tails, bridges (linking two or more galaxies), ring structures, stellar bars and/or enhanced spiral structure and frequently appear severely distorted (see Figure 5.1). We have focused our identification methods on confidently selecting galaxies which have recently undergone or are presently undergoing a tidal interaction. The presence of a tidal tail or bridge is incontrovertible evidence of a recent interaction. Ultimately, we define an **interacting galaxy to be one with strong signatures of a tidal tail or bridge**.

There are two different avenues one can take to morphologically select interacting galaxies. The first is to utilize quantitative morphological software that measures a galaxies structural parameters, such as its asymmetry. As a galaxy undergoes a merger its symmetry can be affected (see Figure 5.16). The asymmetry of a galaxy can help describe the level of a galaxy's disturbed appearance (Abraham et al. 1996b,a; Conselice et al. 2000), and can be used to identify mergers (i.e. $A > 0.35$).

This is an efficient and automated approach. However, a complication of this method is the requirement that all the pixels pertaining to a galaxy be assigned or extracted correctly. A galaxy with a tidal tail or bridge can result in high asymmetry values, allowing it to be identified as an interaction, but the thin sometimes low surface brightness properties of tails and bridges make them difficult to correctly extract. These structures can be designated as separate objects, or not identified at all if their surface brightness is close to that of the background. Figure 5.2 illustrates this point by showing a CFHTLS merger and how the tidal tail and bridge are not extracting fully nor correctly. Parts of the tidal tail are considered a separate object while some portions of the tidal bridge are not extracted at all.

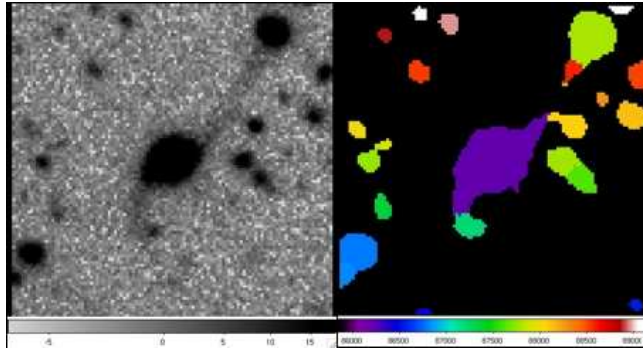


Figure 5.2: Left: An example of an interacting system in the CFHTLS-Deep survey. The i' image is $100h^{-1}\text{kpc}$ on a side, and reveals a bridge linking two galaxies together, and a tidal tail streaming from the lower galaxy. The right hand image is the colour coded segmentation map. Each colour represents a separate object extracted using SExtractor. Clearly, the tidal bridge is only partially detected and is broken up into multiple sources. Similarly, the tidal tail is also segmented into two sources.

Parameters in the extraction software (SExtractor) can be altered to better detect these thin low surface brightness features at the cost of dramatically increasing the number of false detections. Faint artifacts could be considered sources, while other previously single objects could be broken up into multiple components.

The second method of identifying interacting galaxies is based on pure visual inspection. This technique has been utilized by many in the past to morphologically classify galaxies (Hubble 1926; Vorontsov-Velyaminov 1959; Sandage 1961; Arp 1966, to name a few). Qualitative classification is able to identify the low surface brightness features that the automated method has difficulties with, as it utilizes one of the best pattern recognition computers - the brain-eye combination. A downfall of this method is that it can be laborious and subjective, and can suffer from reproducibility issues when the person conducting the classification changes. Although, when a set of visual criteria are clearly defined, and the features themselves are striking (e.g. long tidal tails and bridges) visual inspection can be a highly accurate method of morphological classification (see discussion in section 5.3).

Ultimately, to cover large deep areas of the sky the automated computer algorithms are the most efficient and quantitative, however a code currently does not exist specifically suited to detect tidal tails and bridges with a high rate of success. We have taken a first step towards this by visually identifying a large sample of interacting galaxies which can then be used to optimize software to detect these tidal signatures.

The work presented in this chapter utilizes the visual inspection technique to identify different morphological classes of galaxies, specifically those with strong evidence of an interaction.

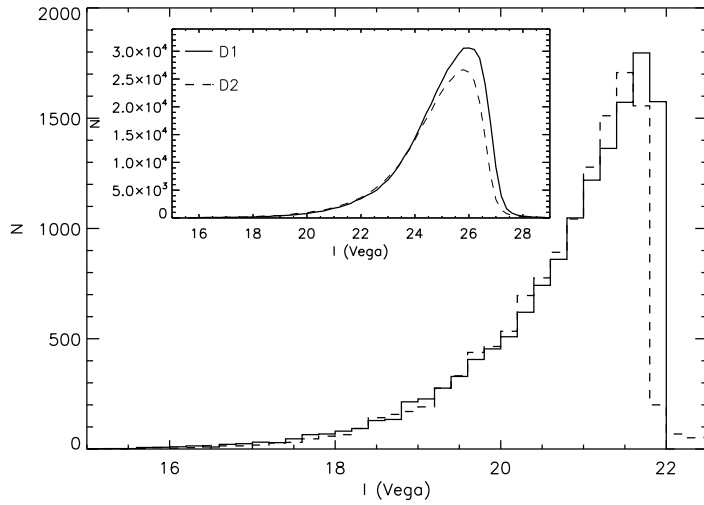


Figure 5.3: The apparent i' distribution for the CFHTLS- D1 and D2 fields. The inset figure outlines the full magnitude coverage of the entire CFHTLS samples. The primary plot highlights the i' distribution of the sample of galaxies used in the analysis of this thesis. A limit of $i' \sim 22$ was applied to ensure secure visual morphological classifications.

5.2.1 A New Classification Scheme

The large area, high quality, deep optical imaging of the CFHTLS-Deep survey makes it well suited to probe interacting galaxies. Although *HST* can resolve fine structures stunningly well, most surveys of its kind lack the required area to find a large number of interactions, as well as the multi-band imaging required to derive not only distance information in the form of a photometric redshift, but colour, mass, and star forming properties.

The CFHTLS-Deep catalog of interacting galaxies was constructed through the visual classification of all galaxies in the D1 and D2 Deep fields, covering 2 square degrees, down to an $i_{vega} < 22.2$ ($\sim 27,000$ galaxies). The apparent magnitude distributions for both the D1 and D2 fields are very similar at the bright end (see Figure 5.3). The small differentials are caused by a combination of D1 being deeper (more objects at the faint end), and covering 0.05 more square degrees, and having a lower number of bright stars than in D2, hence a smaller masked region.

Although our primary objective was to identify interacting systems we did include other morphological classifications such as chain galaxies, low surface brightness objects, galaxies with prominent spiral arms, bars, ellipticals, and sharp disks to name a few (see Table 5.1).

We classified galaxies as interacting or merging if they exhibited a tidal bridge or tail. We then further classified these objects according to the length of their longest tidal tail, the number of tails, and the configuration of the tails. The length of a tidal tail was defined in relation to the angular size of the host galaxy. We broke the tidal tail sample into three tail lengths:

“short tidal tails”, where the tail length is less than the diameter of the galaxy, “medium tidal tails”, where the tail length is approximately the size of the galaxy, and “long tidal tails”, where the tail is longer than the diameter of the host galaxy. These are known as the primary classifications (and were coded as 5,6,7). Two other primary classifications were galaxies with a tidal bridge (classified with a value of 8), and galaxies with a double nuclei (were given the designation 10). The second value given to each interacting object was a subclass, describing the number of tidal tails and their configuration. For example, a galaxy with a double nucleus, and two tidal tails (one long and one short), would be given a classification of “1072” (10 for double nucleus, 7 for long tail, 2 for 2 tails), while a galaxy with a tidal bridge, and an additional medium tidal tail would be designated “861” (8 for a bridge, 6 for medium tail, and 1 for one tail). Figure 5.2.3 provides visual examples of galaxies classified as interacting, while Table 5.2 outlines the classification scheme and the number of galaxies identified per class.

5.2.2 Methodology

Since more than 26,000 galaxies required classifying, we developed software that partially automated the visually classification process. An i' -band thumbnail and a colour composite (g', r', i'), both $100 h^{-1}\text{kpc}$'s on a side, were generated for every object brighter than $i'_{\text{vega}} \leq 22.2$. Each object's i' -band fits image was viewed on a computer screen using DS9, and the user enters a classification through keyboard entry which is logged to a file. As each object was classified the software automatically displayed the next galaxy for classification. The benefits of displaying each object using a package like DS9 is the ability to adjust the scaling, contrast, and zoom levels of each image interactively to highlight faint structures such as tidal tails. The software package also allows the user to stop or pause the classification process and begin again at a later date, starting where they last left off.

5.2.3 Classification Limits

Since a goal of this work is to confidently identify interacting galaxies we only consider galaxies with an apparent $i' \leq 21.9$. Figure 5.4 illustrates how the number of objects that could be classified changes as a function of i' -band magnitude. At bright apparent magnitudes the number of unclassified objects is elevated as these galaxies are located in the halos of stars or diffraction spikes that were not masked out, causing their photometry to be contaminated by star light. The classified fraction levels off between $17.0 \lesssim i'_{\text{vega}} \lesssim 21.8$, and begins to rise beyond $i'_{\text{vega}} > 22$ as the objects become increasingly difficult to classify, due to their smaller angular size and apparent magnitude. The dashed line in Figure 5.4 represents the magnitude cutoff ($i'_{\text{vega}} < 21.9$) at which we can confidently classify galaxies in the CFHTLS-Deep survey. All

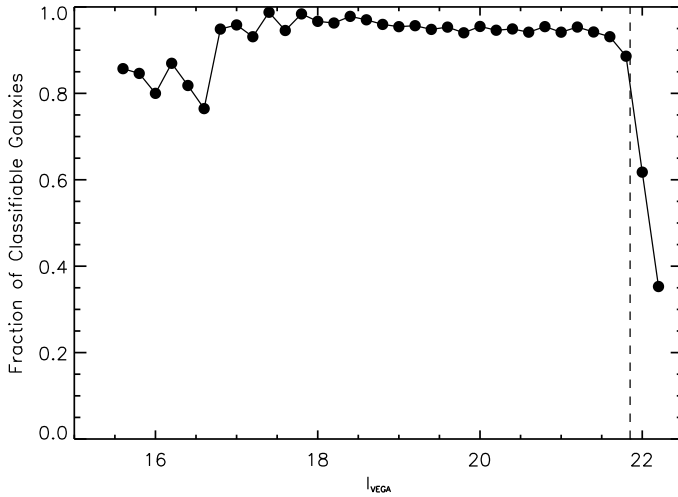


Figure 5.4: The fraction of sources that could be classified as a function of apparent i' magnitude. The dashed line defines the magnitude cutoff of $i' = 21.9$, where $> 85\%$ of galaxies could be classified.

analysis that follows considers only galaxies brighter than this magnitude limit ($i' \leq 21.9$).

Table 5.2 and 5.3 describe in more detail the breakdown of the classifications for interacting galaxies. It also outlines the fraction that each subclass makes up of a specific primary classification (i.e. the fraction of long tailed galaxies with a “bunny ear” configuration like that of the famous Antennae).

The classifications used in following analysis when discussing “interacting or merging galaxies” are, 61-75,81,82,85,861-875,105,1061-1071, totaling 1586 galaxies, and are presented in Table 5.2. Galaxies exclusively with short tidal tails or objects whose only signature of an interaction is a double nuclei were not included as they are the less confident interacting classifications. However, galaxies with a short tidal tail were included if there was secondary evidence (presence of a double nuclei or a tidal bridge (classes 105,85)) that supported an interacting scenario for that particular system.

Table 5.1: Classification Scheme I: Codings and Descriptions for Non-Interacting Galaxies

Code	General Description	Counts
1	Disk dominated galaxies	10041
2	Bulge dominated galaxies	6996
3	Compact galaxies	399
4	Galaxies in bad regions; or too faint to classify	1566
13	Galaxies with a barred structure	247
14	Sharp Disks	169
15	Low Surface Brightness galaxies (LSB)	44
17	Bulge and disk (transitional)	315
18	Chain of galaxies	40
19	Galaxies with clear spiral arms	902
21	Elliptical galaxies	992
22	Elliptical galaxies with shells	16
23	Unknown	12
Total		20,747

Table 5.2: Classification Scheme II: Codings and Descriptions for Interacting Galaxies

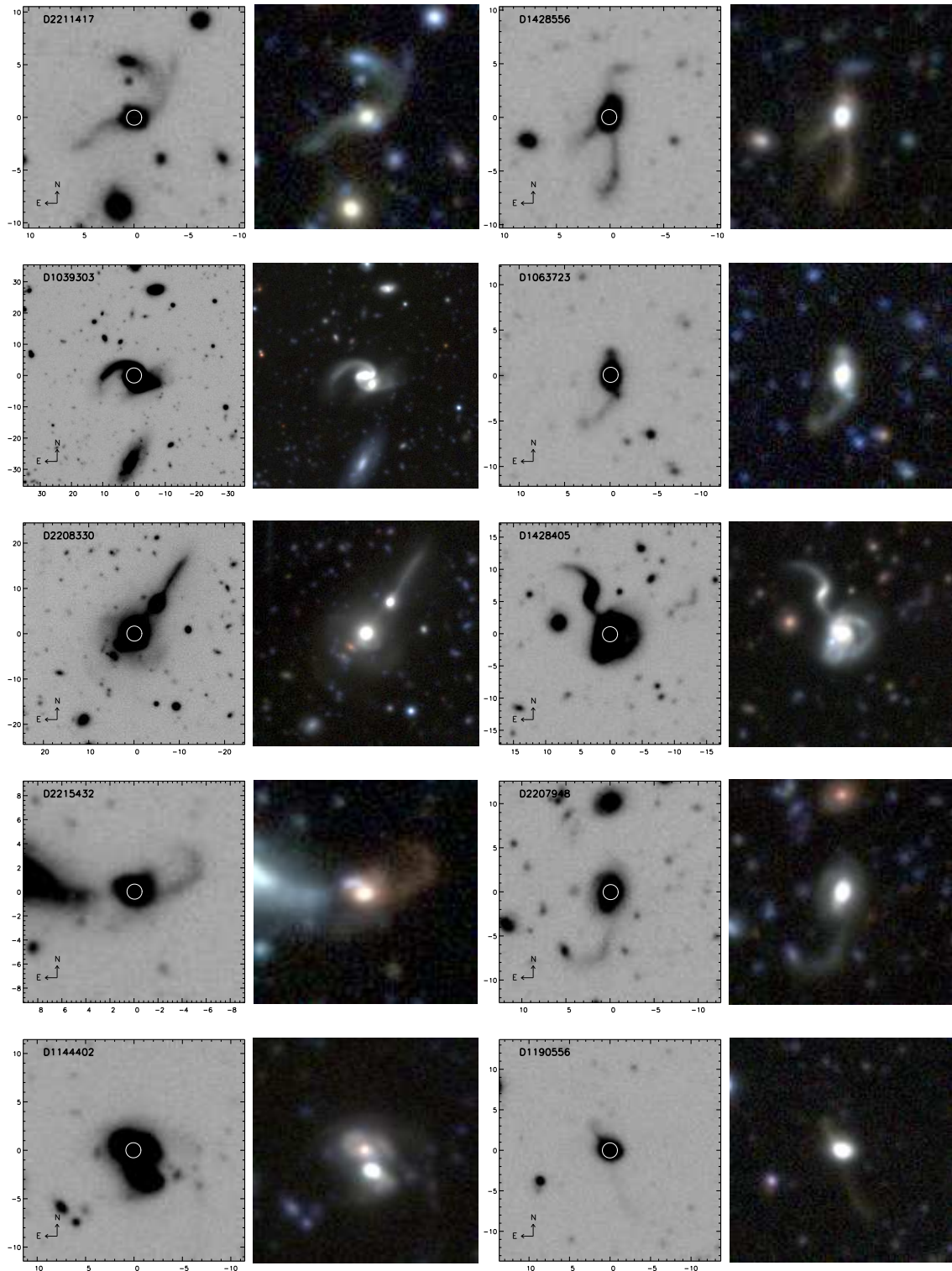
Code	General Description	Counts
"Short Tidal Tails": Tail Length < Diameter of Host		
5	Galaxies with a short tidal tail	586
"Medium Tidal Tails": Tail Length ~ Diameter of Host		
61	Galaxies with a medium length tidal tail: 1 tail	293
62	Galaxies with a medium length tidal tail: 2 tails	111
63	Galaxies with a medium length tidal tail: > 2 tails	13
64	Galaxies with a medium length tidal tail: Bunny Ears (2 tails)	27
65	Galaxies with a medium length tidal tail: Bunny Ears (>2 tails)	12
"Long Tidal Tails": Tail Length > Diameter of Host		
71	Galaxies with a long tidal tail: 1 tail	157
72	Galaxies with a long tidal tail: 2 tails	136
73	Galaxies with a long tidal tail: > 2 tails	15
74	Galaxies with a long tidal tail: Bunny Ears (2 tails)	47
75	Galaxies with a long tidal tail: Bunny Ears (>2 tails)	21
Close Galaxy-Galaxy Pairs with Tidal Bridges		
81	Galaxy in a close pair with bridge, no tail, disk dominated	292
82	Galaxy in a close pair with bridge, no tail, bulge dominated	194
85	Galaxy in a close pair with bridge, + short tidal tail	48
861-865	Close Pair with bridge + medium tail(s), + codings described in 61-65	49
871-875	Close Pair with bridge + long tail(s), + codings described in 71-75	50
Double Nuclei		
10	Galaxies with a double nuclei (DN), no tidal tail	384
105	Galaxies w/ a DN + short tail(s)	12
1061-1065	Galaxies w/ a DN + medium tail(s), + codings described in 61-65	47
1071-1075	Galaxies w/ a DN + long tail(s), + codings described in 71-75	62
Other Possible Galaxy Interactions		
9	Galaxies with a probable tidal tail	908
11	Disturbed galaxies (possible merger)	335
12	Irregular galaxies	225
16	Ring galaxies (or morphologically similar objects)	90
20	Galaxies with "S"spiral arms/potential mergers	588
24	Galaxies in a probable close pair (no strong bridge)	314
Number of Confidently Interacting Galaxies	(61-65,71-75,81,82,85,861-875,105,1065-1075)	1586

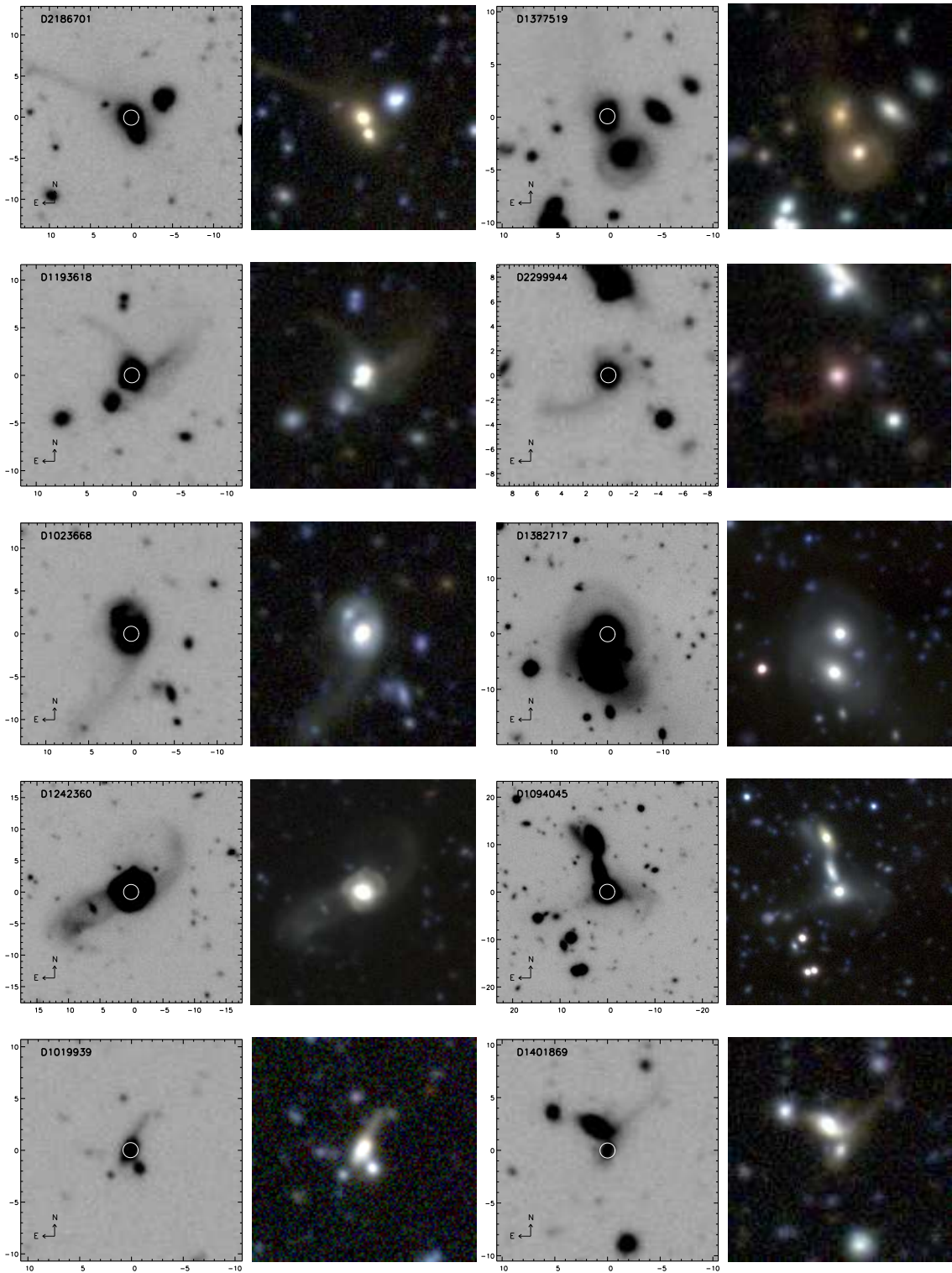
Table 5.3: Fractional Breakdown of Tidal Tail Properties

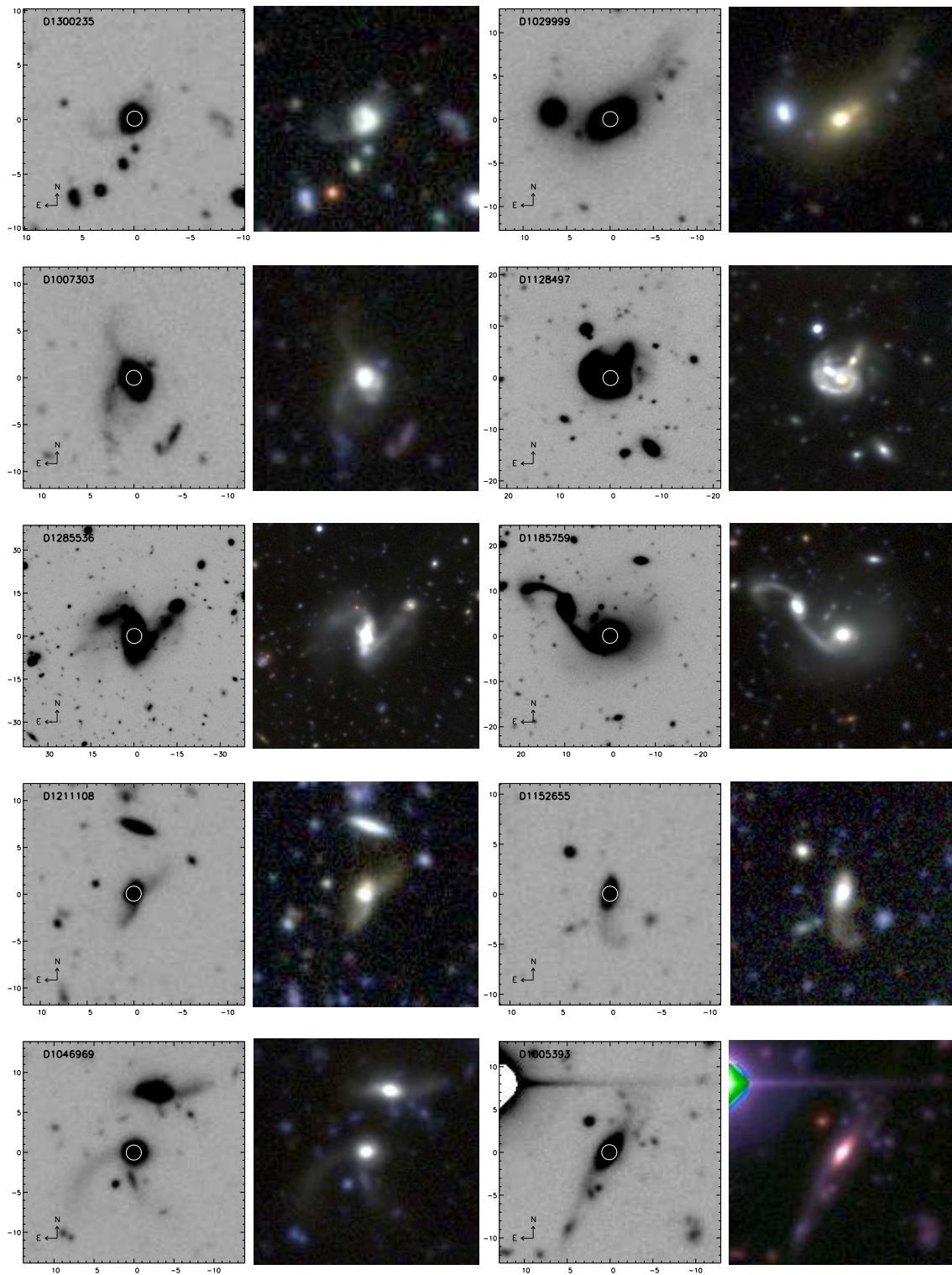
Code	General Description	Fraction within Class
	"Medium Tidal Tails": Tail Length \sim Diameter of Host	Total:456
61	1 tail	64% (293)
62	2 tails	24% (111)
63	> 2 tails	3% (13)
64	Bunny Ears (2 tails)	6% (27)
65	Bunny Ears (>2 tails)	3% (12)
	"Long Tidal Tails": Tail Length > Diameter of Host	Total:376
71	1 tail	42% (157)
72	2 tails	36% (136)
73	> 2 tails	4% (15)
74	Bunny Ears (2 tails)	13% (47)
75	Bunny Ears (>2 tails)	5% (21)
	Close Galaxy-Galaxy Pairs with Tidal Bridges	Total:633
81	Bridge no tail, disk dominated	46% (292)
82	Bridge no tail, bulge dominated	31% (194)
85	Bridge + short tidal tail	8% (48)
861	Bridge + medium tail: 1 tail	7% (47)
862	Bridge + medium tail: 2 tails	0.3% (2)
863	Bridge + medium tail: > 2 tails	0% (0)
864	Bridge + medium tail: Bunny Ears (2 tails)	0% (0)
865	Bridge + medium tail: Bunny Ears (>2 tails)	0% (0)
871	Bridge + long tail: 1 tail	7% (44)
872	Bridge + long tail: 2 tails	0.5% (3)
873	Bridge + long tail: > 2 tails	0% (0)
874	Bridge + long tail: Bunny Ears (2 tails)	0.16% (1)
875	Bridge + long tail: Bunny Ears (>2 tails)	0.3% (2)
	Double Nuclei	Total:493
10	Double nuclei (DN), no tidal tail	78% (384)
105	DN + short tail(s)	2% (12)
1061	DN + medium tail: 1 tail	6% (29)
1062	DN + medium tail: 2 tails	2% (11)
1063	DN + medium tail: > 2 tails	0.2% (1)
1064	DN + medium tail: Bunny Ears (2 tails)	0.8% (4)
1065	DN + medium tail: Bunny Ears (>2 tails)	0.4% (2)
1071	DN + long tail: 1 tail	6% (28)
1072	DN + long tail: 2 tails	4% (19)
1073	Dn + long tail: > 2 tails	0.2% (1)
1074	Dn + long tail: Bunny Ears (2 tails)	2% (12)
1075	Dn + long tail: Bunny Ears (>2 tails)	0.4% (2)

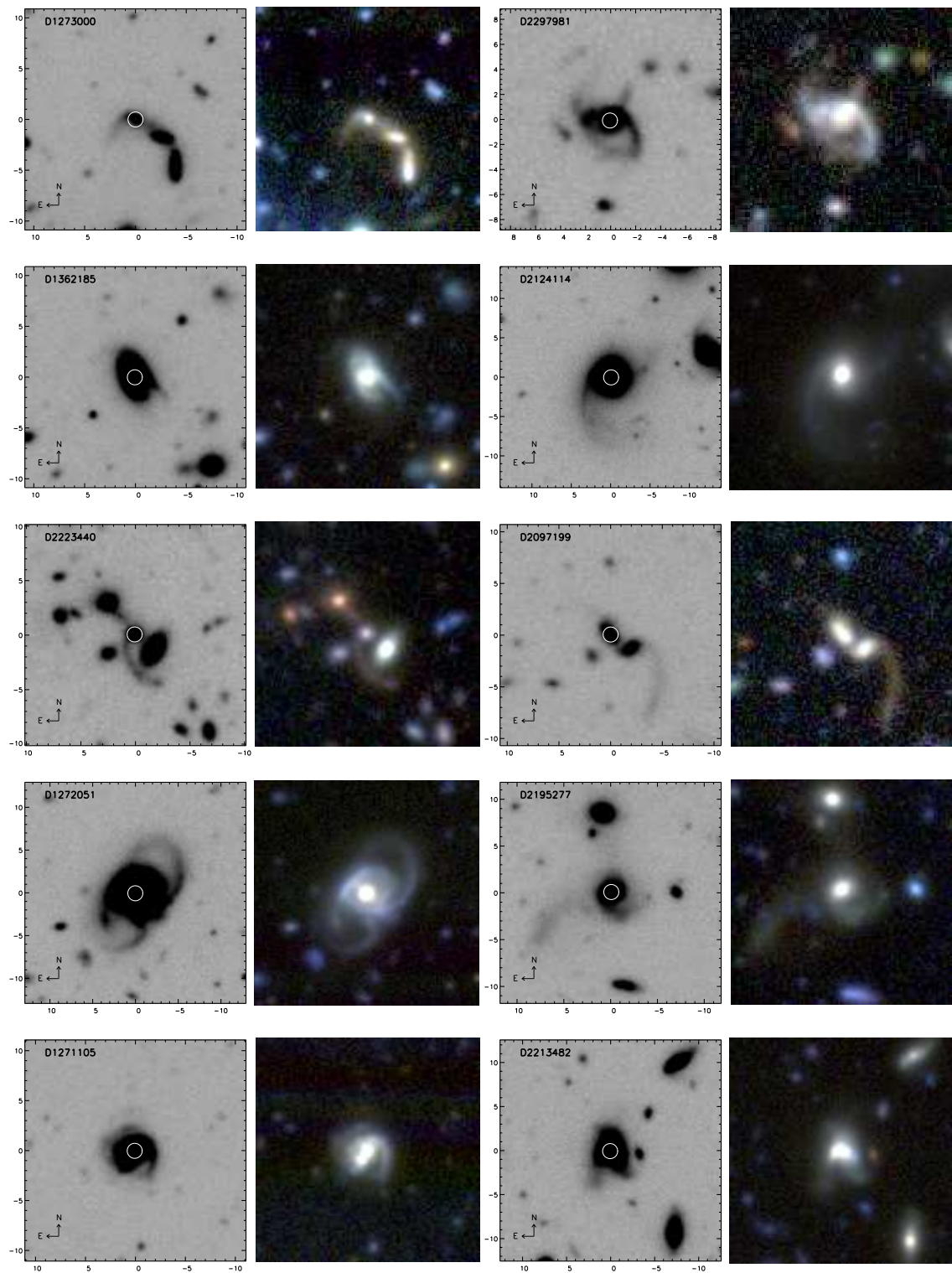
Note: The "fraction within Class" column describes the fraction a particular subclass makes up within its primary class. For example, 42% of long tailed galaxies have only one tidal tail. The value in parentheses is the raw number for the respective subclass.

Figure 5.5: A mosaic of images representing the CFHTLS-Deep Catalog of Interacting Galaxies









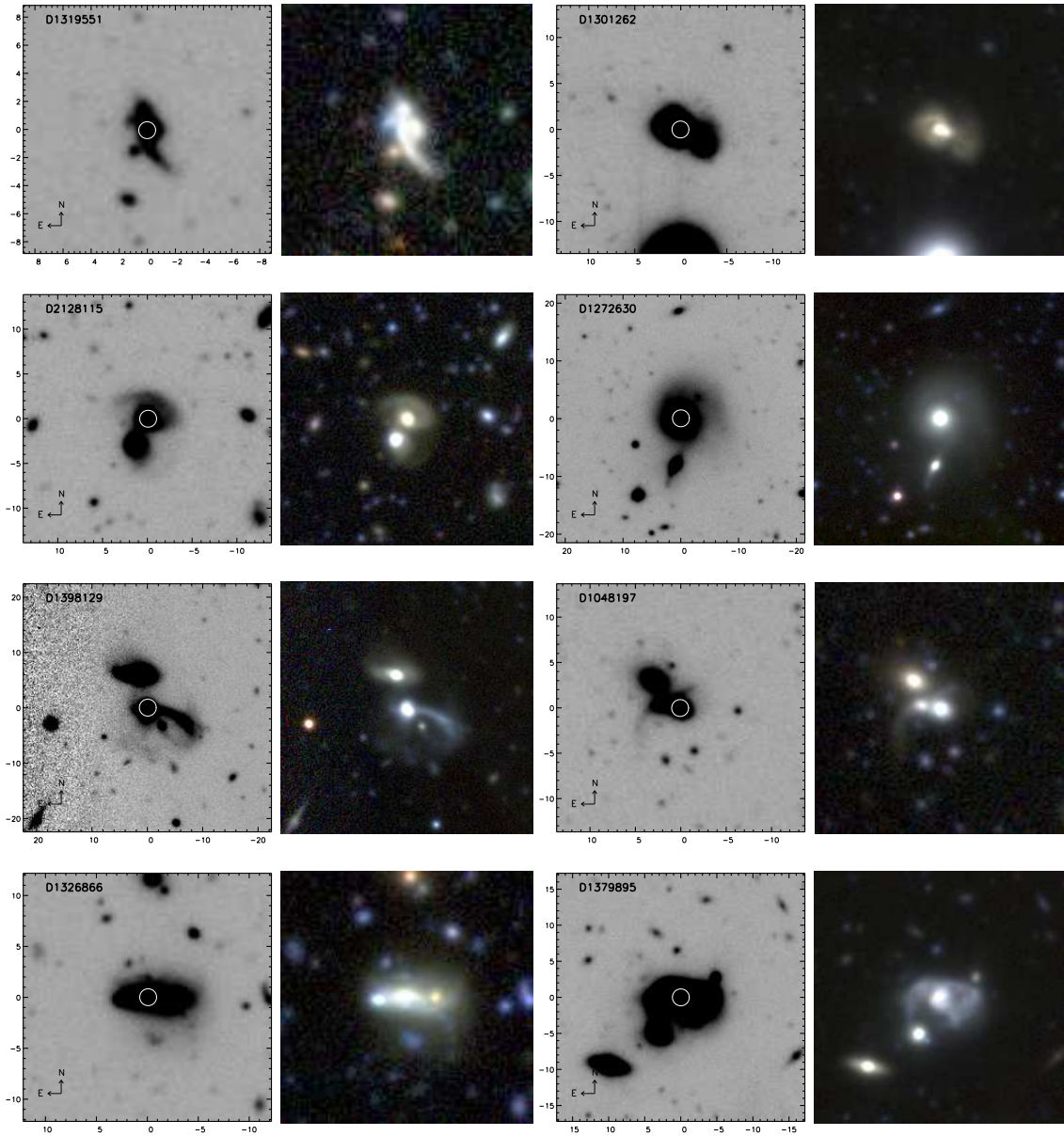


Figure 5.6 A mosaic of images representing the CFHTLS-Deep Catalog of Interacting Galaxies (only $\sim 3\%$ are shown). These i' -band images (left) and color composites (g', r', i') range in class from galaxies with intermediate length tidal tails, long tails, close pairs with tidal bridges to double nuclei with tidal tails. Each stamp is $100 h^{-1}\text{kpc}$ on a side. The white circle marks the galaxy that has been classified, while the axes are in arcseconds. The mean i' magnitude and redshift of the images presented are ~ 19 and $z = 0.41$

5.3 A Classification Experiment

A potential bias in using a visual classification technique is its reproducibility when other individuals visually inspect the same sample of galaxies. A key criteria of this work however, was the requirement of strong tidal signatures before a galaxy was deemed “interacting”. This strong requirement dramatically reduces the classification variance by different individuals. To test and validate the classifications made by C. Bridge, both Dr. Bundy (KB) and Dr. Sullivan (MS) at the University of Toronto, visually inspected a sample of 700 (MS complete 450/700) galaxies. This sample of galaxies was randomly selected from four parent classifications (490-galaxies with tidal tails, 110 galaxies with a tidal bridge, and 100 galaxies classified as possibly interacting but with a lower confidence level (classification code 9).

Both KB and MS were given no information regarding the class breakdown of the set of galaxies they were classifying. The classification was performed in the same manner as described in section 5.2.2, using a simplified coding system outlined in Table 5.4 and discussed prior to the experiment to ensure a consistent approach by all parties. KB and MS noted all classifications relevant to each galaxy. Of the galaxies used in the classification experiment 86% had been confidently categorized as “interacting” prior to the experiment (by C.Bridge). Both KB and MS also classified 88% and 87% of the galaxies in the experiment to be “interacting”. The strong agreement between different individuals regarding which galaxies are “interacting” is a result of the robust visual criteria a galaxy must exhibit before it is included in our analysis. We are therefore excluding many potentially interacting systems (see classes 9,10,5, and 24) not to mention galaxies whose tidal features are below the sensitivities of our survey, hence the results that follow are lower limits.

As an additional test, a set of 500 galaxies (350 interacting, 150 non-interacting) randomly ordered were reclassified by C.Bridge. This blind self test addresses the reproducibility of the authors own classifications using the coding system outlined in Table 5.4. The classifications remained the same 97% of the time. The 3% variation was primarily a result of galaxies being classed into morphologically similar types (i.e an intermediate tidal tailed galaxy being classed as having a short tidal tail) and not into grossly different types.

5.4 Recovery Rate at Higher Redshift

As we are interested in exploring how the fraction of interacting galaxies changes from low- z to high- z , it is important to investigate how tidal features become less resolved and fainter due to cosmological effects. To address this question we have artificially redshifted bright nearby galaxies with tidal features in our sample out to higher redshifts. We then reclassify the

Table 5.4: Classification Experiment: Codings and Descriptions used in the Classification Experiment

Code	General Description
0	Unknown
1	No Tidal Tail
2	Tidal Tail < diameter of galaxy
3	Tidal Tail \sim diameter of galaxy
4	Tidal Tail > diameter of galaxy
5	Galaxy Pair with a Bridge
6	Galaxy Pair with a Bridge and Tidal Tail
7	Double Nuclei with Tidal Tail
8	Double Nuclei without Tidal Tail
9	Disturbed
10	Bunny Ear Tidal Tails

redshifted galaxies to determine the redshift where the tidal features are no longer identifiable as such.

5.4.1 Method

When simulating an image of a low redshift (z_0) galaxy to how it would appear at a higher redshift (z_z), multiple factors must be considered. First, we consider the rebinning factor, b , which is the reduction in apparent size of the galaxy's image when it's viewed at higher redshift. The factor (b) that a galaxy imaged at z_0 needs to be rebinned by to simulate at galaxy at z_z is written as

$$b = \frac{n_0}{n_z} = \frac{\theta_z s_z}{\theta_0 s_0} \quad (5.1)$$

where n_z is the number of pixels in the image, as imaged at redshift z , while s_z and s_0 are the pixel size ($0.186''/\text{pixel}$). In our case we are not simulating what the image would look like using a different detector so s_z and s_0 are the same value and cancel out in the above equation (this parameter was included for clarity). Hence the rebinning factor is simply the ratio of the angles subtended by the image at the initial and higher redshift, where

$$\theta_z = \frac{d}{D_{Az}} = d \frac{(1 + z_z)^2}{L_z} \quad (5.2)$$

and D_{Az} is the angular diameter distance, which is related to the luminosity distance (L_z) by $D_{Az} = L_z/(1 + z)^2$.

The image was rebinned using the idl routine FREBIN which shrinks the array by the designated amount using interpolation. Flux is conversed by ensuring that each input pixel is equally represented in the output array.

We also need to consider the strong dependence of the surface brightness (SB) with redshift as $SB \propto (1+z)^{-4}$, as well as k -correction effects. In order to accurately simulate the appearances of galaxies at high redshift we carefully selected the lowest redshift galaxies possible with similar luminosities to those probed at the high redshift end of our data ($z \sim 0.7 - 1.0$). Our resultant sample consisted of 54 galaxies with tidal features between $0.3 \leq z \leq 0.45$ and $M_g \leq -21.0$.

At redshifts between $0.4 \leq z \leq 1.0$, i' -band is probing rest frame g' -band ($z \geq 0.9$ begins to push into the u^* -band). To account for the effects of the k -correction we utilized the r' -band images of our sample of galaxies being artificially redshifted, since they are between $0.3 \leq z \leq 0.45$, where the r' -band is probing rest g' , like that of our high redshift sample.

Ideally, one would use the segmentation map to define which pixels belong to a particular galaxy and which are associated with the background sky, and only dim the pixels that make up the objects. However, in our case the features of interest, such as tidal tails can be low surface brightness and diffuse, and therefore sometimes not extracted correctly. This was illustrated earlier in Figure 5.2. To address this we reduced the surface brightness of the entire image. In doing so we also reduce the noise of the image, so to correct for this we add the appropriate amount of noise back into the image at the end of the simulation process, which is discussed in detail later.

The luminosity of the same galaxy at low and high redshift should be the identical due to the laws of conservation of energy. Therefore, the amount the image must be reduced in surface brightness is computed by equating the absolute i' and r' magnitudes of each pixel, and can be written as,

$$flux_i = (flux_r \left(\frac{(1+z_1)^4 D_{A1}^2}{(1+z_2)^4 D_{A2}^2} \right) 10^{0.4[ZP_i - ZP_r]} (1+z_2)^Q) \quad (5.3)$$

where ZP are the zeropoints for the i' and r' -bands, z_1 is the redshift of the galaxy, while z_2 is the redshift that the galaxy is being shifted to. The factor of $(1+z_2)^Q$ can be included to address potential surface brightness evolution. Meaning, although a galaxy's surface brightness falls off due to cosmological dimming, galaxies at higher redshift are thought to have higher surface brightnesses, which in turn partially counteracts the dimming effect. The simulations were run both assuming a surface brightness evolution of $Q = 1.4$ (Lilly et al. 1998) and without the effects of the surface brightness evolution ($Q = 0$) (Figure 5.6).

To account for the fact that each pixel in the image is dimmed instead of just the pixels associated with the galaxy, the appropriate amount of noise was added back into the image. The noise was computed using,

$$rms_{added} = \sqrt{rms_{original}^2 - rms_{rescaled}^2} \quad (5.4)$$

where the $rms_{rescaled}$ is the noise in the rebinned, and dimmed image. The $rms_{original}$ was derived by averaging numerous sections of the full square degree image that were unoccupied by sources to properly probe the sky values. The individual stamps of the galaxies were not used in the rms determination again due to the ambiguity of the segmentation maps.

5.4.2 Recovery Rate Results

The sample of 54 low redshift galaxies described above were redshifted out to 5 different redshifts, $z = 0.55, 0.70, 0.85, 1.0, 1.15$. The galaxies were re-inspected at each interval for the presence of tidal features. Figure 5.6 shows, as expected, that as the redshift increased the ease in which tidal features can be detected decreases due to the cosmological dimming and rescaling. Although, when surface brightness evolution was included $\sim 4\%$ more galaxies with tidal features were recovered. The recovery rate remains high out to $z \sim 0.85$, where we can still identify strong tidal features in $\sim 80\%$ of the redshifted galaxies (70% when no surface brightness evolution was included). This simulation suggests that although SB evolution does aid slightly ($< 5\%$ effect) in counter acting cosmological dimming, the increase in the interaction fraction is not a result of the tidal features' SB being higher at higher redshift, and in turn more easily detectable.

Throughout the analysis discussed in this chapter the recovery rate is also referred to as a completeness limit, as it quantifies our survey's sensitivity to tidal features. The rate of recovery could be used as a correction factor, however we are currently most interested in a lower limit measurement of the evolution of the interaction fraction.

5.5 The Galaxy Interaction Fraction: Sample Descriptions

In the past three decades the concept of galaxies as “island Universes” slowly evolving in isolation has changed dramatically. Gravitational interaction between galaxies is now considered a relevant factor in a galaxy’s evolution, capable of altering its morphology, luminosity, colour, size, SFR, and mass distribution.

Tidal tails and bridges are a result of gravitational encounters between two or more galaxies (e.g. Toomre & Toomre 1972). The statistics of galaxies with extended tidal features (tidal bridges and tails) is a powerful tool to study the evolution of the galaxy interaction fraction (GIF). In this section we present our analysis of the GIF using the CFHTLS-Deep survey.

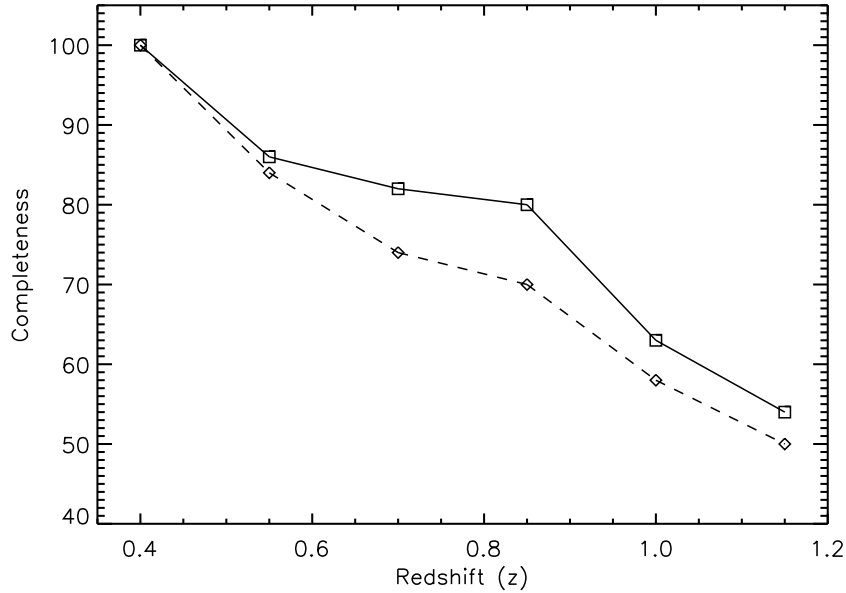


Figure 5.6: The recovery rate for the artificially redshifted sample of 54 interacting galaxies. The full sample of interacting galaxies can be considered 80% complete at $z \sim 0.85$ assuming SB evolution, or 70% complete assuming no surface brightness enhancement at higher redshift. Meaning we are able to detect 80% of the tidal features like those seen at lower redshift ($z \sim 0.4$) out to $z \sim 0.85$, and 62% at $z \sim 1.0$.

5.5.1 Defining the Interacting and Non-Interacting Samples

We first utilize our previously described morphological classifications to divide our sample into “interacting” and “non-interacting” galaxies. Recall that we define “interacting” or “merging” galaxies to have the following visual classifications: medium tidal tails (61-65), long tidal tails (71-75), galaxies in a close pair linked with a tidal bridge (81,82,85,861-871), and those with a clear double nuclei and a tidal tail (105,1061-1071). We confidently find a total of 1586 interacting galaxies within the D1 and D2 fields combined.

In order to investigate the properties of interacting and merging galaxies, we also need to establish a comparison sample of non-interacting galaxies. We combine all the non-interacting classifications which are primarily composed of spiral or disk dominated sources to construct a fair comparison sample. We have identified 22,268 non-interacting galaxies. Before proceeding with the GIF measurement we must first verify that the redshift distributions of the interacting and non-interacting galaxy samples are comparable.

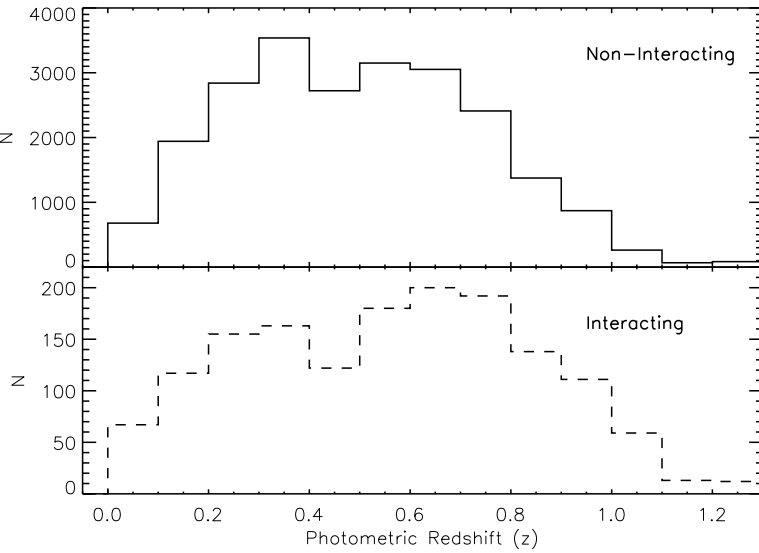


Figure 5.7: The redshift distribution for all galaxies classified as non-interacting (upper) and interacting (lower, dashed). The mean photometric redshifts for the two samples are 0.51 (non-interacting), and 0.58 (interacting).

5.5.2 Redshift Distribution

We applied a traditional template fitting technique as described in section 4.3.1 to acquire photometric redshift estimates for each of our sources. The redshift distribution for both the interacting and non-interacting populations (Figure 5.7) is found to be highly similar, allowing us to proceed with our investigation of the GIF. The mean redshift for the interacting population is 0.58, and 0.51 for the non-interacting sample. For the following analysis we have imposed an upper redshift limit of 1.2, due in combination to the lack of sources at redshifts > 1.2 (caused by the apparent magnitude limit), and the fact that the 4000Å break begins to move beyond our bluest filter, reducing the accuracy of the photometric redshifts.

5.6 The Galaxy Interaction Fraction (GIF)

Unlike close pair studies which suffer from projections effects, using the number of galaxies exhibiting strong tidally induced structures like tails and bridges is a relatively simple and robust measure of the interaction fraction. The CFHTLS-Deep survey is sensitive to tidal features with surface brightnesses down to $i' \lesssim 28 \text{ mag/arcsecond}^2$. Our approach is simply to compare the number of galaxies with tidal features (N_{INT}), to the total number of galaxies

Table 5.5: Inferred Galaxy Interaction Statistics as a Function of Interaction Type

Class	Redshift Range						
	0.10-0.25	0.25-0.40	0.40-0.55	0.55-0.70	0.70-0.85	0.85-1.0	1.0-1.15
N_{Total}	3715	5185	5062	4880	3432	1502	276
Short	N_{INT}	26	76	102	112	71	-
Tidal Tails	GIF [%]	0.7 ± 0.1	1.5 ± 0.2	2.0 ± 0.2	2.3 ± 0.2	2.1 ± 0.3	-
Medium	N_{INT}	23	39	59	84	74	62
Tidal Tails	GIF [%]	0.6 ± 0.1	0.8 ± 0.1	1.2 ± 0.2	1.7 ± 0.2	2.2 ± 0.3	4.1 ± 0.5
Long	N_{INT}	38	62	46	56	50	33
Tidal Tails	GIF [%]	1.0 ± 0.2	1.2 ± 0.2	0.9 ± 0.1	1.2 ± 0.2	1.5 ± 0.2	2.2 ± 0.4
Close Pair	N_{INT}	44	54	91	122	106	57
+Bridge/Tail	GIF [%]	1.2 ± 0.2	1.0 ± 0.1	1.8 ± 0.2	2.5 ± 0.2	3.1 ± 0.3	3.8 ± 0.5
Double Nuclei	N_{INT}	2	5	9	11	20	12
+ Tail	GIF [%]	0.05 ± 0.04	0.1 ± 0.04	0.2 ± 0.1	0.2 ± 0.1	0.6 ± 0.1	0.8 ± 0.2
Double Nuclei	N_{INT}	8	29	53	82	87	48
No Tail	GIF [%]	0.2 ± 0.1	0.6 ± 0.1	1.1 ± 0.1	1.7 ± 0.2	2.5 ± 0.3	3.2 ± 0.5
							5.4 ± 1.4

Note: A stellar mass limit of $10^{9.5}(M_\odot)$ has been imposed. All errors bars are derived from counting statistics

within the same absolute magnitude or stellar mass ranges (N_{Total}), as a function of redshift (see equation 5.5).

$$\text{Galaxy Interaction Fraction(GIF)} = \frac{N_{INT}}{N_{Total}} \quad (5.5)$$

5.6.1 Galaxy Interaction Fraction: Interaction Class

This section describes the redshift evolution of the interaction fraction for the various classes of interacting galaxies. This allows us to explore how the frequency of different interaction types or stages have evolved over time. Table 5.5 outlines the GIF statistics and Figure 5.8 illustrates the GIF for the different interacting types. The sample was restricted to be brighter than $i' \leq 21.9$ to ensure confident classifications, and to have stellar masses $\log M_*(M_\odot) \geq 9.5$ so we are probing similar mass galaxies at low and high redshift. The details of the stellar mass distribution and limits imposed on the sample are discussed later in section 5.7.7.

There is clear evidence that all interacting galaxy classes show at least some evidence of evolution with redshift. The most strongly evolving interacting classes are galaxies in a close pair with a tidal bridge, and galaxies with medium length tidal tails, with interaction fractions 3 times higher at $z \sim 0.9$ than at lower redshifts ($z \sim 0.2$).

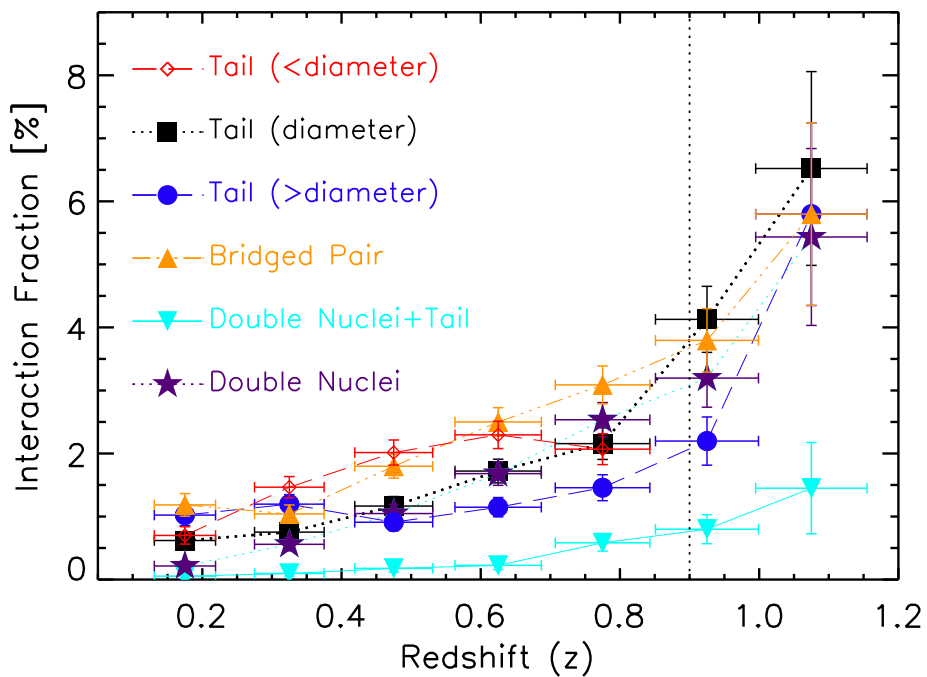


Figure 5.8: The galaxy interaction fraction as a function of redshift for different interaction classes. Short tidal tails are shown in diamonds (red), medium tails squares (black), long tails circles (blue), bridged close pairs upward triangle (orange), galaxies with a double nuclei and a tidal tail downward triangle (green), and double nuclei with no tail star (violet). The error bars are derived using poisson statistics, while the horizontal errors come from the uncertainty in the photometric redshift. The vertical dotted line represents the 75% completeness limit. A stellar mass limit of $10^{9.5}(M_\odot)$ has been imposed.

5.7 Primary Galaxy Interaction Fraction

In the previous section we explored the contribution from the various types or stages of interacting galaxies to the GIF. In this section, we combine the different interacting classes and present one of the primary goals of this research, which is the overall galaxy interaction fraction as a function of redshift. Once again the sample consists of all galaxies with an apparent magnitude brighter than $i' \geq 21.9$, and having a stellar mass larger than $10^{9.5} (M_\odot)$. To ensure a confident lower limit for the GIF we have only considered interacting galaxies with a secure classification. As previously described, the interaction classes included in this measurement are “medium” and “long” tidal tailed galaxies, those in a close galaxy pair with a tidal bridge, and those with a double nuclei and addition morphological evidence of an interaction such as a tidal or bridge. The total number of interacting galaxies used in measuring the GIF was 1,240. Galaxies with “short” tidal tails, and those with double nuclei and no other tidal features were not considered. Although the probability they are undergoing an interaction is favorable, only highly confident interactions were included, as our goal is a secure lower limit of the interaction fraction.

5.7.1 Evolution of the Interaction Fraction

The total GIF, illustrated in Figure 5.9 and numerically described in Table 5.6 reveals a rising fraction of galaxies involved in an interaction or merger with redshift. Meaning, more galaxies were undergoing a tidal interaction when the Universe was about half it’s current age. At low redshift ($z \sim 0.3$) the GIF was found to be $\sim 4\% \pm 0.3$ and more than doubles by $z \sim 0.95$ to $11\% \pm 0.9$. We characterize the evolution of the galaxy interaction fraction by fitting a simple power-law increase with redshift (also applied in Chapter 3 section 3.6.1) of the form $GIF = GIF_0(1 + z)^m$, where GIF_0 is the present day interaction fraction, and m is the power-law index. When all redshift bins in our sample are included ($0.1 \leq z \leq 1.15$) we find a best fit m of 2.24 ± 0.24 and GIF_0 of $2.15\% \pm 0.25$, weighted by the GIF errors bars in each redshift bin.

As discussed in the next section there may be some potential biases at the low and high redshift ends of our analysis. Therefore the evolution of the GIF was also fit using various redshift ranges as shown in Figure 5.9. If one excludes the lowest redshift bin ($0.1 - 0.25$) a best fit power-law index of $m = 2.80 \pm 0.25$ is derived. If the highest redshift bin $1.0 - 1.15$ (the least confident) is excluded $m = 1.95 \pm 0.25$, the lowest degree of evolution found in our analysis. Lastly, if both the lowest and highest redshift bins are removed a value for m of 2.56 ± 0.24 is derived. It is clear that even assuming the minimum value of m found in this analysis, models suggestive of little evolution of the GIF ($m < 1.0$) with redshift are ruled out at a $> 2\sigma$ level of confidence.

5.7.2 Potential Biases

The interaction fraction for the lowest redshift point ($z = 0.18$) is heightened compared to the GIF between $0.25 \leq z \leq 0.6$, potentially due to the fact that at low redshift, tidal features are more easily detected due to the larger angular size of galaxies.

At higher redshift, although our detectability drops as shown in section 5.4 due to simple redshift effects, we still find a large and increasing GIF out to $z \sim 1$. Since we have selected our sample based on a galaxy's stellar mass we do not suffer from a common bias that has affected many close pair and merger fractions which imposed a luminosity limit. If a galaxy is undergoing a tidal interaction star formation can be triggered, elevating a galaxy's luminosity and hence boosting it into a survey's sensitivities, biasing the close pair or merger statistics to higher values. The PEGASE code used to derive our stellar mass uses a 2 population model to account for new and old stellar populations, hence enhanced star formation has no effect on a galaxy's derived stellar mass.

One potential bias to consider is that as we probe higher redshifts, $z > 0.9$, we begin to more closely probe the UV (u^* band) which is dominated by massive young O and B stars. Therefore, star formation in tidal tails and bridges may be more easily visible resulting in a higher GIF at larger redshifts. However, it is unlikely that this bias is solely or even largely responsible for the higher GIF at $z \sim 1$, since the simulations performed in section 5.4 revealed that an enhancement in surface brightness only effects the recovery rate on a $\sim 5\%$ level. This would in turn only affect the GIF by $< 1\%$.

Another bias to consider involves the strong Mid-IR luminosity dependence on the fraction of galaxies undergoing an interaction (see section 5.10.3). At redshifts beyond $z \geq 0.9$ galaxies detected at $24\mu\text{m}$ are high luminosity LIRGs or ULIRGs, which we find to be interacting more frequently (Figure 5.23). Therefore, the dramatic elevation of the GIF could in part be attributed to probing higher Mid-IR luminosity systems. Although it should be noted that Mid-IR faint galaxies also show an increasing GIF with redshift (Figure 5.24) consistent with the overall trend seen in Figure 5.9. Also there is evidence for evolution in the GIF with the highest redshift point removed. A deeper $24\mu\text{m}$ survey would allow us to better probe the Mid-IR luminosity effect on the GIF at $z > 0.9$. This can be done using the MID-IR coverage of the CFHTLS-D2 from the COSMOS survey once the data is made public.

Our analysis therefore suggests that the evolution in the GIF is a real physical effect, meaning there were more galaxies undergoing tidal interactions and mergers at earlier times out to $z \sim 1$. Unlike previous studies probing close pair and merger fractions, small number statistics do not effect the confidence of our results, as we have the largest sample of interacting galaxies in the current literature, with sub-percent poisson errors. Although our sample is the largest

Table 5.6: Inferred Galaxy Interaction Statistics

Redshift	N_{Int}	N_{Total}	Int. Fraction [%]
0.10-0.25	108	1745	6.2±0.6
0.25-0.40	160	3725	4.3±0.3
0.40-0.55	209	4736	4.4±0.3
0.55-0.70	280	4700	6.0±0.4
0.70-0.85	258	3413	7.6±0.5
0.85-1.00	168	1497	11.2±0.9
1.00-1.15	57	300	19.0±2.5

to date by a factor of >10 it remains important to compare our findings to previous works.

5.7.3 GIF: Comparison with Previous Works

We begin with Reshetnikov (2000), which used a similar visual classification approach to identify tailed galaxies, and found a local interaction fraction on the order of 1-2%, compared to the 5% local measurement found by this work. Possible explanations as to why our local measurement is higher than that found in Reshetnikov (2000), are 1) the CFHTLS-Deep images are better suited to detecting low surface brightness features, because of their depth, 2) the large survey area (2 square degrees) provides a larger sample of galaxies. Reshetnikov (2000) only had a sample of 14 interacting galaxies between 0.5-1.5, and may have been affected by small number statistics and cosmic variance.

A key consideration when attempting to compare results from previous studies is the similarity in objects being probed. It is unfair to directly compare our results to those which derive a close galaxy pair fraction as they have included pre-merger pairs (prior to the first passage) and we have not. Since we use a morphological approach in identifying interactions a fairer comparison would be studies that also consider the visual appearance of a galaxy whether it be qualitative or quantitative, like those of Le Fèvre et al. (2000) and Conselice et al. (2003) to name a couple. Another key consideration are the limits imposed on the sample, i.e. luminosity or stellar mass restrictions. Many studies of this kind have been restricted to probing merger rates with luminosity limits imposed. Therefore a fair comparison with our results (at this time) can only be made to work done by Conselice et al. (2003), who probe the merger fraction as a function of stellar mass. Figure 5.10 re-illustrates the GIF found by the CFHTLS-Deep survey, and includes results reported by Conselice et al. (2003) (shown in orange triangles). Our results are consistent with that found by Conselice et al. (2003). It should be noted that their measurements of the merger fraction were based on a sample inspecting only 27 galaxies between $0.4 < z < 0.7$ and 61 within $0.7 < z < 1.3$, while in the same redshift ranges we are probing 5,206 and $>5,210$ galaxies.

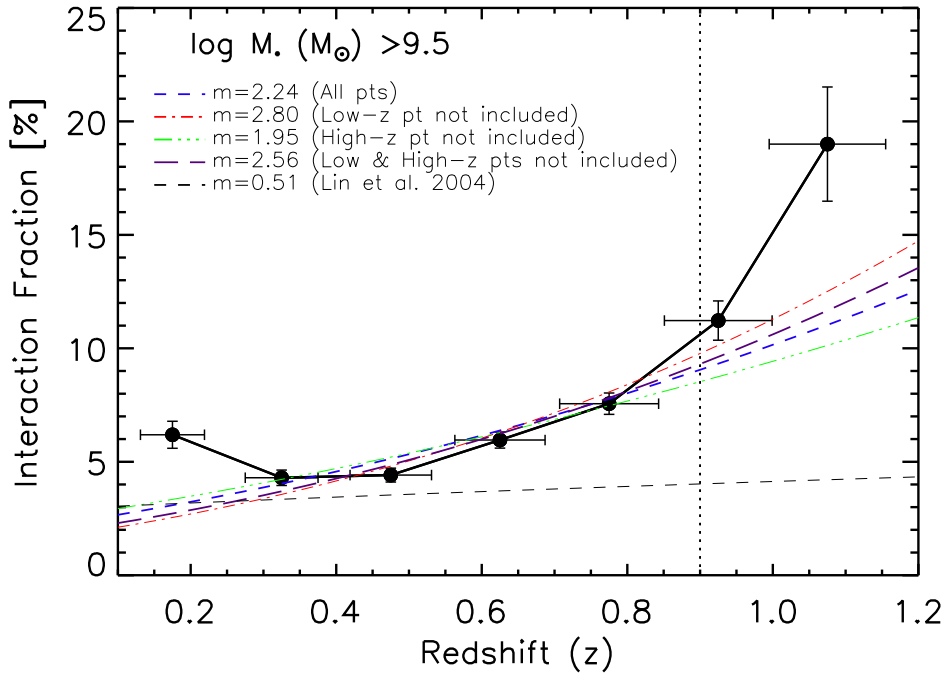


Figure 5.9: The mass limited galaxy interaction fraction as a function of redshift from the CFHTLS-Deep survey (filled circles). The non-solid lines represent the best $(1+z)^m$ fits when various data points are included in the analysis. When all points between $0.1 \leq z \leq 1.15$ (with stellar masses $\geq 10^{9.5}(M_\odot)$) are included the best fit of $(1+z)^m$ is $m = 2.24 \pm 0.24$ (blue, dashed). When the lowest redshift point is not included, $m = 2.8 \pm 0.25$ (red, dash-dot), only the high-z point removed, $m = 1.95 \pm 0.2$ (green, dash-dot-dot), and when both the low and high-z points are not included $m = 2.56 \pm 0.24$ (purple, long dash). It is clear that a GIF with little evolution as found in Lin et al. (2004); Lotz et al. (2006) ($m = 0.51 \pm 0.28$, black dashed line) is inconsistent with our results, and can be ruled out at a $> 2\sigma$ level. The error bars are derived using poisson statistics, while the horizontal errors come from the uncertainty in the photometric redshift. The vertical dotted line represents the 75% recovery limit.

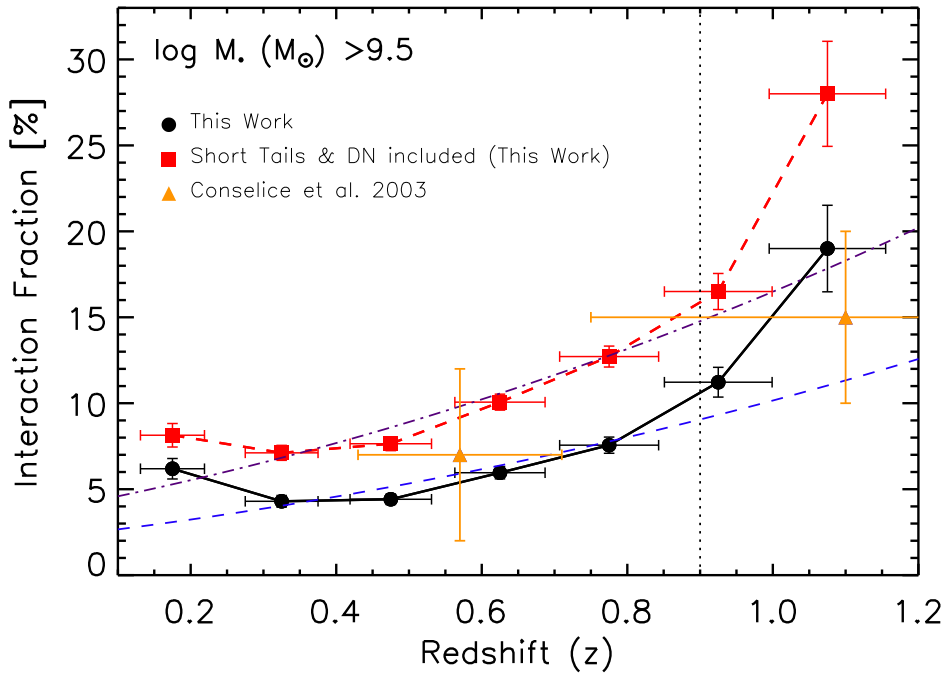


Figure 5.10: A plot of the mass limited GIF as a function of redshift from the CFHTLS-Deep survey using the primary interacting sample (circles; black) and the secondary sample (squares; red) that include “short” tidal tails, and double nuclei with no other interaction signatures. The filled triangles (orange) are merger fractions derived in Conselice et al. (2003). The blue dashed line outlines the best $m = 2.24 \pm 0.24$ fit for the primary sample, while the secondary sample has an $m = 2.14 \pm 0.18$. Again, error bars are derived using poisson statistics, while the horizontal errors come from the uncertainty in the photometric redshift. The vertical dotted line represents the 75% recovery limit.

This work has presented the first statistically secure lower limit of the interaction fraction for galaxies with stellar masses $M_* > 10^{9.5}$ as a function of redshift. The fraction of galaxies undergoing tidal interactions is surely higher than the rate reported in this work, as this study is limited to higher surface brightness features, and only included the most confident tidal features in its analysis.

In Figure 5.10 we re-derived the GIF with the inclusion of less confident signatures of tidal interactions or mergers, such as galaxies with “short” tidal tails (tail length less than diameter of host), and galaxies with a double nuclei and no secondary signs of an interaction. This resulted in an additional 767 “interacting” galaxies included in the analysis. The resultant GIF is on average $\sim 5\%$ higher than our lower limit, and its evolution with redshift traces the lower limit GIF remarkably well over the full redshift range.

5.7.4 Interaction Fraction: Luminosity Dependence

After estimating a confident lower limit for the galaxy interaction fraction we now explore the sensitivity of the results to various galaxy properties, beginning with optical luminosity. Many previous merger rate studies have found the merger rate to depend on luminosity (Patton et al. 1997, 2000; Conselice et al. 2003; Xu et al. 2004). In the following sections we apply various optical luminosity limits to our sample and re-analyze the GIF to explore any possible luminosity dependence. Figure 5.11 shows the absolute g' -band magnitudes (M_G) for the interacting (red) and non-interacting (black) samples in the combined D1 and D2 fields. It also outlines the M_G limits imposed to aid in a more complete comparison of galaxies at high and low redshifts with and without considering luminosity evolution.

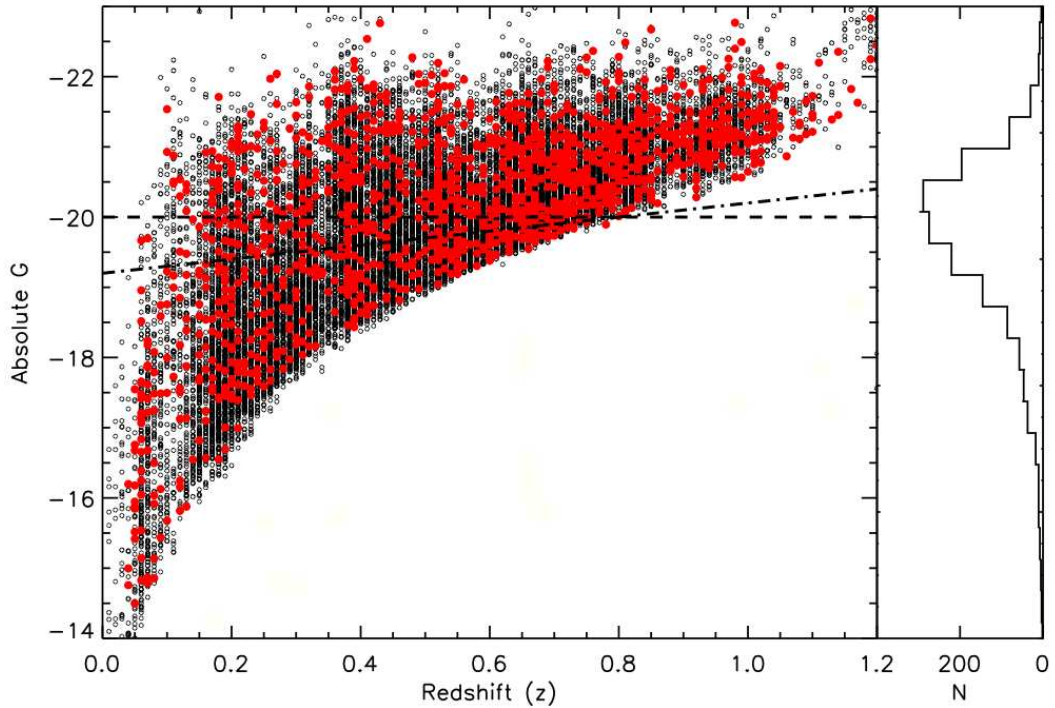


Figure 5.11: The absolute g' -band luminosity as a function of redshift for galaxies classified as non-interacting (open circles, black) and those undergoing an interaction (filled circles, red). The dashed lines define the lower absolute magnitude limits considered in following analysis section; (dashed) no luminosity evolution, (dashed-dotted) includes luminosity evolution $Q = 1$. The histogram on the right shows the absolute g' magnitude distribution for the interacting galaxy sample.

We chose a minimum (M_{min}) luminosity limit, $M_G \leq -20$, which is a few tenths of a magnitude brighter than M^* to balance the completeness at high redshift with probing M^* as closely as possible. The sample was divided into bright ($M_G < -21.0$) and faint ($-21.0 \leq M_G \leq -20.0$) luminosities to study the impact optical luminosity may have on the frequency

of observed galaxy interactions. Table 5.7 and Figure 5.12 present the GIF as a function of redshift for the two luminosity ranges. A clear dependence of the GIF on M_G is evident out to $z \sim 0.7$, after which bright and faint galaxies have statistically similar interaction fractions. Within the optical luminosities outlined above, bright galaxies show tidal signatures more frequently than fainter galaxies. It must be considered however, that this result may be either entirely or in part due to the ease of identifying the low surface brightness features in brighter galaxies, rather than a true increase in the frequency of interactions in brighter galaxies. The level of this effect is difficult to quantify, and requires deeper images of these fainter galaxies to see if tidal features are evident.

Overall, we find that between $0.2 \leq z \leq 0.7$ regardless of the optical luminosity the GIF is fairly constant, consistent with little evolution of the GIF. However, there is evidence of an increasing GIF at $z > 0.8$, suggesting that interactions and merging may play a larger role in galaxy evolution at higher redshifts.

At this point we have assumed that galaxies in the past and those locally have similar optical luminosities. We now proceed with a scenario when luminosity evolution is assumed.

5.7.5 Interaction Fraction: Luminosity Evolution

When a static luminosity limit is considered for a range of redshifts, one is essentially assuming that the mass-to-light ratio (M/L) of galaxies is the same over that redshift range. In this section we explore the impact that luminosity evolution may have on our GIF measurement.

Although there is considerable controversy in the literature as to how galaxies evolve at $z < 1$, it is agreed that evolution does occur (Lin et al. 1999; Carlberg et al. 2001), but at what magnitude is under debate. At the very least galaxies will evolve passively as their stellar populations age, resulting in a gradual fading of their optical light. Hence, at higher redshifts when the galaxies are younger we would expect them to have higher mean luminosities. Detailed luminosity function studies (Lin et al. 1999) showed that a luminosity correction can be applied to a galaxy at redshift z , using the expression, Qz , where Q is typically taken to be equal to 1 (Lin et al. 1999; Patton et al. 2002).

Luminosity evolution has been considered in some close pair studies. Patton et al. (2002) and Lin et al. (2004) found that N_c (the number of companions per galaxy) can be significantly affected by the inclusion or exclusion of luminosity evolution. When luminosity evolution is corrected for, fainter galaxies at lower redshifts are included, resulting in higher pair statistics, and in turn less evolution of the pair fraction with redshift.

To explore the effect luminosity evolution may have on the interaction fraction we have adopted $Q = 1$, and repeated the GIF analysis described in the preceding section. We find no significant difference in the GIF at any redshift with or without a luminosity evolution

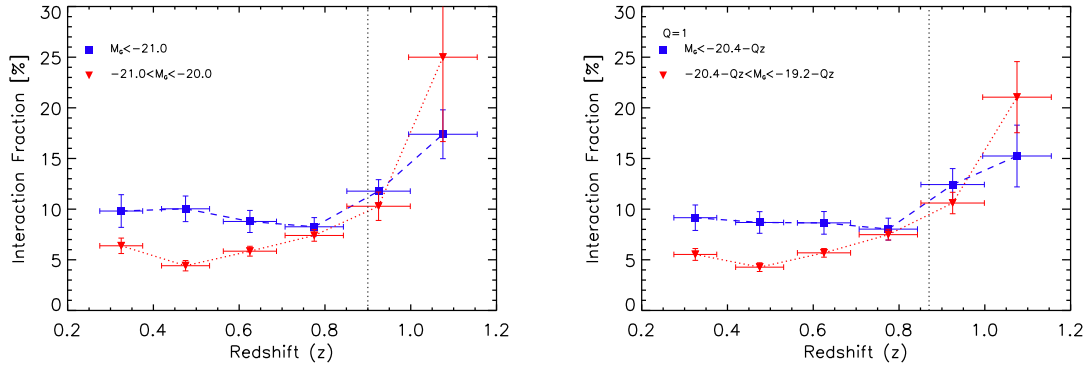


Figure 5.12: The galaxy interaction fraction as a function of redshift. (Left) the GIF assuming no luminosity evolution ($Q=0$). (Right) the GIF assuming luminosity evolution of $Q=1$. It is clear that the GIF is not highly dependent on the assumption of luminosity evolution. At lower redshift ($z < 0.6$) more luminous galaxies have a GIF up to 2 times that of lower luminosity galaxies. The error bars are derived using poisson statistics, while the horizontal errors come from the uncertainty in the photometric redshift. Note that at $z > 1$ the $-21.0 \leq M_G \leq -20.0$ sample is incomplete, and should be considered with caution.

correction (see Table 5.7 for numerical details). Figure 5.12 shows that the GIF is still dependent on optical luminosity at lower redshifts ($z < 0.6$), regardless of luminosity evolution. Bright galaxies, below $z < 0.6$ are up to 2 times more likely to be undergoing an interaction or merger than fainter galaxies. This luminosity dependence is also not evident at higher redshifts ($0.6 < z < 1.0$) when $Q = 1$.

5.7.6 Interaction Induced Brightening?

We might expect that galaxies involved in an interaction may have heightened luminosities compared to non-interacting galaxies, due to tidally triggered star formation or AGN activity. Figure 5.13 shows the M_G distribution for four primary interacting galaxy types. The average M_G magnitude for the field population (not including galaxies classified as interacting) is -20.66. The four interacting types all show an elevated average M_G brightened of 0.15-0.5 mags. compared to the non-interacting population ($M_G=-20.81$ for medium tidal tails, -20.91 for close pairs, -20.96 for long tails, and -21.16 for double nuclei with tidal tails). For comparison minimal elevation is seen in isolated spiral galaxies which have an average M_G of -20.68. However, it is important to consider the masses of these systems, as a larger more massive galaxy is often brighter than a less massive one. For example, galaxies with visual evidence of a double nuclei and tidal tail are potentially more massive systems, compared to an isolated spiral, since they have a high probability of being the result of two galaxies that have recently coalesced. In the next section we probe the mass dependence of the galaxy interaction fraction.

Table 5.7: Galaxy Interaction Statistics: Luminosity Limits

Luminosity Range	Redshift	N_{Total}	N_{Int}	Int. Fraction [%]
No Luminosity Evolution				
$M_G < -21.0$	0.25-0.40	377	37	9.8 ± 1.6
	0.40-0.55	628	63	10.0 ± 1.3
	0.55-0.70	740	65	8.8 ± 1.1
	0.70-0.85	1005	83	8.3 ± 0.9
	0.85-1.00	917	108	11.8 ± 1.1
	1.00-1.15	299	52	17.4 ± 2.4
$-21.0 \leq M_G < -20.0$	0.25-0.40	1097	70	6.4 ± 0.8
	0.40-0.55	1698	75	4.4 ± 0.5
	0.55-0.70	2479	145	5.9 ± 0.5
	0.70-0.85	2283	169	7.4 ± 0.6
	0.85-1.00	525	54	10.3 ± 1.4
	1.00-1.15	36	9	25.0 ± 8.3
Luminosity Evolution ($Q = 1$)				
$M_G < -20.4 - Qz$	0.25-0.40	579	53	9.2 ± 1.3
	0.40-0.55	760	66	8.7 ± 1.1
	0.55-0.70	694	60	8.7 ± 1.1
	0.70-0.85	685	55	8.0 ± 1.1
	0.85-1.00	499	62	12.4 ± 1.6
	1.00-1.15	164	25	15.2 ± 3.1
$-20.4 - Qz \leq M_G < -19.2 - Qz$	0.25-0.40	1628	90	5.5 ± 0.6
	0.40-0.55	2316	99	4.3 ± 0.4
	0.55-0.70	3113	177	5.7 ± 0.4
	0.70-0.85	2660	199	7.5 ± 0.5
	0.85-1.00	943	100	10.6 ± 1.1
	1.00-1.15	171	36	21.1 ± 3.5

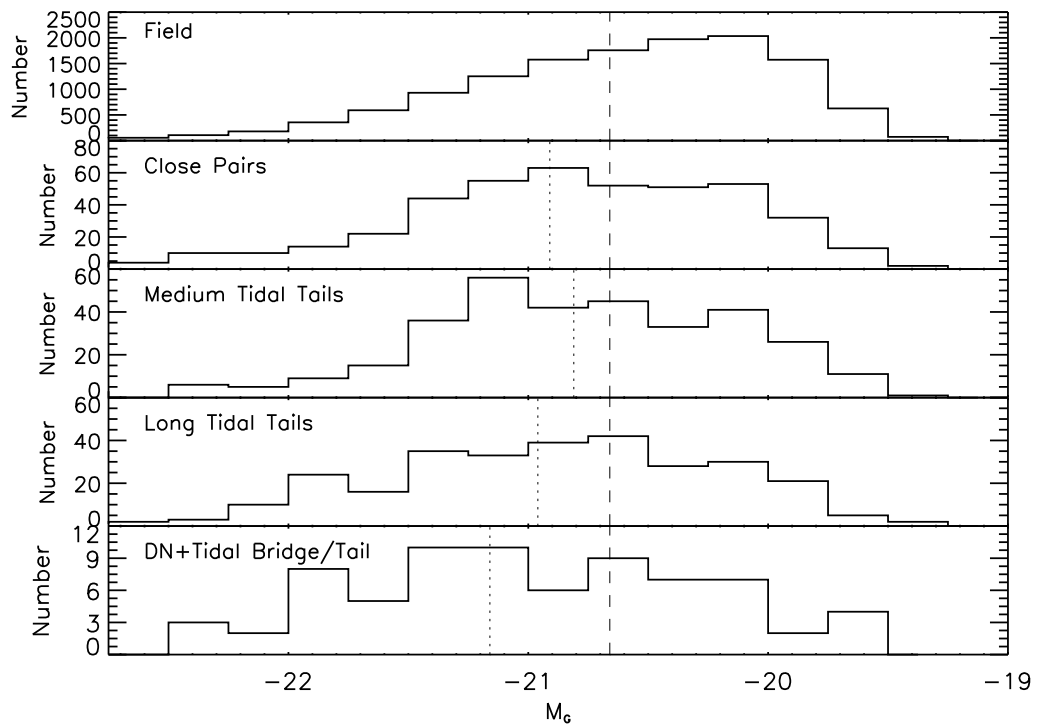


Figure 5.13: The absolute g' -band magnitude (M_G) distribution for galaxies classified as interacting and the field. The dotted line represents the average M_G for each interacting class. (Top) Field galaxies (interacting galaxies removed), (2nd, 3rd, 4th from top) show galaxies in a paired system with a tidal bridge, and galaxies with medium and long length tidal tails, (bottom) are galaxies with a double nuclei and tidal features. The dashed line defines the average M_G for the non-interacting field population. Luminosity evolution of $Q=1$ was assumed.

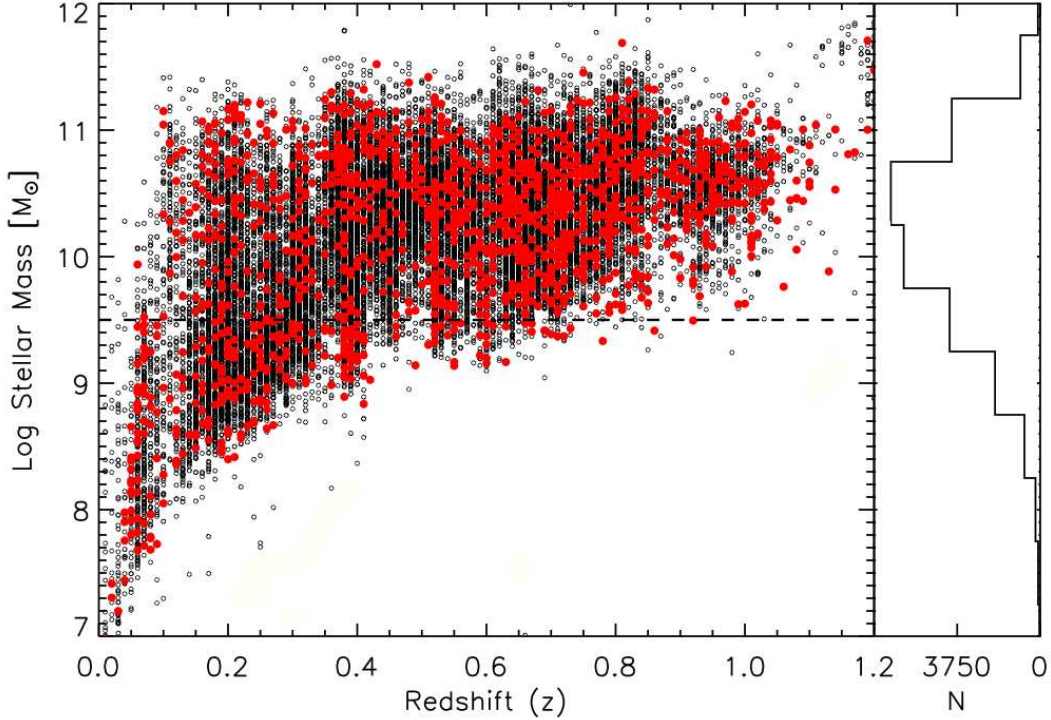


Figure 5.14: Stellar mass as a function of redshift for the CFHTLS D1 and D2 fields. Galaxies classified as non-interacting are shown as open circles, (black) and those undergoing an interaction filled circles, (red). The dashed line defines lower stellar mass limit (Log Mass $> 9.5 M_{\odot}$) considered in following analysis. The histogram on the right shows the stellar mass distribution for the field.

5.7.7 GIF: Mass Dependence

Using the 5-band optical photometry in the CFHTLS we estimated the stellar masses of our sources through template fitting (see section 4.3.2 for details). Figure 5.14 details the stellar mass distribution as a function of redshift for our $i' \leq 21.9$ sample of classified galaxies. Previous merger rate studies derived from observations and theoretical models have suggested that the merger fraction not only varies with optical luminosity as confirmed in the previous section but also depends on stellar mass. It has been suggested that brighter, massive galaxies have the highest merger fractions at $z > 1$ (Conselice et al. 2003; Conselice 2006a; Maller et al. 2006). In order to investigate how the GIF is effected by stellar mass we divided our $i' \leq 21.9$ sample into four mass ranges; low masses ($10^{9.0} \leq M < 10^{9.5}$) and $10^{9.5} \leq M < 10^{10}$), intermediate mass ($10^{10} \leq M < 10^{10.7}$), and high mass galaxies ($M \geq 10^{10.7}$).

The implied interaction fraction is calculated for each stellar mass range. The GIF statistics are described in Table 5.8, and plotted in Figure 5.15.

Interestingly, the interaction fraction is not strongly dependent on stellar mass below $z < 1.0$. There is evidence however that at $z < 0.4$, massive galaxies have a higher (nearly dou-

Table 5.8: Galaxy Interaction Statistics: Mass Dependence

Log Stellar Mass (M_{\odot})	Redshift	N_{Total}	N_{Int}	Int. Fraction [%]
$9.0 \leq M < 9.5$	0.10-0.20	1613	67	4.2 ± 0.5
	0.20-0.40	811	44	5.4 ± 0.8
$9.5 \leq M < 10.0$	0.10-0.2	1069	40	3.7 ± 0.6
	0.20-0.40	1716	44	2.6 ± 0.4
	0.40-0.60	1839	108	5.9 ± 0.6
	0.60-0.80	493	48	9.7 ± 1.4
	0.80-1.00	71	8	11.3 ± 4.0
$10.0 \leq M < 10.7$	0.15-0.35	1515	77	5.1 ± 0.6
	0.35-0.55	3273	114	3.5 ± 0.3
	0.55-0.75	3186	194	6.1 ± 0.4
	0.75-0.95	1701	151	8.9 ± 0.7
	0.95-1.15	385	57	14.8 ± 2.0
$M \geq 10.7$	0.35-0.55	1351	102	7.6 ± 0.8
	0.55-0.75	1345	77	5.7 ± 0.7
	0.75-0.95	1303	108	8.3 ± 0.8
	0.95-1.15	313	43	13.7 ± 2.1

Note: N_{Total} is the number of galaxies within the specified stellar mass and redshift range. N_{Int} is the number of galaxies confidently classified as interacting with a given redshift and stellar mass range. The errors for the interaction fraction were derived using counting statistics.

ble) GIF compared to intermediate and low mass galaxies. This however, is likely a result of massive galaxies being larger and more luminous, and in-turn making any tidal feature more easily detected. Our results are consistent with Conselice (2006a), who found that at $z \lesssim 1$, lower mass galaxies are undergoing mergers at only a slightly higher rate than massive galaxies, which they found to be merging more frequently at $z > 1.0$.

To summarize, we find that the GIF does depend on optical luminosity ($z < 0.7$), however we find little stellar mass dependence.

5.8 Galaxy Merger Rate

Now that we have compiled a large sample of interacting galaxies and have studied the galaxy interaction fraction we can proceed with measuring the galaxy merger rate. It is worth mentioning that our sample of interacting galaxies may contain a small number of galaxy fly-bys that have high relative velocities and will not coalesce or perhaps will do so at over a long period of time (~ 3.5 Gyr).

Although this is a potential complication the effect is likely small, as high velocity encounters do not typically produce strong (bright) tidal features. These high speed encounters can result in substantial mass loss and may be important in the production of dwarf galaxies, but overall these interactions produce little morphological disturbance (Barnes 1998). Therefore

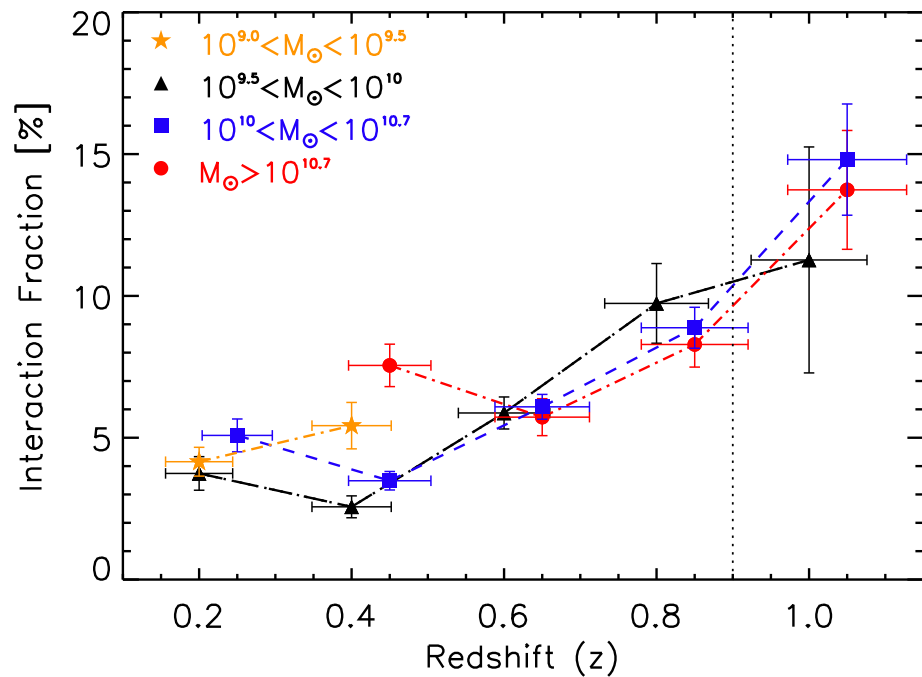


Figure 5.15: The galaxy interaction fraction selected based on stellar mass limits rather than absolute magnitudes. The orange stars represent the GIF for the lowest mass range ($\text{Log } M=9.0-9.5$), while the solid triangles show the GIF computed using a stellar mass range of $\text{Log } M=9.5-10$, solid squares $\text{Log } M=10.0-10.7$ and the solid circles describe the GIF for the highest mass range ($\text{Log } M>10.7$). The vertical error bars are derived using poisson statistics, while the horizontal errors come from the uncertainty in the photometric redshift. The vertical dotted line represents the 75% completeness limit.

we consider the merger rate and interaction rate to be two highly analogous quantities, which can be compared directly. Hence the interaction rate is taken to be equivalent to the merger rate and can be expressed as,

$$\mathfrak{R}_{mg} = N_{int}/T_{mg} \quad (5.6)$$

where N_{int} is the number of interactions, and T_{mg} is the merger time scale. This equation provides a measure of the number of mergers/galaxy/Gyr. Since we have measured the interaction fraction in section 5.7 we now proceed with estimating the appropriate merger time-scale.

5.8.1 Merger Time-scales

An understanding of the time scale on which our method of identifying interactions is sensitive to is key. Dynamical arguments are one method used to derive the merger time-scale, but is best suited for pre-mergers since properties of both members of the interactions can be studied. This method is thoroughly discussed in Chapter 3 section 5.8.1.

Ideally, one could also use galaxy N-body simulations to compile a large suite of merging galaxies with a range of inclinations, viewing angles, orbit parameters, and mass ratios. By performing our classification method to these simulated mergers we could more accurately determine the time scale over which our method is sensitive to. Although work is currently being done by a group at Harvard to compile a data base of galaxy mergers (private communication, Besla 2007), it is not yet complete.

Ultimately, we made use of N-body simulations of galaxies undergoing mergers described in Conselice (2006a) which employs the models of Mihos & Hernquist (1996) and Mihos (2001) to estimate the merger time-scale probed by visually identifying galaxies with strong tidal features. The quantitative method used by many computational codes find that mergers with mass ratios greater than 1:5 can be identified by their large asymmetries (Abraham et al. 1996a; Conselice 2006a). Figure 5.16, taken from Conselice (2006a) illustrates how asymmetry can change with time during a galaxy merger. The amplitude of the asymmetry and the peak positions along the merger time-line can vary depending on the configuration and mass ratios of the merger scenario. Our method of identifying interactions is based on low surface brightness tails and bridges which will probe mergers to lower asymmetries than morphological codes (such as CAS) due to the issues discuss earlier in section 5.2, regarding incomplete source segmentation.

We carefully considered the duration that a galaxy encounter would exhibit the tidal features used in this work to identify interacting galaxies. We visually inspected snapshots of

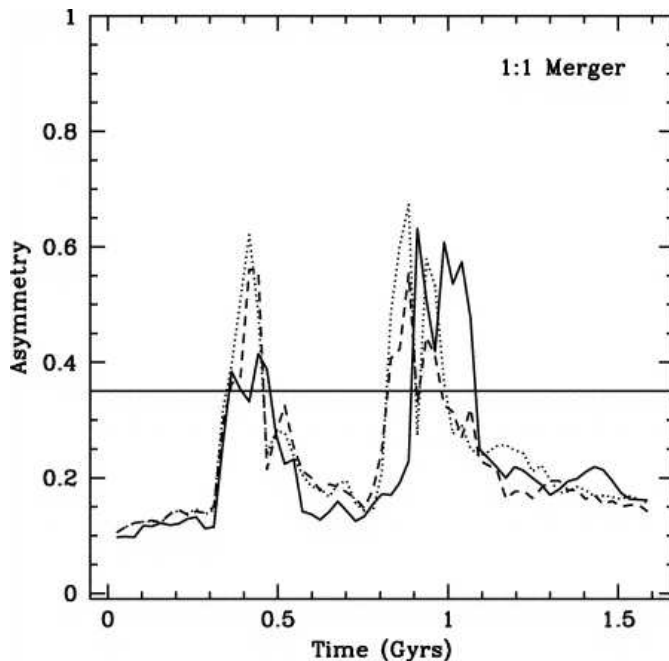


Figure 5.16: The evolution of the asymmetry measurement for 1:1 major mergers from N -body simulations taken from Conselice (2006a). This plot is an illustration of how the asymmetry of a galaxy can change throughout a merger. An estimate of the merger time-scale can be inferred by considering the duration a galaxy's asymmetry is consistent with merger activity. The three dashed lines are from simulations where different types of orbits were used. One galaxy is inclined while the other has a retrograde orbit (solid line), prograde (dashed line), and a simulation with a galaxy in a retrograde orbit while the other is prograde (dotted line). The solid horizontal line defines the asymmetry at which point a galaxy is morphologically consistent with that of a merger ($A > 0.35$) (Conselice 2006a)

a simulated merger (Figure 2 in Conselice (2006a)) noting the duration in which the galaxies would be classified as “interacting” according to our criteria. We also considered the duration that a galaxy would have a high level of asymmetry (Figure 5.16 Conselice (2006a)). Ultimately, we estimate the time-scale being probed by strong visual tidal features to be $0.8 \text{ Gyr} \pm 0.2$.

Now that we have a reasonable estimate of the merger time-scale our identification method is sensitive to, we proceed with measuring the galaxy merger rate.

5.8.2 Computed Merger Rates

In this section, the merger rate is presented along with the number of mergers a typical galaxy in our sample has undergone since the Universe was half its present age. Using equation 5.6, the merger rate for galaxies with stellar masses $\geq 10^{9.5} M_{\odot}$ is shown in Figure 5.17 as a function of redshift. Again, the merger of two galaxies of fairly equal masses is visually identifiable by tidal signatures for roughly $0.8 \text{ Gyr} \pm 0.2$. The large uncertainty in the merger time-scale reflects the various possible merger scenarios, i.e. large mass ratios can extend the merger time-scale.

We find an average merger rate of $R_{mg} \sim 0.075 \text{ mergers gal}^{-1} \text{Gyr}^{-1}$ between $0.1 \leq z \leq 0.65$, which increases to $0.24 \text{ mergers gal}^{-1} \text{Gyr}^{-1}$ at $z \sim 1.0$. The merger rate appears to evolve with redshift as $m = 2.36 \pm 0.56$, where the error in m considers both the poisson errors in the GIF and the uncertainty in the merger time scale. Since the majority of close pair and merger studies in the literature impose optical luminosity cuts we are limited to comparing our results to one study, that of Conselice et al. (2003). We derived the merger rate from the merger fraction statistics of galaxies with stellar masses $\geq 10^{9.5}(M_{\odot})$, in Table 6 of Conselice et al. (2003), assuming a merger time scale of $0.9 \text{ Gyr} \pm 0.2$. Figure 5.17 shows that there is substantial agreement between our measurements and that of derived from (Conselice et al. 2003) (orange points).

5.8.3 Interaction History

Using our GIF results and the merger time scale derived in section 5.8.1 we can calculate a lower limit for the interaction history for typical galaxies in our sample. Equation 5.7 shows that by integrating the fraction of galaxies undergoing an interaction divided by the merger time scale one can obtain the number of interactions an average galaxy undergoes between two points in redshift space.

$$n_{int} = \int_{z_2}^{z_1} \frac{\text{GIF}(z)}{T_{mg}} dt = \int_{z_2}^{z_1} t_H \left(\frac{f_0}{T_{mg}} \right) (1+z)^{m-1} \frac{dz}{E(z)} \quad (5.7)$$

where t_H is a Hubble time, $\text{GIF}(z)$ is the galaxy interaction fraction at a given redshift, f_0 is the GIF at $z \sim 0$, and $E(z) = (\Omega_M(1+z)^3 \Omega_{\Lambda})^{-1/2}$. A power-law increase for the interaction

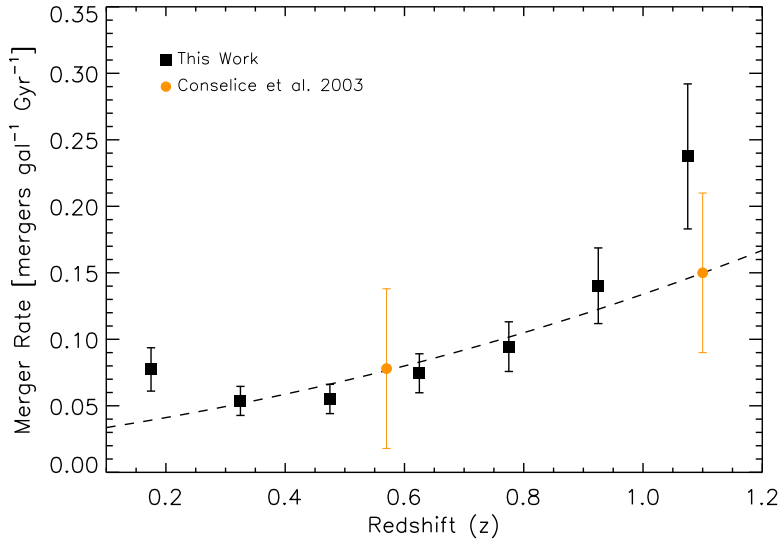


Figure 5.17: The merger rate as a function of redshift in units of mergers/galaxy/Gyr. The filled black squares represent the merger rate derived using interacting galaxies with stellar masses $\geq 10^{9.5}(M_\odot)$. The dashed line outlines the evolution of the merger rate, fit to the CFHTLS-Deep data, where $m = 2.36 \pm 0.56$. All error bars include both the uncertainties of the interaction fractions and merger time scale. The orange circles were derived from Conselice et al. (2003), and show good agreement with our results.

rate was assumed, as it is well fit by the data.

Based on the above equation, and assuming $m = 2.24, f_0 = 0.0215$ (the best fit to all our data in section 5.7.1), we find that a galaxy with a stellar mass $\geq 10^{9.5} M_\odot$ (average mass ratio 3:1) experiences ~ 0.6 mergers from $z = 1.0$ to the present day (see Figure 5.18).

Now that we have established a confident lower limit of the number of galaxies undergoing an interaction since $z \sim 1$ we can begin to investigate the star forming properties of these systems and attempt to shed light on the role interactions play in the CSFR history of the Universe.

5.9 Star Formation Rates of Interacting Galaxies

Interactions and collisions can profoundly affect the evolution of galaxies, through morphological transformations, mass accretion, and perhaps the most brilliant, through induced star formation. Observations of interacting galaxies such as the Antennae (Schweizer 1982) and simulations of major mergers (Mihos & Hernquist 1996; Cox et al. 2006) both provide evidence that interactions can trigger violent starbursts.

Using the 5-band optical photometry of the CFHTLS-Deep survey we derived star forma-

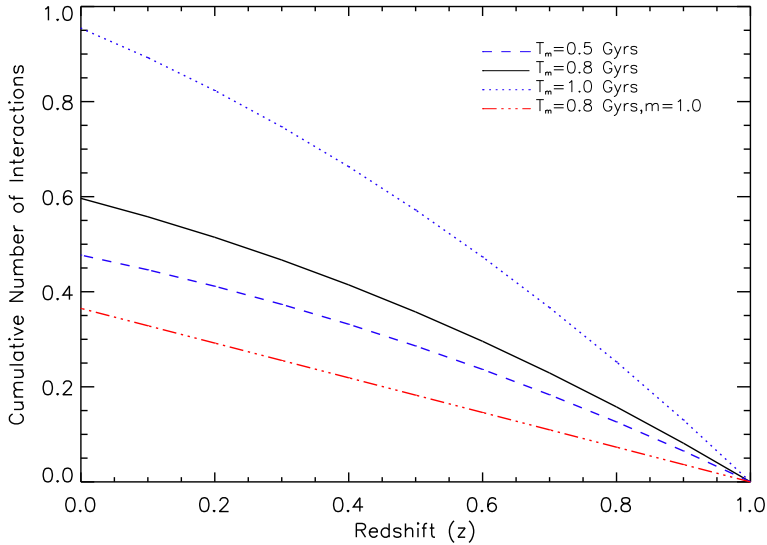


Figure 5.18: The interaction history, or the number of interactions an average galaxy in our sample has undergone since $z \sim 1$ (solid, black line). The coloured lines represent the same measurement but assume a different merger time-scale, as stated in the plots legend. The assumed evolution of the merger rate was $(1 + z)^{2.24 \pm 0.02}$. The red line is presented for comparison purposes assuming little evolution of the merger rate.

tion rates (SFR) for each galaxy in our sample (section 4.3.2 describes the formulation used). We begin by exploring the star forming properties of each class of interacting galaxies. Figure 5.19 shows the average SFR for each interaction type, and the galaxy field population as a function of redshift. All interaction classes from close pairs with tidal bridges (early stage mergers) to galaxies with double nuclei and tidal tails (later stage) exhibit enhanced SFR's a factor of 1.5-4 times that of the field. The level of star formation enhancement also grows with the redshift. At higher redshifts one might expect the average SFR to be larger simply because more gas is available. We do find that the average SFR for field galaxies (which is largely comprised of spiral or disk dominated galaxies ($> 60\%$)) increases marginally with redshift from $\sim 1.4 M_{\odot}/yr$ at $z \sim 0.2$ to $\sim 3.2 M_{\odot}/yr$ at $z \sim 0.75$. For interacting galaxies however, we see a factor of 3 growth in the average SFR with redshift. Once again, this increase could simply be a result of these systems being more gas-rich, allowing tidally triggered starbursts to be more significant at higher redshifts. Figure 5.19 clearly shows that different interaction classes vary substantially in their average SFR's. Galaxies in the first stages of a interaction, those in a close pair linked via a tidal bridge have SFR's similar to the field population (only slightly enhanced at higher redshift). While later stage interactions, those with a tidal tail or double nuclei and tidal tails are the most enhanced, especially at $z > 0.6$.

Although the average SFR for different interacting types is a useful and interesting mea-

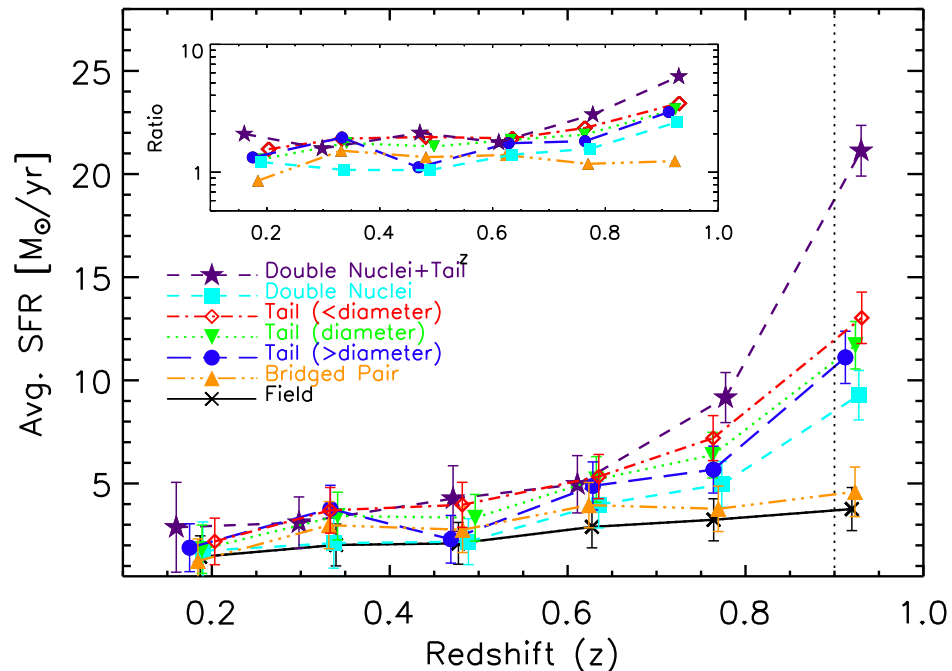


Figure 5.19: The average star formation rates for various interaction classes, as well as the field population. Inset is the ratio of the average SFR of a particular class compared to the field. The field is shown by the x's (black), bridged close pairs by triangle (orange), long tidal tails, circle (blue), intermediate tails, downward triangle (green), short tails, open diamond (red), double nuclei, square (cyan), and double nuclei with tail(s) are shown by stars (purple). The errors bars are the standard deviation of the SFR's.

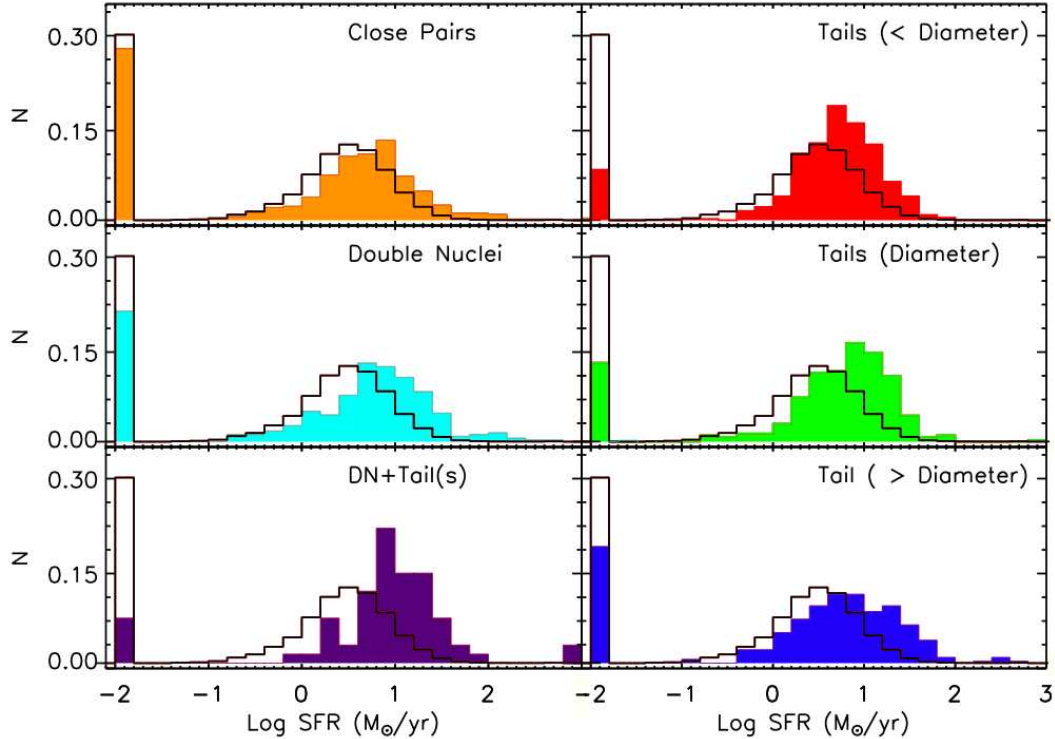


Figure 5.20: The star formation rate distributions for the various interaction classes, as well as the field population normalized so that the integral over the bins is unity. The field distribution is shown in each histogram in black. (Top) bridged close pairs (orange), followed by short tails (red), intermediate tails (green), long tidal tails (blue), double nuclei (cyan), and double nuclei with tail(s) (purple). This figure shows that galaxies with tidal tails and double nuclei have SFR distributions shifted to higher rates compared to the field. The lowest SFR bin (at Log SFR=-2) represents a SFR of zero and has been shifted to this position for plotting clarity.

surement it is also important to understand their SFR distributions. Figure 5.20 shows a histogram of the SFR distributions for each of the primary interaction classes. Generally, the distributions are shifted to higher SFR's than the field (overlaid in black). Clearly, the majority of galaxies with a double nuclei and tidal tail(s) have above average SFR's. This can be explained if this stage of interaction represents a later stage in the merger process, well after the first encounter and prior to the final coalescence of the system. Simulations do suggest that the second passage (or later stage) typically results in the largest starburst (Mihos & Hernquist 1996).

Ultimately, we have shown clear observational evidence that tidal interactions can enhance SF by a factor of 1.5-4 based on broad-band SF estimates. As discussed earlier in this section however, high redshift galaxies may be more gas-rich, in turn they may also harbor large quantiles of dust. It is therefore important to explore the Mid-IR properties of these interacting systems since we may be missing star formation that is being obscured by dust.

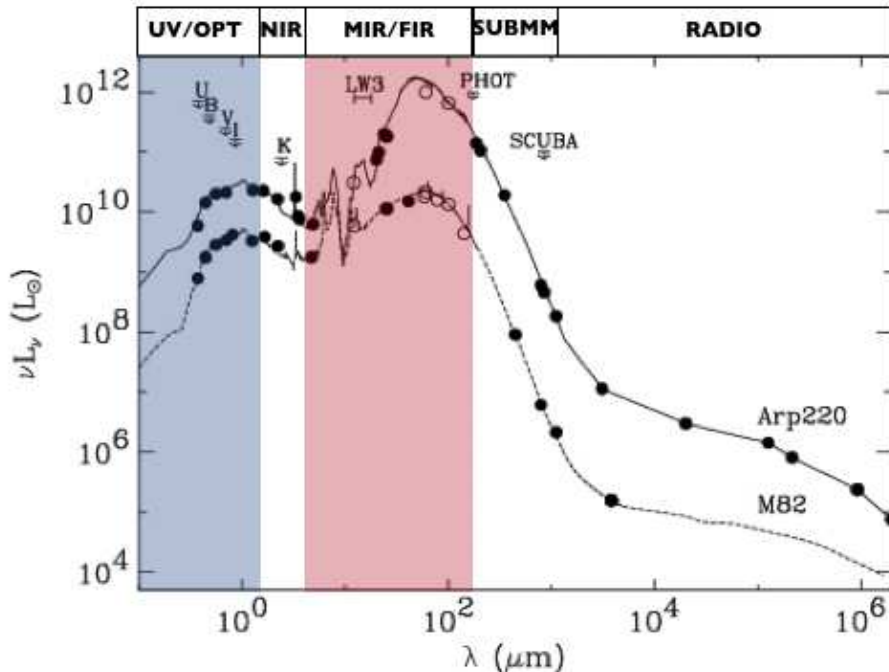


Figure 5.21: The Spectral energy distribution of IR galaxies. The dashed line outlines the SED of M82, while solid line shows the SED of Arp 220. It is clear from this figure that a significant fraction of luminosity is output in the Mid/Far-IR for certain galaxy types, making it an important window to study star formation. The filled and open circles illustrate photometric data, with some finer spectroscopic features included. The data used for these SEDs is summarized in Elbaz et al. (2002). Various wavelengths (filters) are noted in the Figure. The blue region outlines the optical wavelengths, while the red region denotes wavelengths covered by *Spitzer*.

5.10 Mid-Infrared Properties of Interacting Galaxies

Locally, galaxies radiate $\sim 30\%$ of their bolometric luminosity in the Mid to Far IR ($8\text{-}1000\mu\text{m}$) (Soifer & Neugebauer 1991), however luminous IR galaxies (LIRGs and ULIRGs) radiate more than 90% of their of light at these wavelengths. Figure 5.21 illustrates the SEDs of two starburst galaxies M82 and Arp 220 (ULIRG) from the optical to radio. It is clear that a large fraction of star formation in these systems can be traced by the Mid/Far-IR.

Rapid redshift evolution of the number density of LIRGs and ULIRGs points to them being an important star forming phase of a galaxy's life cycle. The intense infrared emission of local LIRGs and ULIRGs appears to be correlated with strong tidal interactions or galaxy mergers of molecular gas-rich spirals (Sanders & Mirabel 1996). It is therefore logical to expect that the IR emission of distant LIRGs and ULIRGs is also due to interactions. Since most of the star formation in the history of Universe is hidden or affected by dust, optically derived SFR's do not provide the full story, unless a dust correction is applied, which is challenging to estimate

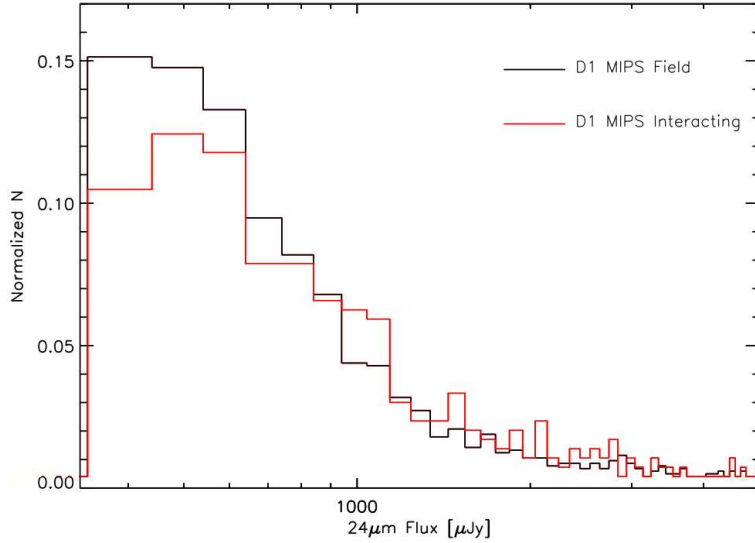


Figure 5.22: The $24\mu\text{m}$ distribution of interacting and non-interacting galaxies in the CFHTLS-D1 field. The histogram is normalized for the area under the curve to be unity. The interacting and non-interacting MIPS bright galaxies have similar $24\mu\text{m}$ distributions.

for individual high redshift galaxies. The Mid-IR, specifically $24\mu\text{m}$, is a good tracer of star formation unaffected by dust extinction, making it a complimentary wavelength and unique window to probe dust enshrouded SF induced by mergers.

With the advent of the *Spitzer* Space Telescope, the Mid-IR properties of distant galaxies have become more accessible. The SWIRE legacy survey overlaps with 0.8 square degrees of the CFHTLS-D1 field. Details regarding the sensitivities and catalogs are discussed earlier in section 4.3.3. Using our sample of optically selected tidally interacting galaxies we present the first $24\mu\text{m}$ galaxy interaction fraction, along with Mid-IR derived SFR's and estimates of the fraction of mergers with potential AGN activity.

5.10.1 MIPS $24\mu\text{m}$ Sample

To ensure a fair comparison between interacting, and non-interacting galaxies a $340\mu\text{Jy}$ limit was imposed on both samples. Figure 5.22 shows that the normalized $24\mu\text{m}$ flux distributions for the interacting and non-interacting samples are comparable. Within the region where D1 overlaps with the SWIRE survey there are 1,072 galaxies detected above $340\mu\text{Jy}$ of which 27% (293) were also optically classified as interacting. It must be mentioned that the depths of the SWIRE MIPS coverage are shallower than that of the XFLS which went down to $100\mu\text{Jy}$.

In order to explore the fraction of MIPS bright galaxies undergoing an interaction we divided the full D1 sample into MIPS detected (MIPS bright, $f_{24} \geq 340\mu\text{Jy}$) and those undetected at $24\mu\text{m}$, which we will occasionally refer to as non-MIPS galaxies. Some objects may

fall into our non-MIPS subset simply because they are below our survey limits, hence the term non-MIPS also includes IR faint galaxies. This is acceptable since we are focusing on the bright MIPS population. Another CFHTLS Deep field (D2) is currently being surveyed by the COSMOS collaboration to depths of $100 \mu\text{Jy}$ at $24\mu\text{m}$, which will allow us to probe the interaction frequency of the faint MIPS population when the data becomes public.

5.10.2 MIPS Galaxy Interaction Fraction

We know that LIRG galaxies play an important role in the CSFR density at high redshift, but the driving mechanisms behind their IR activity are still unclear. By probing the fraction of MIPS bright galaxies that are undergoing an interaction we can shed light on the role merger induced star formation plays in a LIRG's IR luminosity and in turn the CSFR.

We present the first galaxy interaction fraction for bright MIPS galaxies using the CFHTLS-D1 sample in Figure 5.23 and Table 5.9. The fraction of MIPS galaxies that are undergoing a tidal interaction appears to rapidly evolve with redshift, with $12.73\% \pm 2.78\%$ of MIPS detected galaxies involved in an interaction at $z \sim 0.2$, and $\sim 37\%$ at $z \sim 0.9$. We also find that the fraction of non-MIPS interacting galaxies remains significantly lower at all redshifts. Meaning, galaxies with a $24\mu\text{m}$ flux $\geq 340 \mu\text{Jy}$ are on average ~ 10 times more likely to be undergoing a tidal interaction than non-MIPS galaxies (or those fainter than $340 \mu\text{Jy}$) at $z < 1$. This result is consistent with our earlier findings in the XFLS where MIPS galaxies were 5 times as likely to have a close companion (Bridge et al. 2007a). This suggests that as the merger process progresses, from close pairs to later stages interactions exhibiting long tidal tails, bridges and double nuclei, the MIPS flux increases. This is again consistent with idea that tidal interactions between galaxies induce star formation.

Another interesting result of this work comes from the relatively high fraction of bright MIPS galaxies that show tidal interactions. At $z \sim 0.7$ we find that approximately $35\% \pm 5\%$ of MIPS galaxies brighter than $340 \mu\text{Jy}$ are interacting, compared to 10% found by Lotz et al. (2006) using the Gini coefficient and M_{20} parameters at the same redshift. However, our fraction of interacting MIPS galaxies is at first glance, consistent with that found by Bell et al. (2005) who visually determined 30% of their 442 MIPS galaxies to be interacting at $z \sim 0.7$. Although we find a MIPS interaction fraction higher by $\sim 5\%$ compared to Bell et al. (2005) we are probing slightly bluer wavelengths by using i' -band compared to the z -band used by Bell et al. (2005), making us slightly more sensitive to star formation, and features such as tidal tails. Another point to consider is that the classification scheme used by Bell et al. (2005) included less robust interaction signatures (i.e. galaxies with disturbed appearances). If we broaden our criteria for an interaction and include systems similar to that used by Bell et al. (2005), the number of interacting MIPS galaxies is nearly 50% , up from $\sim 30\%$.

Table 5.9: MIPS Galaxy Interaction Statistics

Redshift	N_{Total}	N_{Int}	Int. Fraction [%]
$24\mu\text{m}$ Detected			
0.10-0.25	165	21	12.7 ± 2.8
0.25-0.40	213	49	23.0 ± 3.3
0.40-0.55	181	52	28.7 ± 4.0
0.55-0.70	146	49	33.6 ± 4.8
0.70-0.85	166	64	38.6 ± 4.8
0.85-1.00	98	36	36.7 ± 6.1
$24\mu\text{m}$ Undetected			
0.10-0.25	1783	41	2.3 ± 0.4
0.25-0.40	2176	49	2.3 ± 0.3
0.40-0.55	2357	77	3.3 ± 0.4
0.55-0.70	2313	82	3.5 ± 0.4
0.70-0.85	1490	75	5.0 ± 0.6
0.85-1.00	678	57	8.4 ± 1.1

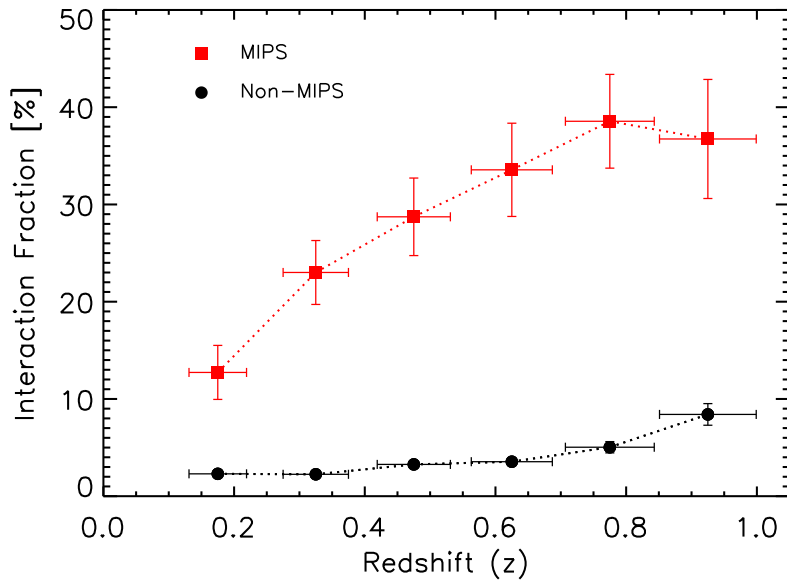


Figure 5.23: The $24\mu\text{m}$ galaxy interaction fraction (red). The GIF for non-MIPS galaxies is shown in black. It is clear that the MIPS objects interact more frequently at all redshifts and the MIPS GIF evolves rapidly with redshift. The vertical error bars are derived using counting statistics, while the horizontal error bars represent the photometric redshift error.

To summarize, over $0.1 \leq z \leq 1.0$ and $f_{24} > 340 \mu\text{Jy}$ we find that on average $\geq 30\%$ of bright MIPS galaxies are strongly interacting, with a rapidly evolving GIF. But what is causing the star formation in the remaining 70%? We find that another 15% of MIPS galaxies are classified as ‘probable’ interactions (i.e. short tails, disturbed or classed as probable tailed galaxies or bridged pairs), while 40% of MIPS sources have spiral or disk-like appearances, and another 10% are bulge dominated and the remaining 5% are combinations of other classes.

5.10.3 Mid-IR GIF: Luminosity Dependence

It is clear from Figure 5.23 that the MIPS GIF evolves rapidly. However, it is important to consider any potential Mid-IR luminosity dependence on the GIF. It has been well established that at high and low redshifts nearly all ULIRG galaxies are merger dominated, but the role merging plays in LIRG or sub-LIRG galaxies at high redshifts is unclear. To investigate the Mid-IR dependence on the GIF we divided our MIPS sample into three IR luminosity ranges, $10.7 < \log L_{IR}(L_\odot) \leq 11.3$, $11.3 < \log L_{IR}(L_\odot) \leq 12$, and $\log L_{IR} > 12.0$. Due to the rapid evolution of IR galaxies, and the depth of the SWIRE survey we can not probe each luminosity range over extended redshifts, however there is some overlap as shown in Figure 5.24. As expected, we find that ULIRG galaxies are predominately ($\sim 65\%$) classed as mergers. The remaining 35% are also likely to be undergoing a merger, but were not classed as such probably because these objects are at high redshift where ground-based morphological classification becomes difficult unless the interaction features are large and bright.

Figure 5.24 clearly reveals a strong Mid-IR luminosity dependence on the GIF, a factor of two larger than that seen in the optical (Figure 5.12). The interaction fraction increases with increasing IR luminosity.

5.10.4 MIPS Interaction Fraction: Class Breakdown

Due to our large sample of interacting MIPS galaxies we can further breakdown the MIPS GIF according to interaction type. This allows us to explore the stages or levels of tidal interaction that correlate with the $24\mu\text{m}$ flux and in turn star formation, within the luminous IR population.

Figure 5.25 shows the interaction fraction for both the MIPS and non-MIPS population broken down by interacting type (i.e long tails, bridge pairs etc.). As expected from the overall MIPS, non-MIPS interaction fractions, all interaction types have a higher frequency of being MIPS sources at all redshifts. We find that more than 56% of galaxies with a double nuclei and tidal tail are brighter than $340 \mu\text{Jy}$ at $24\mu\text{m}$, while 40% of medium tails, 46% of long tidal tails and 32% of bridged pairs are MIPS bright.

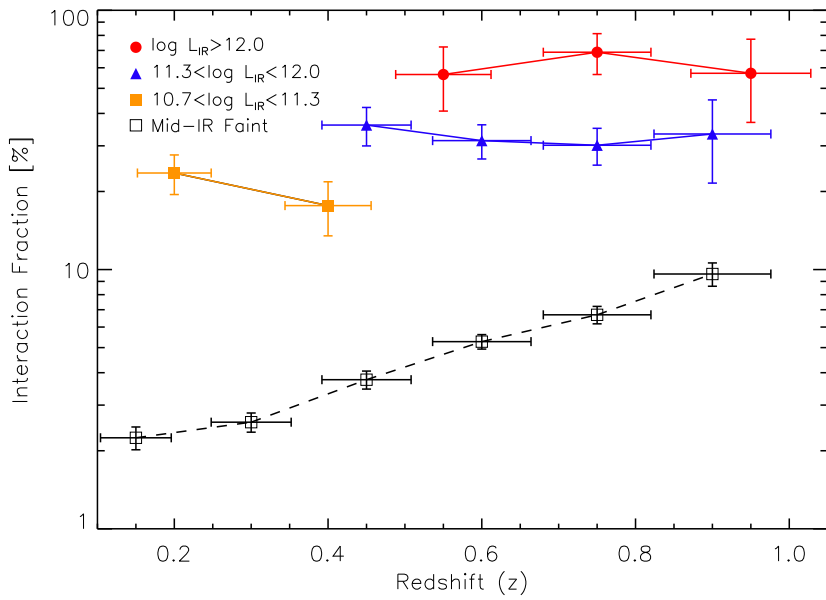


Figure 5.24: The interaction fraction as a function of redshift for three IR-luminosity ranges, $10.7 < \text{Log}L_{\text{IR}} < 11.3$ (orange, squares), $11.3 < \text{Log}L_{\text{IR}} < 12.0$ (blue, triangles), and $\text{Log}L_{\text{IR}} > 12.0$ (red, circles). For comparison the GIF for IR-faint galaxies shown in black is included. This figure clearly shows a strong IR-luminosity dependence on the galaxy interaction fraction, a factor of two larger than the optical luminosity dependence.

Our Mid-IR findings support the idea that nearly half of luminous IR galaxies at $z \sim 0.8$ are driven by galaxy-galaxy interactions, and mergers become an increasingly important mechanism for driving IR emission at higher redshift.

5.10.5 Mid-IR Star Formation Rates

In the previous section we used the $24\mu\text{m}$ flux as a proxy for star formation, however we can take this a step further by deriving SFR's directly from a galaxy's IR luminosity and compare them to those determined from the optical photometry derived in section 5.9.

As mentioned earlier, luminous IR galaxies are known to emit the majority of their luminosity at far-infrared wavelengths ($> 90\%$). Thus, star formation rates derived from optical observations of this population are merely a lower limit to the total SFR. The Mid-infrared has been found to be a good tracer of star formation, and it is less affected by dust extinction. Its shortcoming, however, is that the typically adopted far-infrared SFR calibration (Kennicutt 1998), is based on the assumption that all the UV emission is from massive stars which gets reprocessed by dust into IR flux, and does not consider the effects of UV radiation leakage, or that a fraction of the UV emission is a result of an active galactic nuclei (AGN).

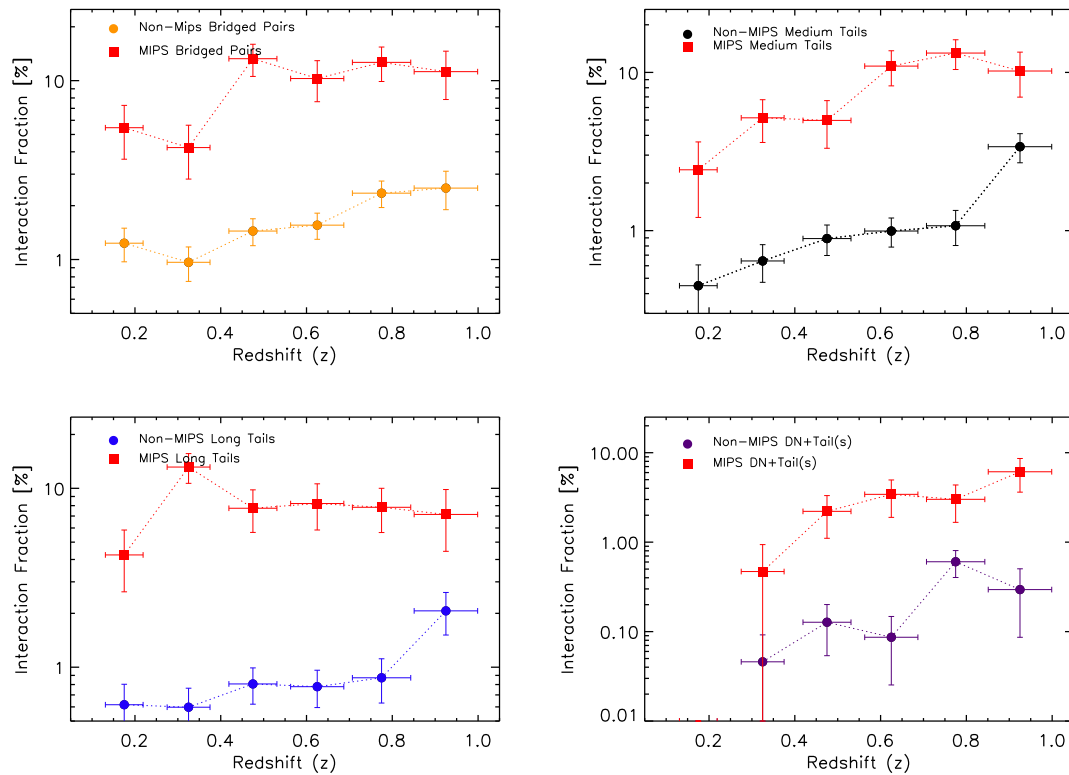


Figure 5.25: The MIPS GIF broken down by interaction type. In all figures, red outlines the GIF for MIPS sources, while the GIF for non-MIPS galaxies is shown by the colours noted in each figure. As expected from the optical results MIPS galaxies have higher interaction fractions, suggesting that merger activity likely plays an important role in their IR luminosity and in turn SF.

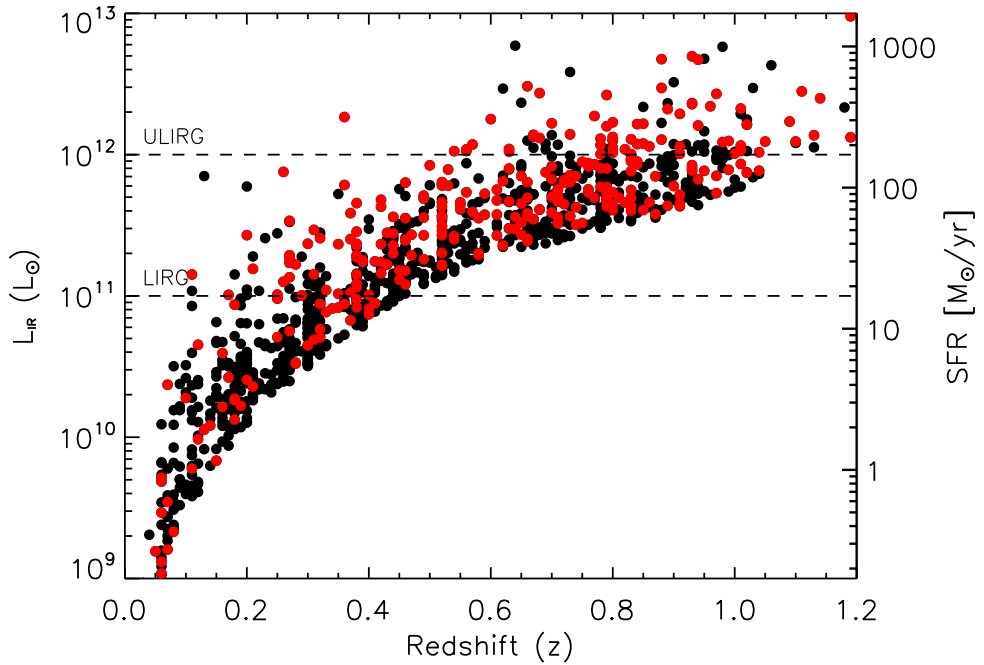


Figure 5.26: Total Infrared luminosity $L_{IR}[8\text{-}1000\mu\text{m}]$ (left axis) vs. redshift for the MIPS 24 μm sample in the CFHTLS/SWIRE field. The black circles represent field galaxies, while the red circles indicate the interacting sample. This figure, like that shown for the XFLS sample (Figure 3.14) illustrates the strong luminosity evolution of the Mid-IR population. The L_{IR} was derived using luminosity dependent SED template suites from the literature (see text for details). The dashed lines define the L_{IR} regions that classify LIRGs ($L_{IR} \geq 10^{11} L_{\odot}$) and ULIRGs ($L_{IR} \geq 10^{12} L_{\odot}$). The star formation rates plotted on the right axis in M_{\odot}/yr for all the 24 μm sources with $f_{24} > 340 \mu\text{Jy}$ assume the calibration from Kennicutt (1998).

To calculate the SFR_{IR} , we first computed the bolometric infrared luminosity from our 24 μm observations, in the same manner outlined in section 3.7.1. If we assume that the dominant heat source of the IR dust radiation is young stars, then the conversion of L_{IR} to a star formation rate can be made with the calibration of Kennicutt (Kennicutt 1998),

$$SFR_{IR} = 4.5 \times 10^{-44} L_{IR} (\text{ergs}^{-1}), \quad (5.8)$$

as also described in section 3.8.1. Figure 5.26 shows the L_{IR} and equivalent SFR distributions for the MIPS CFHTLS sample. The SWIRE 24 μm imaging ($f_{24} > 340 \mu\text{Jy}$) is not as deep as that in the XFLS ($f_{24} > 100 \mu\text{Jy}$) which is evident when a comparison is made between Figure 5.26 and Figure 3.14. Beyond $z > 0.5$ we quickly become incomplete when probing the LIRG population, however the CFHTLS covers a larger volume, resulting a larger sample of bright LIRGs and ULIRGs than was available in the XFLS.

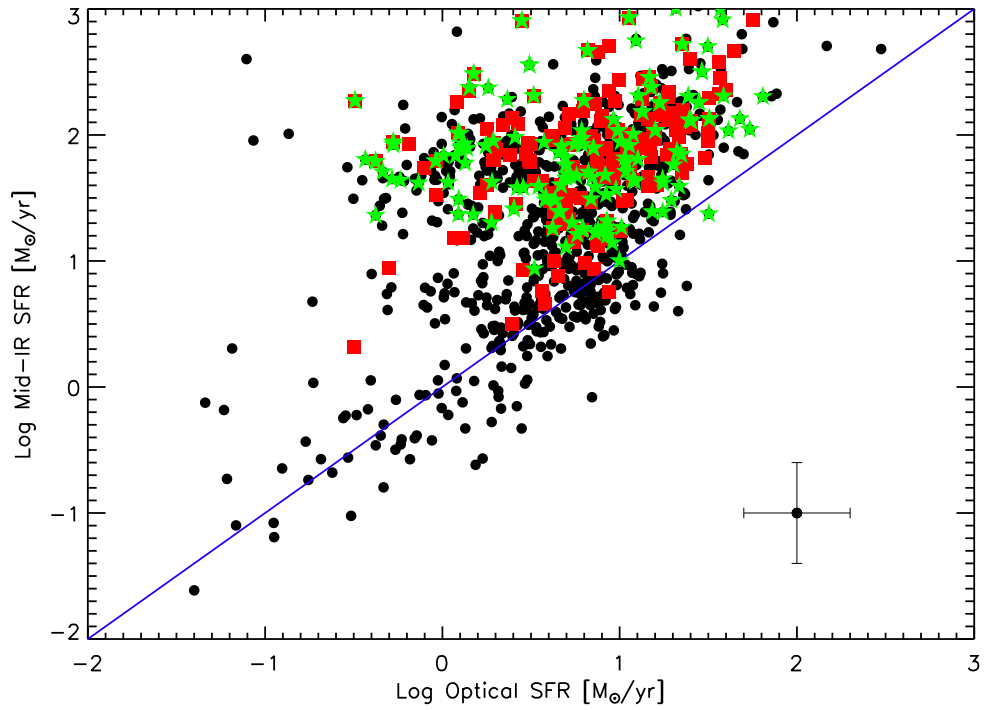


Figure 5.27: Comparison of the optically derived SFR's to IR SFR's. Open (black) symbols represent the field population, squares (red) denote interacting galaxies, while stars (green) mark galaxies whose IRAC colours are consistent with an AGN. This figure shows that generally SFR_{IR} are larger than those derived optically. Also interacting galaxies show enhanced SFR_{IR} compared to the field. A representative error bar is shown in the lower right

Figure 5.27 compares the star formation rates derived optically (SFR_{opt}), to those determined using the IR luminosity (SFR_{IR}). It is readily apparent that the SFR_{IR} are generally, larger than those derived optically, especially for interacting systems. Galaxies that have been classified as interacting have been highlighted in red, while field galaxies are represented in black. The optical and IR SFR's agree reasonably well for galaxies with low levels of star formation, however there is large subset of $24\mu m$ detected galaxies whose SFR_{IR} are a factor of ~ 10 larger than those derived optically. Some points to consider are that while SFR_{opt} can result in an underestimate of the SFR in dusty galaxies, large UV/optical escape fractions due to geometry or dust opacity can cause the SFR_{IR} to be overestimated. Additionally, if a significant fraction of a source's bolometric luminosity is from a central AGN the SFR_{IR} will also be overestimated. In Figure 5.27 galaxies that were found to have IRAC colours consistent with an AGN (see section 3.7.6 for details) were highlighted (green,stars), but do not exclusively have the highest SFR_{IR} of the sample, and may be composite systems (both SF and AGN).

Since Figure 5.27 shows an indication that strongly interacting galaxies have SFR_{IR} greater than the field we explored the normalized SFR_{IR} distribution for each interacting class com-

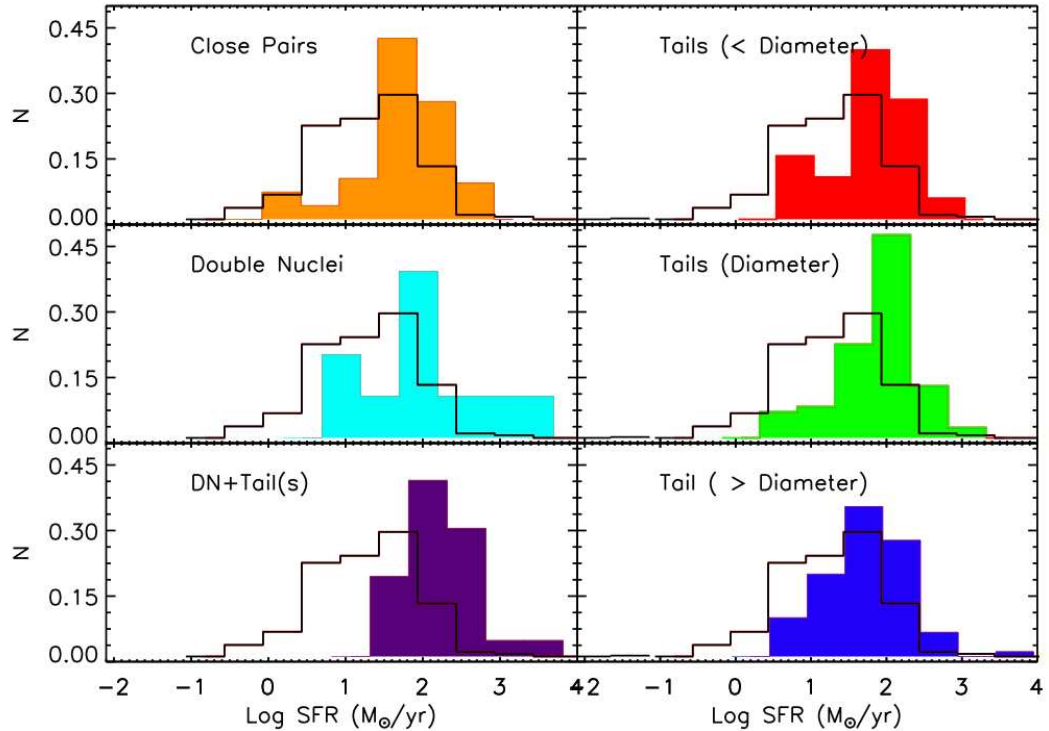


Figure 5.28: Comparison of the normalized (area equal to unity) SFR_{IR} for interacting galaxies (filled, colour) and the field (with interacting galaxies removed). (Top Left) describes the SFR distributions for galaxies classed as a close pair with a tidal bridge, (right) galaxies with a “short” tidal tail. The middle panel shows the SFR’s for galaxies with a double nuclei (left;cyan), and intermediate length tidal tails (right;green), while the bottom panel describes galaxies with a double nuclei accompanied by a tidal tail (left;purple), and those with long tidal tails (right;blue). The field is represented by the black lines. This plot shows that all interacting types have enhanced star formation rates on average $4\times$ that seen in non-interacting field galaxies.

pared to the non-interacting field population, as done in section 5.9 for the SFR_{opt} . Generally, interacting galaxies were found to have $\text{SFR}_{IR} \sim 4\times$ higher than the field, while optically the enhancement was found to be a factor of ~ 2 . Irrespective of the absolute SFR quantities derived by the IR or optical, a clear result from this work is that strongly interacting galaxies, those with tidal tails and bridges have on average, star formation rates a factor of 2-4 times higher than isolated non-interacting galaxies.

5.10.6 Merger-Starburst-AGN Connection?

The relationship between mergers, and the onset of star formation and AGN activity has direct bearings on our understanding of the early Universe. A large contribution from obscured AGN would complicate the deduction of the star formation history of the Universe from luminosity functions. There is growing evidence that star formation and AGN activity go hand

in hand. It seems likely that a triggering mechanism for starbursts is galaxy interactions as we have shown in this work, however, the nature of the connection between mergers and the onset of AGN activity is very unclear.

The most widely supported merger scenario involving infrared galaxies (Sanders et al. 1988) stems from the Toomre (1977b) sequence. In this scheme when two galaxies begin to interact, they lose angular momentum and orbital energy to the dark matter halo and/or tidal features, ultimately coalescing into a single galaxy. In this scenario, star formation is tidally triggered followed by the onset of AGN activity at later stages.

There have however, been conflicting observational findings regarding the timing of the onset of AGN activity in merging galaxies. Recently, Ellison et al. (2007, in prep) found an AGN fraction in close galaxy pairs to be similar to that found in galaxies without a companion. Kewley & Dopita (2003) supports the scenario that AGN activity is triggered by interactions but it is anti-correlated with the merger sequence, meaning later stage mergers are dominated by SF rather than AGN. Other works in the late 1980's and 1990's find no correlation between mergers and AGN activity (Lutz et al. 1998) and even a deficiency of AGN in advanced mergers and strongly interacting systems (e.g. Bushouse 1986). In contrast Smith & Heckman (1989) and Bahcall et al. (1997) showed that the precursors to at least the most powerful AGN have been gas-rich mergers, as tidal tails were evident (Smith & Heckman 1989; Bahcall et al. 1997).

It is clear that the connection between interactions and AGN activity is highly uncertain. To further examine this connection, we have applied the IRAC colour criteria to highlight AGN candidates from both our sample of strongly interacting galaxies and the field population. We then explored the fraction of AGN as a function of interaction type (or stage), and redshift.

5.10.7 IRAC Colour Selection: AGN Candidates

Recall the discussion in section 3.7.6 which outlines the successful use of identifying AGN in the Mid-IR by their strong continuum (Laurent et al. 2000; Lacy et al. 2004; Stern et al. 2005).

The four channel *Spitzer* IRAC photometry (3.6, 4.5, 5.8 and $8.0\mu\text{m}$) was used to identify the region in colour-colour space where AGN dominated sources tend to reside. This region selects AGN candidates, whose SEDs are consistent with AGN activity (power-law like) with fairly high accuracy, as shown by Lacy et al. (2007). Figure 5.29 shows the IRAC colours for the interacting and non-interacting (referred to as the field) sample of galaxies from the CFHTLS-D1 field. The dashed line defines the region expected to be occupied by AGN.

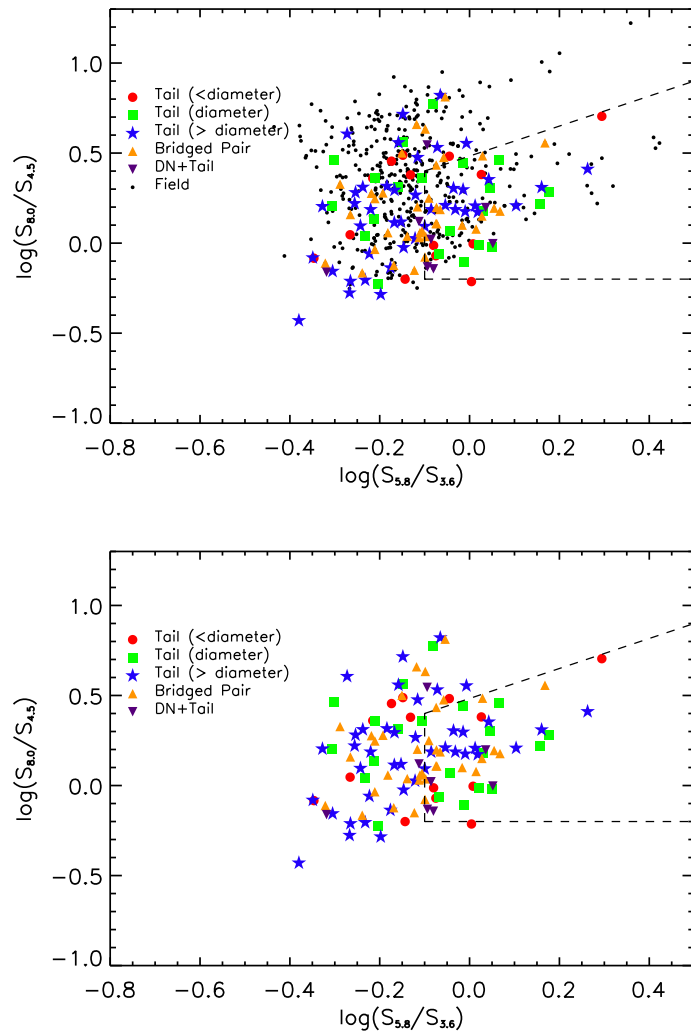


Figure 5.29: IRAC Colours of MIPS detected ($f_{24} \geq 340 \mu\text{Jy}$) interacting and field galaxies between $0.1 \leq z < 1.0$, with stellar masses $M > 10^{9.5} M_\odot$. The dashed line defines the region expected to be occupied by AGN from Lacy et al. (2007). (Top) IRAC colours for both interacting (coloured symbols defined in legend of plot), and non-interacting or field galaxies (black circles). (Bottom) Exclusively shows the IRAC colours of strongly interacting galaxies with the field removed for clarity.

5.10.8 AGN Fractions

Overall we find that $\sim 24\%$ of field galaxies between $0.1 \leq z < 1.0$ with stellar masses $M > 10^{9.5} M_{\odot}$ and $f_{24} > 340 \mu\text{Jy}$ fall into the Mid-IR colour space consistent with harboring an AGN. This result is in agreement with that found by other studies (Choi et al. 2006; Lacy et al. 2007) with similar flux limits.

When we consider all strongly interacting galaxies, we find an AGN fraction of 41%, 1.7 times that found in non interacting galaxies. Simulations of merging galaxies show that throughout the merger sequence interstellar gas can be driven inwards to the nucleus after the first encounter (Mihos & Hernquist 1996). It must be noted, however, that the triggering of gas inflows and nuclear activity depends on a variety of factors (Mihos & Hernquist 1996). One such factor is orbital geometry, as prograde collisions drive inflow more rapidly than retrograde collisions due spin-orbital coupling. Another consideration is the presence of a bulge which promotes disk stability delaying the gas inflow until later in the merger, in contrast to disk encounters (no bulge) which typically readily form bars allowing rapid inflow and central activity.

5.10.9 AGN Fraction: Interaction Type

The AGN fraction for interacting galaxies broken down by type is described in Table 5.10. In the CFHTLS Deep Survey we find that galaxies in a close pair connected by a tidal bridge, showed AGN fractions of $42\% \pm 11\%$, just over 1.5 times that found in the field. Recall that in the XFLS we found that galaxies in a pre-merger or close pair phase (no morphological criteria considered) had AGN fractions similar to the field (only 2% higher), which is also found by Ellison et al (2007, in prep). The differing results found in the XFLS and CFHTLS-Deep for “close pairs” could be explained purely by the stage of the merger process. In both Bridge et al. (2007) and Ellison et al. (2007 in prep) close pairs were selected primarily to have projected separation of $\lesssim 20 h^{-1}\text{kpc}$, resulting in samples dominated by pre-mergers, before the first encounter, while the CFHTLS-Deep close pairs were identified based on the existence of a connecting tidal bridge. The presence of a tidal bridge ensures that the paired galaxies are indeed interacting, are not a projection effect and have undergone at least one close interaction. The heightened AGN fraction could be a result of gas more efficiently being driven inwards from the disk to the nucleus by tidal torques.

Galaxies with intermediate and long tidal tails were found to have AGN fractions of $\sim 52\%$ and $\sim 30\%$, while galaxies with a double nuclei (and tidal tail) have the highest AGN fraction of all interacting classes at $\sim 63\%$. Our observational findings imply that AGN activity is enhanced or triggered at all stages of the merger sequence after the first encounter.

Table 5.10: Fraction of MIPS Galaxies with AGN Signatures

Morphological Class (Code)	Num. of AGN	Num. of Non-AGN	AGN Fraction [%]
Short Tailed (5)	5	9	35.7 ± 16.0
Intermediate Tailed (6)	11	10	52.4 ± 16.0
Long Tailed (7)	13	29	30.1 ± 8.6
Close Pairs with Bridge (8)	15	21	41.7 ± 10.8
Double Nuclei with Tail (10)	5	3	62.5 ± 28.0
Field (non-interacting)	102	315	24.3 ± 2.4
All Interacting Galaxies	44	63	41.1 ± 6.2

Since the highest AGN fraction is seen in one of the latest stages our classification scheme, our observations support the merger scenario of Sanders et al. (1988) for IR galaxies, where AGN activity is largely elevated at later stages of the merger sequence.

Since the formation of a bar is an avenue for driving inflows into the central region of a galaxy we thought it necessary to explore the AGN fraction of the subset of galaxies we clearly identified as having a bar structure. Interestingly, barred galaxies that show no signs of interactions have AGN fractions similar to the field at 23%, suggesting that the presence of a bar is not a primary requirement for AGN activity.

Again, it must be said that not all the galaxies identified as AGN by their IRAC colours will be AGN, some galaxies will be PAH dominated (Sajina et al. 2005). However, the high success rate of this technique supports the finding that strongly interacting galaxies appear to have a higher frequency of AGN activity than non-interacting galaxies. Further follow-up work with spectroscopic observations is required to confirm our findings. Additionally, disentangling the contribution from SF and AGN to the IR luminosity of LIRGs and ULIRGs is yet another question worthy of further study and need of follow-up (see section 6.2).

5.11 Summary

In this chapter we have presented the first statistically confident galaxy interaction fraction as a function of redshift and its dependence on optical and Mid-IR luminosity as well as stellar mass. By using the high quality, deep 5-band optical photometry from the CFHTLS-Deep survey, we developed a new classification scheme to identify strong tidal features marking a recent or ongoing merger. We visually classified $\sim 27,000$ galaxies, compiling the largest catalog of interacting galaxies (~ 1200) in the current literature.

We have shown that the frequency of galaxy interactions appears to evolve with redshift as $(1 + z)^{2.24 \pm 0.24}$, with no strong stellar mass dependence. There is a some indication of an

optical luminosity dependence at low redshift, whereby the interaction fraction is elevated by $\lesssim 5\%$ for galaxies with $M_G < -21$. However, this could be a result of merely being able to detect low surface brightness features such as tidal tails in brighter objects that are relatively nearby.

When the Mid-IR luminosity of galaxies is considered we find that MIPS $24\mu\text{m}$ detected galaxies are 10 times more likely to be interacting than those below the flux limits of the SWIRE survey. We also find the interaction fraction to be strongly dependent on Mid-IR luminosity, where galaxies with a higher MIR luminosity are more likely to be interacting. As $24\mu\text{m}$ flux is in part a tracer of star formation the higher interaction frequency for MIPS galaxies supports the enhanced star formation rates derived both from the optical and Mid-IR that were found for our sample of interacting galaxies.

We have also shown that galaxy interactions appear to more frequently harbor an AGN, consistent with simulations predicting that interactions can be a mechanism for funneling gas into the inner central regions of the galactic nucleus (Mihos & Hernquist 1996; Hopkins et al. 2005).

This chapter presented a consistent picture of galaxy evolution where by galaxy interactions occurred more frequently in the past, typically trigger bursts of star formation and are mechanisms for feeding or triggering AGN activity. It also provides evidence that mergers play a significant role in driving the IR emission of LIRGs.

Chapter 6

Summary and Future Prospects

6.1 Summary of New Results

As most of the star formation in the history of our Universe was enshrouded by dust, the absorption and thermal re-emission of stellar UV light by dust grains into the Mid to Far-IR make this wavelength range key to tracing the global SFR. The results of Le Floc'h et al. (2005), clearly showed that luminous IR galaxies become the dominant population contributing to the comoving IR energy density (for $z > 0.6$) and house more than two thirds of the star formation activity at $z \sim 1$. Locally, galaxy mergers are typically responsible for IR luminous phases, however their role in higher redshift LIRGs remains highly debated.

This dissertation has approached the star formation and merger evolution of interacting galaxies in two new ways. By probing the Mid-IR properties of close galaxy pairs, morphological mergers and the merger rate evolution of LIRGs and ULIRGs we were able to study the star forming properties of these systems uninhibited by dust. We were also able to quantify the role merging plays in the IR luminosity and CSFR densities out to $z \sim 1$.

Secondly, we have developed a new classification scheme to securely identify interacting galaxies based on dynamical signatures, such as tidal bridges and tails. Through the application of this new technique, alongside traditional methods of identifying mergers, we were able to address a central yet remarkably simple paradigm of galaxy formation and evolution which asks, for a given galaxy mass and type, what, on the average is its star formation and merger history, and how are the two related? Also, what role do AGN play in these processes?

This dissertation investigated these central questions by applying a variety of methods to identify galaxies throughout all stages of the merger sequence using both the XFLS and CFHTLS-Deep multi-wavelength surveys. The principle conclusions of this work are:

- A new classification scheme was developed to identify galaxies involved in a merger, through the presence of tidal tails and bridges.
- The new classification technique was applied to the CFHTLS-Deep Survey's high quality, deep multi-band imaging, yielding the largest catalog of tidally interacting galaxies (>1200) in the current literature, ranging from low to high redshift ($0.1 \leq z \leq 1.15$).
- By counting the number of interacting galaxies, limited by stellar mass, over a range of redshifts we measured the first statistically strong, lower limit of the galaxy interaction fraction out to $z \sim 1$. This measurement suggests moderate evolution of the interaction fraction and merger rate, going as $(1+z)^{2.24 \pm 0.24}$ and is inconsistent with a little or no evolution model. There also appears to be little stellar mass dependence on the interaction fraction above $M > 10^{9.5} (M_\odot)$.
- Using a spectroscopic sample of galaxies from the *Spitzer* XFLS we identified close galaxy pairs separated by $5h^{-1}\text{kpc} \leq r_{proj} \leq 20h^{-1}\text{kpc}$ and $\Delta m \leq 1.5$ along with late stage mergers based on their quantitative asymmetries ($A \geq 0.35$). By taking advantage of the Mid-IR imaging over the XFLS field we derived the first close pair fraction for IR bright and faint galaxies. We find that the merger rate for LIRG phase galaxies evolves as $(1+z)^{2.12 \pm 0.93}$. However, this evolution is not seen when IR faint mergers ($< 0.1mJy$) are included.
- IR bright close galaxy pairs are notably more asymmetric than IR faint galaxy pairs, implying that interactions play a role in their IR activity.
- By probing the $24\mu\text{m}$ properties of galaxies in the CFHTLS and XFLS we were able to demonstrate that Mid-IR bright galaxies have a high incidence of being involved in a interaction. We find that $\sim 40\%$ of galaxies at $z \sim 0.8$ are involved in an interaction, while $\sim 10\%$ have a close companion (the deeper XFLS data found that 25% of MIPS galaxies had a close companion). This high interaction fraction for MIPS galaxies clearly indicates a link between merger activity or stage, and star formation. The interaction rate of IR bright galaxies also appears to evolve rapidly with redshift, pointing to a increasingly important role of interactions and mergers in driving the IR emission of LIRG phase galaxies at $z \gtrsim 0.6$.
- We estimate that 40 – 60% of the infrared luminosity density at $z \sim 1$ can be attributed to galaxies involved in some stage of a major merger, indicating that merger-driven star formation is responsible for at least 30 – 40% of the star formation density at $z \sim 1$.

- Star formation rates derived from both optical and Mid-IR imaging show that interacting galaxies have on average enhanced SFR's 2-4 times higher than that found in the "non-interacting" field population, ranging from a few-100's M_{\odot}/yr (in ULIRGs even 1000's M_{\odot}/yr).
- By investigating the Mid-IR colours of galaxies we also found that interacting galaxies (all types) are on average 1.7 times as likely to have SEDs consistent with some level of AGN activity compared to that seen in non-interacting galaxies. This result further supports the hypothesis of a causal connection between merging, starbursts and triggered AGN activity.

This dissertation has presented a picture of galaxy evolution whereby galaxies appear to interact more frequently at higher redshifts (specifically IR luminous galaxies), can trigger bursts of star formation, and in some cases AGN activity. It shows that the role of mergers is one of increasing importance with redshift in the context of the decline in the CSFR and as the driver of LIRG energy sources.

6.2 Future Work

In this section we briefly outline several future directions in which the work in this thesis can, and should be extended.

6.2.1 Spectroscopic Observations of Close Galaxy Pairs

First, as this dissertation has in part relied on photometric redshifts, and spectroscopic redshifts of only one member of a close galaxy pair candidate, optical and/or Mid-IR spectra would not only increase the accuracy of the redshift measurements thereby strengthening the confidence in evolutionary trends, but also reduce the contamination by projected close galaxy pairs. To help address this we have undertaken a spectroscopic Study of Close Optical Pairs In CFHTLS (SCOPIC) using Magellan's multi-object spectrograph IMACS. Data acquisition is now complete with a total of 10 nights, targeting ~ 1500 close galaxy pairs, (both pair members), and ~ 500 $24\mu\text{m}$ detected galaxies. This rich data set will allow us to investigate the accuracy of selecting close galaxy pairs based on photometric redshifts, and a more accurate determination of the optical star formation rates through line diagnostics.

The optical spectra of MIPS sources will give us additional insight in the connection between interactions, star formation and AGN activity. Interactions identified by their IRAC colours to be consistent with AGN could potentially be confirmed, if the system is not too dust obscured.

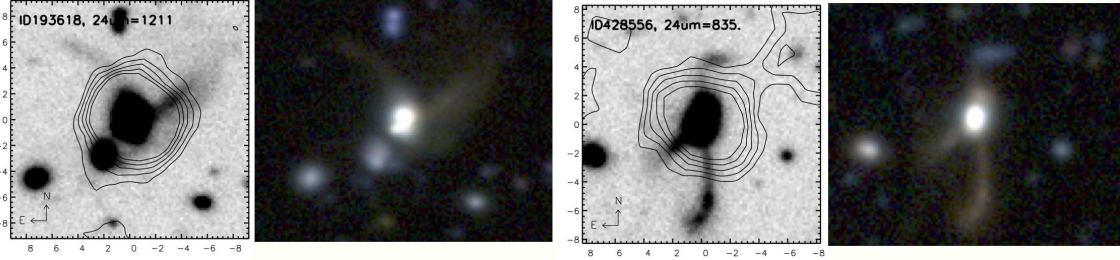


Figure 6.1: Two candidates for IRS spectroscopy. The thumbnails are 80kpc/h on a side with axes in arcseconds. The $24\mu\text{m}$ contours are overlaid on the i' -band images, with the $24\mu\text{m}$ flux noted in μJy . To the right of each galaxy is its g', r', i' colour composite.

6.2.2 Starburst-AGN Connection: Mid-IR Spectroscopy

As described in the previous Chapter, our results point to galaxy interactions as a potential triggering mechanism for not only star formation but also AGN activity. In order to explore the merger-starburst-AGN connection further, we have identified an important population of IR-bright galaxies with long tidal tail features (see Figure 6.1 some examples), at $0.45 < z < 1.0$ for deep IRS spectroscopy. The identification of galaxies with tidal tails is a clean way of selecting merging galaxies. These systems are within the 0.8 sq. deg. overlapping region of the CFHTLS and the *Spitzer* SWIRE Survey, and have heightened MIR properties from a combination of star formation and potentially AGN activity.

The sample consists of all galaxies with tidal tails above 1.0mJy at $24\mu\text{m}$, and all "long" tailed galaxies $>0.7\text{mJy}$. These galaxies are LIRGs or ULIRGs and represent a specific stage of the galaxy merger process associated with starburst activity. IRS spectroscopy of these merging systems would allow the investigate the following questions:

- Do Mid-IR spectral properties (PAH-band strengths, silicate absorption depths, AGN signatures) correlate with the stage of the merger and or length of tidal-tail? This could allow us to test whether AGN have turned on in these high-z merging systems, and the relative contribution of star formation and AGN activity.
- Do these galaxies share a common defining characteristic in their IR spectra resulting from a sudden starburst triggered by an interaction?
- Do IR bright mergers differ in significant ways from non-merging LIRG galaxies found in other surveys at the same redshift?

6.2.3 Comparison to Simulations: Merger Time-Scales

A large uncertainty in the measurements of galaxy interaction rates is the timescale a particular method of identifying mergers or interactions is sensitive for. If morphological classification is used, like that presented in this thesis one could ideally utilize a set of N-body simulations of merging galaxies. By classifying a set of merger simulations at various viewing angles and orbital configurations one could classify these simulated mergers with the same criteria applied to observational surveys. This would allow a more accurate estimate of the merger time-scale our particular method is sensitive to. Currently, there is a group at Harvard University compiling a catalog of simulated mergers with which we will be able to visually classify based on the scheme outlined in this thesis. Time-Scale accuracy could potentially be refined from $\sim 0.4\text{-}0.5$ Gyr down to $\sim 0.1\text{-}0.2$ Gyr based on preliminary studies.

This is an exciting and challenging time to be studying galaxy formation and evolution. Surveys like those mentioned above along side new and revolutionary instruments will provide the opportunities to fully understand or at least get a better handle on the processes linking mergers, interactions, star formation, AGN, and their roles in building galaxies both large and small.

Glossary & Acronyms

ACS	Advanced Camera for Surveys
AGN	Active Galactic Nucleus
CDM	Cold Dark Matter
CFHT	Canada France Hawaii Telescope
CFHTLS	Canada France Hawaii Telescope Legacy Survey
CIRB	Cosmic Infrared Background
CP	Close galaxy Pair
CVZ	Constant Viewing Zone
DDT	Directors Discretionary Time
DN	Double Nuclei
FIR	Far-Infrared (15 – 170 μm)
FLS	First Look Survey
FWHM	Full Width at Half Maximum
GIF	Galaxy Interaction Fraction
HST	<i>Hubble Space Telescope</i>
Gyr	Gigayear (10^9 years)
h	Parameterizes the Hubble constant, such that $H_o = 100h \text{km s}^{-1}\text{Mpc}^{-1}$
IR	Infrared
IRAC	Infrared Array Camera
IRAS	<i>Infrared Astronomical Satellite</i>
ISO	<i>Infrared Space Observatory</i>
kpc	kiloparsec (10^3 parsec)
LIR	Infrared Luminosity [8-1000 μm]
LIRG	Luminous Infrared Galaxy ($L_{[8-1000\mu\text{m}]} \gtrsim 10^{11} L_\odot$)
Mpc	Megaparsec (10^6 parsec)
MIPS	Multi-band Imaging Photometer
MIR	Mid-Infrared (2.5 – 24 μm)

NIR	Near-Infrared ($0.5 - 2.5 \mu\text{m}$)
PAH	Polycyclic Aromatic Hydrocarbons
parsec	Distance at which an Astronomical Unit (AU) subtends $1''$, on the sky. Equal to 3.26 light years.
PSF	Point Spread Function
Q	Luminosity Evolution Parameter
RMS	Root Mean Square
SB	Surface Brightness
SDSS	Sloan Digital Sky Survey
SFH	Star Formation History
<i>Spitzer</i>	<i>Spitzer</i> Space Telescope
SED	Spectral Energy Distribution
SFR	Star Formation Rate
SNLS	Supernova Legacy Survey (CFHTLS)
SNR	Signal-to-Noise Ratio
SSC	<i>Spitzer</i> Science Center
ULIRG	Ultra-luminous Infrared Galaxy ($\text{L}_{[8-1000\mu\text{m}]} \gtrsim 10^{12} L_\odot$)
UV	Ultra-Violet
XFLS	Extragalactic First Look Survey

Bibliography

- Abraham, R. G., Tanvir, N. R., Santiago, B. X., Ellis, R. S., Glazebrook, K., & van den Bergh, S. 1996a, MNRAS, 279, L47
- Abraham, R. G., van den Bergh, S., Glazebrook, K., Ellis, R. S., Santiago, B. X., Surma, P., & Griffiths, R. E. 1996b, ApJS, 107, 1
- Abraham, R. G., van den Bergh, S., & Nair, P. 2003, ApJ, 588, 218
- Appleton, P. N., Fadda, D. T., Marleau, F. R., Frayer, D. T., Helou, G., Condon, J. J., Choi, P. I., Yan, L., Lacy, M., Wilson, G., Armus, L., Chapman, S. C., Fang, F., Heinrichson, I., Im, M., Jannuzzi, B. T., Storrie-Lombardi, L. J., Shupe, D., Soifer, B. T., Squires, G., & Teplitz, H. I. 2004, ApJS, 154, 147
- Arp, H. 1966, ApJS, 14, 1
- Bahcall, J. N., Kirhakos, S., Saxe, D. H., & Schneider, D. P. 1997, ApJ, 479, 642
- Barnes, J. E. 1998, in Saas-Fee Advanced Course 26: Galaxies: Interactions and Induced Star Formation, ed. R. C. Kennicutt, Jr., F. Schweizer, J. E. Barnes, D. Friedli, L. Martinet, & D. Pfenniger, 275–+
- Barnes, J. E. 2004, MNRAS, 350, 798
- Barton, E. J., Geller, M. J., & Kenyon, S. J. 2000, ApJ, 530, 660
- Baum, W. A. 1962, in IAU Symposium, Vol. 15, Problems of Extra-Galactic Research, ed. G. C. McVittie, 390–+
- Bell, E. F., Papovich, C., Wolf, C., Le Floc'h, E., Caldwell, J. A. R., Barden, M., Egami, E., McIntosh, D. H., Meisenheimer, K., Pérez-González, P. G., Rieke, G. H., Rieke, M. J., Rigby, J. R., & Rix, H.-W. 2005, ApJ, 625, 23
- Benítez, N., Ford, H., Bouwens, R., Menanteau, F., Blakeslee, J., Gronwall, C., Illingworth, G., Meurer, G., Broadhurst, T. J., Clampin, M., Franx, M., Hartig, G. F., Magee, D., Sirianni, M.,

- Ardila, D. R., Bartko, F., Brown, R. A., Burrows, C. J., Cheng, E. S., Cross, N. J. G., Feldman, P. D., Golimowski, D. A., Infante, L., Kimble, R. A., Krist, J. E., Lesser, M. P., Levay, Z., Martel, A. R., Miley, G. K., Postman, M., Rosati, P., Sparks, W. B., Tran, H. D., Tsvetanov, Z. I., White, R. L., & Zheng, W. 2004, *ApJS*, 150, 1
- Berrier, J. C., Bullock, J. S., Barton, E. J., Guenther, H. D., Zentner, A. R., & Wechsler, R. H. 2006, *ApJ*, 652, 56
- Bertin, E. & Arnouts, S. 1996, *A&AS*, 117, 393
- Binney, J. & Tremaine, S. 1987, Princeton University Press: Princeton
- Bolzonella, M., Miralles, J.-M., & Pelló, R. 2000, *A&A*, 363, 476
- Boselli, A., Sauvage, M., Lequeux, J., Donati, A., & Gavazzi, G. 2003, *A&A*, 406, 867
- Bridge, C. R., Appleton, P. N., Conselice, C. J., Choi, P. I., Armus, L., Fadda, D., Laine, S., Marleau, F. R., Carlberg, R. G., Helou, G., & Yan, L. 2007a, ArXiv Astrophysics e-prints, 659, 931
- . 2007b, *ApJ*, 659, 931
- Bundy, K., Fukugita, M., Ellis, R. S., Kodama, T., & Conselice, C. J. 2004, *ApJ*, 601, L123
- Burkey, J. M., Keel, W. C., Windhorst, R. A., & Franklin, B. E. 1994, *ApJ*, 429, L13
- Bushouse, H. A. 1986, *AJ*, 91, 255
- Bushouse, H. A., Borne, K. D., Colina, L., Lucas, R. A., Rowan-Robinson, M., Baker, A. C., Clements, D. L., Lawrence, A., & Oliver, S. 2002, *ApJS*, 138, 1
- Carlberg, R. G., Cohen, J. G., Patton, D. R., Blandford, R., Hogg, D. W., Yee, H. K. C., Morris, S. L., Lin, H., Hall, P. B., Sawicki, M., Wirth, G. D., Cowie, L. L., Hu, E., & Songaila, A. 2000, *ApJ*, 532, L1
- Carlberg, R. G., Pritchett, C. J., & Infante, L. 1994, *ApJ*, 435, 540
- Carlberg, R. G., Yee, H. K. C., Morris, S. L., Lin, H., Hall, P. B., Patton, D. R., Sawicki, M., & Shepherd, C. W. 2001, *ApJ*, 563, 736
- Cassata, P., Cimatti, A., Franceschini, A., Daddi, E., Pignatelli, E., Fasano, G., Rodighiero, G., Pozzetti, L., Mignoli, M., & Renzini, A. 2005, *MNRAS*, 357, 903
- Chary, R. & Elbaz, D. 2001, *ApJ*, 556, 562

- Choi, P. I., Yan, L., Im, M., Helou, G., Soifer, B. T., Storrie-Lombardi, L. J., Chary, R., Teplitz, H. I., Fadda, D., Marleau, F. R., Lacy, M., Wilson, G., Appleton, P. N., Frayer, D. T., & Surace, J. A. 2006, *ApJ*, 637, 227
- Clavel, J., Schulz, B., Altieri, B., Barr, P., Claes, P., Heras, A., Leech, K., Metcalfe, L., & Salama, A. 2000, *A&A*, 357, 839
- Condon, J. J. 1992, *ARA&A*, 30, 575
- Conselice, C. J. 1997, *PASP*, 109, 1251
- . 2003, *ApJS*, 147, 1
- . 2006a, *ApJ*, 638, 686
- . 2006b, *MNRAS*, 373, 1389
- Conselice, C. J., Bershady, M. A., Dickinson, M., & Papovich, C. 2003, *AJ*, 126, 1183
- Conselice, C. J., Bershady, M. A., & Jangren, A. 2000, *ApJ*, 529, 886
- Conselice, C. J., Blackburne, J. A., & Papovich, C. 2005, *ApJ*, 620, 564
- Cox, T. J., Jonsson, P., Primack, J. R., & Somerville, R. S. 2006, *MNRAS*, 373, 1013
- Dale, D. A., Helou, G., Contursi, A., Silbermann, N. A., & Kolhatkar, S. 2001, *ApJ*, 549, 215
- Dasyra, K. M., Tacconi, L. J., Davies, R. I., Genzel, R., Lutz, D., Naab, T., Burkert, A., Veilleux, S., & Sanders, D. B. 2006, *ApJ*, 638, 745
- Desert, F.-X., Boulanger, F., & Puget, J. L. 1990, *A&A*, 237, 215
- Dubinski, J., Mihos, J. C., & Hernquist, L. 1999, *ApJ*, 526, 607
- Efron, B. & Tibshirani, R. 1986, *Stat. Sci.*, 1, 54
- Elbaz, D., Cesarsky, C. J., Chanial, P., Aussel, H., Franceschini, A., Fadda, D., & Chary, R. R. 2002, *A&A*, 384, 848
- Fadda, D., Flores, H., Hasinger, G., Franceschini, A., Altieri, B., Cesarsky, C. J., Elbaz, D., & Ferrando, P. 2002, *A&A*, 383, 838
- Fadda, D., Jannuzzi, B. T., Ford, A., & Storrie-Lombardi, L. J. 2004, *AJ*, 128, 1

- Fadda, D., Marleau, F. R., Storrie-Lombardi, L. J., Makovoz, D., Frayer, D. T., Appleton, P. N., Armus, L., Chapman, S. C., Choi, P. I., Fang, F., Heinrichsen, I., Helou, G., Im, M., Lacy, M., Shupe, D. L., Soifer, B. T., Squires, G. K., Surace, J., Teplitz, H. I., Wilson, G., & Yan, L. 2006, AJ, 131, 2859
- Fazio, G. G., Hora, J. L., Allen, L. E., Ashby, M. L. N., Barmby, P., Deutsch, L. K., Huang, J.-S., Kleiner, S., Marengo, M., Megeath, S. T., Melnick, G. J., Pahre, M. A., Patten, B. M., Polizotti, J., Smith, H. A., Taylor, R. S., Wang, Z., Willner, S. P., Hoffmann, W. F., Pipher, J. L., Forrest, W. J., McMurry, C. W., McCreight, C. R., McKelvey, M. E., McMurray, R. E., Koch, D. G., Moseley, S. H., Arendt, R. G., Mentzell, J. E., Marx, C. T., Losch, P., Mayman, P., Eichhorn, W., Krebs, D., Jhabvala, M., Gezari, D. Y., Fixsen, D. J., Flores, J., Shakoorzadeh, K., Jungo, R., Hakun, C., Workman, L., Karpati, G., Kichak, R., Whitley, R., Mann, S., Tollestrup, E. V., Eisenhardt, P., Stern, D., Gorjian, V., Bhattacharya, B., Carey, S., Nelson, B. O., Glaccum, W. J., Lacy, M., Lowrance, P. J., Laine, S., Reach, W. T., Stauffer, J. A., Surace, J. A., Wilson, G., Wright, E. L., Hoffman, A., Domingo, G., & Cohen, M. 2004, ApJS, 154, 10
- Ferguson, H. C., Dickinson, M., Giavalisco, M., Kretchmer, C., Ravindranath, S., Idzi, R., Taylor, E., Conselice, C. J., Fall, S. M., Gardner, J. P., Livio, M., Madau, P., Moustakas, L. A., Papovich, C. M., Somerville, R. S., Spinrad, H., & Stern, D. 2004, ApJ, 600, L107
- Fioc, M. & Rocca-Volmerange, B. 1997, A&A, 326, 950
- Glassman, T. M. 2007, preparation
- Gottlöber, S., Klypin, A., & Kravtsov, A. V. 2001, ApJ, 546, 223
- Graham, A. W. & Driver, S. P. 2005, Publications of the Astronomical Society of Australia, 22, 118
- Grazian, A., Fontana, A., de Santis, C., Nonino, M., Salimbeni, S., Giallongo, E., Cristiani, S., Gallozzi, S., & Vanzella, E. 2006, A&A, 449, 951
- Gwyn, S. D. J. & Hartwick, F. D. A. 1996, ApJ, 468, L77+
- Hibbard, J. E. & van Gorkom, J. H. 1996, AJ, 111, 655
- Hopkins, A. M. 2004, ApJ, 615, 209
- Hopkins, P. F., Hernquist, L., Cox, T. J., Di Matteo, T., Martini, P., Robertson, B., & Springel, V. 2005, ApJ, 630, 705
- Hubble, E. P. 1926, ApJ, 64, 321

- Infante, L. 1987, A&A, 183, 177
- Infante, L., de Mello, D. F., & Menanteau, F. 1996, ApJ, 469, L85+
- Kartaltepe, J. S., Sanders, D. B., Scoville, N. Z., Calzetti, D., Capak, P., Koekemoer, A., Mobasher, B., Murayama, T., Salvato, M., Sasaki, S. S., & Taniguchi, Y. 2007, ArXiv e-prints, 705
- Kennicutt, Jr., R. C. 1998, ARA&A, 36, 189
- Kewley, L. J. & Dopita, M. A. 2003, in Revista Mexicana de Astronomia y Astrofisica Conference Series, Vol. 17, Revista Mexicana de Astronomia y Astrofisica Conference Series, ed. V. Avila-Reese, C. Firmani, C. S. Frenk, & C. Allen, 83–84
- Khochfar, S. & Burkert, A. 2001, ApJ, 561, 517
- Kron, R. G. 1980, ApJS, 43, 305
- Lacy, M., Petric, A. O., Sajina, A., Canalizo, G., Storrie-Lombardi, L. J., Armus, L., Fadda, D., & Marleau, F. R. 2007, AJ, 133, 186
- Lacy, M., Storrie-Lombardi, L. J., Sajina, A., Appleton, P. N., Armus, L., Chapman, S. C., Choi, P. I., Fadda, D., Fang, F., Frayer, D. T., Heinrichsen, I., Helou, G., Im, M., Marleau, F. R., Masci, F., Shupe, D. L., Soifer, B. T., Surace, J., Teplitz, H. I., Wilson, G., & Yan, L. 2004, ApJS, 154, 166
- Lacy, M., Wilson, G., Masci, F., Storrie-Lombardi, L. J., Appleton, P. N., Armus, L., Chapman, S. C., Choi, P. I., Fadda, D., Fang, F., Frayer, D. T., Heinrichsen, I., Helou, G., Im, M., Laine, S., Marleau, F. R., Shupe, D. L., Soifer, B. T., Squires, G. K., Surace, J., Teplitz, H. I., & Yan, L. 2005, ApJS, 161, 41
- Lagache, G., Dole, H., & Puget, J.-L. 2003, MNRAS, 338, 555
- Lagache, G., Dole, H., Puget, J.-L., Pérez-González, P. G., Le Floc'h, E., Rieke, G. H., Papovich, C., Egami, E., Alonso-Herrero, A., Engelbracht, C. W., Gordon, K. D., Misselt, K. A., & Morrison, J. E. 2004, ApJS, 154, 112
- Larson, R. B. & Tinsley, B. M. 1978, ApJ, 219, 46
- Laurent, O., Mirabel, I. F., Charmandaris, V., Gallais, P., Madden, S. C., Sauvage, M., Vigroux, L., & Cesarsky, C. 2000, A&A, 359, 887
- Lavery, R. J., Remijan, A., Charmandaris, V., Hayes, R. D., & Ring, A. A. 2004, ApJ, 612, 679

- Le Borgne, D. & Rocca-Volmerange, B. 2002, A&A, 386, 446
- Le Borgne, D., Rocca-Volmerange, B., Prugniel, P., Lançon, A., Fioc, M., & Soubiran, C. 2004, A&A, 425, 881
- Le Fèvre, O., Abraham, R., Lilly, S. J., Ellis, R. S., Brinchmann, J., Schade, D., Tresse, L., Colless, M., Crampton, D., Glazebrook, K., Hammer, F., & Broadhurst, T. 2000, MNRAS, 311, 565
- Le Floc'h, E., Papovich, C., Dole, H., Bell, E. F., Lagache, G., Rieke, G. H., Egami, E., Pérez-González, P. G., Alonso-Herrero, A., Rieke, M. J., Blaylock, M., Engelbracht, C. W., Gordon, K. D., Hines, D. C., Misselt, K. A., Morrison, J. E., & Mould, J. 2005, ApJ, 632, 169
- Leauthaud, A., Massey, R., Kneib, J. P., Rhodes, J., Johnston, D. E., Capak, P., Heymans, C., Ellis, R. S., Koekemoer, A. M., Le Fevre, O., Mellier, Y., Refregier, A., Robin, A. C., Scoville, N., Tasca, L., Taylor, J. E., & Van Waerbeke, L. 2007, ArXiv Astrophysics e-prints
- Lilly, S., Schade, D., Ellis, R., Le Fevre, O., Brinchmann, J., Tresse, L., Abraham, R., Hammer, F., Crampton, D., Colless, M., Glazebrook, K., Mallen-Ornelas, G., & Broadhurst, T. 1998, ApJ, 500, 75
- Lilly, S. J., Le Fevre, O., Hammer, F., & Crampton, D. 1996, ApJ, 460, L1+
- Lin, H., Yee, H. K. C., Carlberg, R. G., Morris, S. L., Sawicki, M., Patton, D. R., Wirth, G., & Shepherd, C. W. 1999, ApJ, 518, 533
- Lin, L., Koo, D. C., Weiner, B. J., Chiueh, T., Coil, A. L., Lotz, J., Conselice, C. J., Willner, S. P., Smith, H. A., Guhathakurta, P., Huang, J., Le Floc'h, E., Noeske, K. G., Willmer, C. N. A., Cooper, M. C., & Phillips, A. C. 2006, ArXiv Astrophysics e-prints
- Lin, L., Koo, D. C., Willmer, C. N. A., Patton, D. R., Conselice, C. J., Yan, R., Coil, A. L., Cooper, M. C., Davis, M., Faber, S. M., Gerke, B. F., Guhathakurta, P., & Newman, J. A. 2004, ApJ, 617, L9
- Loh, E. D. & Spillar, E. J. 1986, ApJ, 303, 154
- Lotz, J. M., Davis, M., Faber, S. M., Guhathakurta, P., Gwyn, S., Huang, J., Koo, D. C., Le Floc'h, E., Lin, L., Newman, J., Noeske, K., Papovich, C., Willmer, C. N. A., Coil, A., Conselice, C. J., Cooper, M., Hopkins, A. M., Metevier, A., Primack, J., Rieke, G., & Weiner, B. J. 2006, ArXiv Astrophysics e-prints
- Lutz, D., Spoon, H. W. W., Rigopoulou, D., Moorwood, A. F. M., & Genzel, R. 1998, ApJ, 505, L103

- Madau, P., Pozzetti, L., & Dickinson, M. 1998, *ApJ*, 498, 106
- Magnier, E. A. & Cuillandre, J.-C. 2004, *PASP*, 116, 449
- Maller, A. H., Katz, N., Kereš, D., Davé, R., & Weinberg, D. H. 2006, *ApJ*, 647, 763
- Marleau, F. R. 2007, preparation
- Marleau, F. R., Fadda, D., Storrie-Lombardi, L. J., Helou, G., Makovoz, D., Frayer, D. T., Yan, L., Appleton, P. N., Armus, L., Chapman, S., Choi, P. I., Fang, F., Heinrichsen, I., Im, M., Lacy, M., Shupe, D., Soifer, B. T., Squires, G., Surace, J., Teplitz, H. I., & Wilson, G. 2004, *ApJS*, 154, 66
- McCarthy, P. J., Le Borgne, D., Crampton, D., Chen, H.-W., Abraham, R. G., Glazebrook, K., Savaglio, S., Carlberg, R. G., Marzke, R. O., Roth, K., Jørgensen, I., Hook, I., Murowinski, R., & Juneau, S. 2004, *ApJ*, 614, L9
- Melbourne, J., Koo, D. C., & Le Floc'h, E. 2005, *ApJ*, 632, L65
- Metcalfe, N., Shanks, T., Campos, A., McCracken, H. J., & Fong, R. 2001, *MNRAS*, 323, 795
- Mihos, J. C. 2001, *ApJ*, 550, 94
- Mihos, J. C. & Hernquist, L. 1996, *ApJ*, 464, 641
- Neuschaefer, L. W., Im, M., Ratnatunga, K. U., Griffiths, R. E., & Casertano, S. 1997, *ApJ*, 480, 59
- Patton, D. R., Carlberg, R. G., Marzke, R. O., Pritchett, C. J., da Costa, L. N., & Pellegrini, P. S. 2000, *ApJ*, 536, 153
- Patton, D. R., Grant, J. K., Simard, L., Pritchett, C. J., Carlberg, R. G., & Borne, K. D. 2005, *AJ*, 130, 2043
- Patton, D. R., Pritchett, C. J., Carlberg, R. G., Marzke, R. O., Yee, H. K. C., Hall, P. B., Lin, H., Morris, S. L., Sawicki, M., Shepherd, C. W., & Wirth, G. D. 2002, *ApJ*, 565, 208
- Patton, D. R., Pritchett, C. J., Yee, H. K. C., Ellingson, E., & Carlberg, R. G. 1997, *ApJ*, 475, 29
- Press, W. H. & Schechter, P. 1974, *ApJ*, 187, 425
- Priddey, R. S. & McMahon, R. G. 2001, *MNRAS*, 324, L17
- Puget, J. L., Leger, A., & Boulanger, F. 1985, *A&A*, 142, L19

- Reshetnikov, V. P. 2000, A&A, 353, 92
- Rieke, G. H., Young, E. T., Engelbracht, C. W., Kelly, D. M., Low, F. J., Haller, E. E., Beeman, J. W., Gordon, K. D., Stansberry, J. A., Misselt, K. A., Cadien, J., Morrison, J. E., Rivlis, G., Latter, W. B., Noriega-Crespo, A., Padgett, D. L., Stapelfeldt, K. R., Hines, D. C., Egami, E., Muzerolle, J., Alonso-Herrero, A., Blaylock, M., Dole, H., Hinz, J. L., Le Floc'h, E., Papovich, C., Pérez-González, P. G., Smith, P. S., Su, K. Y. L., Bennett, L., Frayer, D. T., Henderson, D., Lu, N., Masci, F., Pesenson, M., Rebull, L., Rho, J., Keene, J., Stolovy, S., Wachter, S., Wheaton, W., Werner, M. W., & Richards, P. L. 2004, ApJS, 154, 25
- Sajina, A., Lacy, M., & Scott, D. 2005, ApJ, 621, 256
- Sandage, A. 1961, The Hubble atlas of galaxies (Washington: Carnegie Institution, 1961)
- Sanders, D. B. & Mirabel, I. F. 1996, ARA&A, 34, 749
- Sanders, D. B., Soifer, B. T., Elias, J. H., Madore, B. F., Matthews, K., Neugebauer, G., & Scoville, N. Z. 1988, ApJ, 325, 74
- Schlegel, D. J., Finkbeiner, D. P., & Davis, M. 1998, ApJ, 500, 525
- Schweizer, F. 1982, ApJ, 252, 455
- Shim, H., Im, M., Pak, S., Choi, P., Fadda, D., Helou, G., & Storrie-Lombardi, L. 2006, ApJS, 164, 435
- Smith, E. P. & Heckman, T. M. 1989, ApJ, 341, 658
- Soifer, B. T. & Neugebauer, G. 1991, AJ, 101, 354
- Soifer, B. T., Sanders, D. B., Madore, B. F., Neugebauer, G., Danielson, G. E., Elias, J. H., Lonsdale, C. J., & Rice, W. L. 1987, ApJ, 320, 238
- Spinoglio, L., Malkan, M. A., Rush, B., Carrasco, L., & Recillas-Cruz, E. 1995, ApJ, 453, 616
- Stern, D., Eisenhardt, P., Gorjian, V., Kochanek, C. S., Caldwell, N., Eisenstein, D., Brodwin, M., Brown, M. J. I., Cool, R., Dey, A., Green, P., Jannuzzi, B. T., Murray, S. S., Pahre, M. A., & Willner, S. P. 2005, ApJ, 631, 163
- Storrie-Lombardi, L. J. 2007, preparation
- STSCI. 1998

- Sullivan, M., Howell, D. A., Perrett, K., Nugent, P. E., Astier, P., Aubourg, E., Balam, D., Basa, S., Carlberg, R. G., Conley, A., Fabbro, S., Fouchez, D., Guy, J., Hook, I., Lafoux, H., Neill, J. D., Pain, R., Palanque-Delabrouille, N., Pritchett, C. J., Regnault, N., Rich, J., Taillet, R., Aldering, G., Baumont, S., Brionder, J., Filiol, M., Knop, R. A., Perlmutter, S., & Tao, C. 2006a, AJ, 131, 960
- Sullivan, M., Le Borgne, D., Pritchett, C. J., Hodzman, A., Neill, J. D., Howell, D. A., Carlberg, R. G., Astier, P., Aubourg, E., Balam, D., Basa, S., Conley, A., Fabbro, S., Fouchez, D., Guy, J., Hook, I., Pain, R., Palanque-Delabrouille, N., Perrett, K., Regnault, N., Rich, J., Taillet, R., Baumont, S., Brionder, J., Ellis, R. S., Filiol, M., Lusset, V., Perlmutter, S., Ripoche, P., & Tao, C. 2006b, ApJ, 648, 868
- Surace, J. A. e. a. 2005, SWIRE Data Site
- Thompson, R. I., Weymann, R. J., & Storrie-Lombardi, L. J. 2001, ApJ, 546, 694
- Toomre, A. 1977a, in Evolution of Galaxies and Stellar Populations, ed. B. M. Tinsley & R. B. Larson, 401–+
- Toomre, A. 1977b, ARA&A, 15, 437
- Toomre, A. & Toomre, J. 1972, ApJ, 178, 623
- Vorontsov-Velyaminov, B. A. 1959, in Atlas and catalog of interacting galaxies (1959), 0–+
- Wang, Y. P. 2006, ApJ, 638, 138
- Werner, M. W., Roellig, T. L., Low, F. J., Rieke, G. H., Rieke, M., Hoffmann, W. F., Young, E., Houck, J. R., Brandl, B., Fazio, G. G., Hora, J. L., Gehrz, R. D., Helou, G., Soifer, B. T., Stauffer, J., Keene, J., Eisenhardt, P., Gallagher, D., Gautier, T. N., Irace, W., Lawrence, C. R., Simmons, L., Van Cleve, J. E., Jura, M., Wright, E. L., & Cruikshank, D. P. 2004, ApJS, 154, 1
- Williams, R. E., Blacker, B., Dickinson, M., Dixon, W. V. D., Ferguson, H. C., Fruchter, A. S., Giavalisco, M., Gilliland, R. L., Heyer, I., Katsanis, R., Levay, Z., Lucas, R. A., McElroy, D. B., Petro, L., Postman, M., Adorf, H.-M., & Hook, R. 1996, AJ, 112, 1335
- Wolf, C., Bell, E. F., McIntosh, D. H., Rix, H.-W., Barden, M., Beckwith, S. V. W., Borch, A., Caldwell, J. A. R., Häussler, B., Heymans, C., Jahnke, K., Jogee, S., Meisenheimer, K., Peng, C. Y., Sánchez, S. F., Somerville, R. S., & Wisotzki, L. 2005, ApJ, 630, 771
- Woods, D., Fahlman, G. G., & Richer, H. B. 1995, ApJ, 454, 32
- Xu, C. K., Sun, Y. C., & He, X. T. 2004, ApJ, 603, L73

Yee, H. K. C. & Ellingson, E. 1995, *ApJ*, 445, 37

Zepf, S. E. & Koo, D. C. 1989, *ApJ*, 337, 34